Université Fédérale
Toulouse Midi-Pyrénées

THÈSE

En vue de l'obtention du

DOCTORAT DE L'UNIVERSITÉ DE TOULOUSE

Délivré par :

Université Toulouse 3 Paul Sabatier (UT3 Paul Sabatier)

Présentée et soutenue par :
Carolina GOMEZ-CARDENAS
le vendredi 4 décembre 2015

Titre :

Outils d'aide à l'optimisation des campagnes d'essais non destructifs sur ouvrages en béton armé

École doctorale et discipline ou spécialité :
ED MEGEP : Génie civil

Unité de recherche :
Laboratoire Matériaux et Durabilité des Constructions

Directeur/trice(s) de Thèse :
Jean-Paul BALAYSSAC
Zoubir-Mehdi SBARTAÏ
Vincent GARNIER

Jury :

Jean-Louis GALLIAS, Professeur, Université de Cergy-Pontoise	Rapporteur
Corinne CURT, Ingénieur de Recherche HDR, IRSTEA-Aix en Provence	Rapporteur
Franck SCHOEFS, Professeur, Université de Nantes	Examinateur
Jean-Paul BALAYSSAC, Professeur, Université Paul Sabatier	Examinateur
Zoubir-Mehdi SBARTAÏ, Maître de Conférences, Université de Bordeaux I	Examinateur
Vincent GARNIER, Maître de Conférences HDR, Université d'Aix-Marseille	Examinateur

ABSTRACT

Non-destructive testing methods (NDT) are essential for estimating concrete properties (mechanical or physical) and their spatial variability. They also constitute an useful tool to reduce the budget auscultation of a structure. The proposed approach is included in an ANR project (EvaDéOS) whose objective is to optimize the monitoring of civil engineering structures by implementing preventive maintenance to reduce diagnosis costs. In this thesis, the objective was to characterize at best a peculiar property of concrete (e.g. mechanical strength, porosity, degree of saturation, etc.), with technical ND sensitive to the same properties. For this aim, it is imperative to develop objective tools that allow to rationalize a test campaign on reinforced concrete structures.

For this purpose, first, it is proposed an optimal spatial sampling tool to reduce the number of auscultation points. The most commonly used algorithm is the spatial simulated annealing (SSA). This procedure is regularly used in geostatistical applications, and in other areas, but yet almost unexploited for civil engineering structures. In the thesis work, an original optimizing spatial sampling method (OSSM) inspired in the SSA and based on the spatial correlation was developed and tested in the case of on-site auscultation with two complementary fitness functions: mean prediction error and the error on the estimation of the global variability. This method is divided into three parts. First, the spatial correlation of ND measurements is modeled by a variogram. Then, the relationship between the number of measurements organized in a regular grid and the objective function is determined using a spatial interpolation method called kriging. Finally, the OSSM algorithm is used to minimize the objective function by changing the positions of a smaller number of ND measurements and for obtaining at the end an optimal irregular grid.

Destructive testing (DT) are needed to corroborate the information obtained by the ND measurements. Because of the cost and possible damage to the structure, an optimal sampling plan to collect a limited number of cores is important. For this aim, a procedure using data fusion based on the theory of possibilities and previously developed is used to estimate the properties of concrete from the ND. Through a readjustment bias requiring DTs performed on carrots, it is calibrated. Knowing that there is uncertainty about the results of DTs performed on carrots, it is proposed to take into account this uncertainty and propagate it through the calibration on the results of the fused data. By propagating this uncertainty, it is obtained mean fused values with a standard deviation. One can thus provide a methodology for positioning and minimizing the number of cores required to auscultate a structure by two methods: first, using the OSSM for the results of fused properties values in each measuring point and the second by the minimization of the average standard deviation over all of the fused points obtained after the propagation of DTs uncertainties.

Finally, in order to propose an alternative to the possibility theory, neural networks are also tested as alternative methods for their relevance and usability.

Keywords: NDT, inspection, concrete structure, optimization, spatial variability, uncertainties, data fusion, artificial neural networks.

RÉSUMÉ

Les méthodes de contrôle non destructif (CND) sont essentielles pour estimer les propriétés du béton (mécaniques ou physiques) et leur variabilité spatiale. Elles constituent également un outil pertinent pour réduire le budget d'auscultation d'un ouvrage d'art. La démarche proposée est incluse dans un projet ANR (EvaDéOS) dont l'objectif est d'optimiser le suivi des ouvrages de génie civil en mettant en œuvre une maintenance préventive afin de réduire les coûts. Dans le cas du travail de thèse réalisé, pour caractériser au mieux une propriété particulière du béton (ex : résistance mécanique, porosité, degré de Saturation, etc.), avec des méthodes ND sensibles aux mêmes propriétés, il est impératif de développer des outils objectifs permettant de rationaliser une campagne d'essais sur les ouvrages en béton armé.

Dans ce but, premièrement, il est proposé un outil d'échantillonnage spatial optimal pour réduire le nombre de points d'auscultation. L'algorithme le plus couramment employé est le recuit simulé spatial (RSS). Cette procédure est régulièrement utilisée dans des applications géostatistiques, et dans d'autres domaines, mais elle est pour l'instant quasiment inexploitée pour des structures de génie civil. Dans le travail de thèse, une optimisation de la méthode d'optimisation de l'échantillonnage spatial (MOES) originale inspirée du RSS et fondée sur la corrélation spatiale a été développée et testée dans le cas d'essais sur site avec deux fonctions objectifs complémentaires : l'erreur de prédiction moyenne et l'erreur sur l'estimation de la variabilité. Cette méthode est décomposée en trois parties. Tout d'abord, la corrélation spatiale des mesures ND est modélisée par un variogramme. Ensuite, la relation entre le nombre de mesures organisées dans une grille régulière et la fonction objectif est déterminée en utilisant une méthode d'interpolation spatiale appelée krigeage. Enfin, on utilise l'algorithme MOES pour minimiser la fonction objectif en changeant les positions d'un nombre réduit de mesures ND et pour obtenir à la fin une grille irrégulière optimale.

Des essais destructifs (ED) sont nécessaires pour corroborer les informations obtenues par les mesures ND. En raison du coût ainsi que des dégâts possibles sur la structure, un plan d'échantillonnage optimal afin de prélever un nombre limité de carottes est important. Pour ce faire, une procédure utilisant la fusion des données fondée sur la théorie des possibilités et développée antérieurement, permet d'estimer les propriétés du béton à partir des ND. Par le biais d'un recalage nécessitant des ED réalisés sur carottes, elle est étalonnée. En sachant qu'il y a une incertitude sur le résultat des ED réalisés sur les carottes, il est proposé de prendre en compte cette incertitude et de la propager au travers du recalage sur les résultats des données fusionnées. En propageant ces incertitudes, on obtient des valeurs fusionnées moyennes par point avec un écart-type. On peut donc proposer une méthodologie de positionnement et de minimisation du nombre des carottes nécessaire pour ausculter une structure par deux méthodes : la première, en utilisant le MOES pour les résultats des propriétés sortis de la fusion dans chaque point de mesure et la seconde par la minimisation de l'écart-type moyen sur la totalité des points fusionnés, obtenu après la propagation des incertitudes des ED.

Pour finir, afin de proposer une alternative à la théorie des possibilités, les réseaux de neurones sont également testés comme méthodes alternatives pour leur pertinence et leur simplicité d'utilisation.

Mots-clés: CND, surveillance, structure en béton, optimisation, variabilité spatiale, incertitudes, fusion des données, réseau de neurones.

TABLE OF CONTENTS

TABLE OF FIGURES

TABLE OF TABLES

CHAPTER 1
GENERAL INTRODUCTION

1.1. Framework and context

Nowadays, most of the structures for human use (buildings, bridges, etc.) are made of concrete. It is of vital importance to ensure that they function correctly during their service life and it has become crucial to find a reliable and efficient method for evaluating the condition of a structure at different times of its life span. Traditionally, the most commonly used method for the evaluation of a concrete structure has been visual inspection [1]. It is usually carried out by an expert engineer, who defines the most degraded zones of the structure and takes some samples (cores) in order to refine his analysis and eventually propose a reparation procedure. This method, which is subjective and remains informal, can only be used when a number of pathologies in the concrete, like cracking and spalling, are visible. Other pathologies, such as reinforcing steel corrosion are difficult to identify with visual inspection alone. Besides, using only the destructive test extracted from the studied structure to establish a diagnosis makes it unreliable for different reasons:

- The quantity of cores extracted from a studied structure element will be minimum and certainly not enough to make a reliable diagnosis, due to its price and how these test can compromise the integrity of the structure, thus, too many extracted cores could result in a decrease of the lifespan of the structure.
- The concrete is a heterogeneous material and the assessment of its properties/pathologies can be complex due to concrete intrinsic variability. It is also due to concrete spatial variability that at the same time can be due to the evolution of concrete properties affected by weather conditions (humidity, wind, etc.) or it can also be due to concrete segregation due to inappropriate formulation or casting procedure. Moreover, the destructive measurement itself can be variable depending on how many cores are tested, the environmental conditions at the moment of the cores extraction, how the cores are stored and the type of test used to assess a concrete property in particular.

For that reason, non-destructive testing (NDT) is an interesting complement in the diagnosis of a concrete structure [2-7]. It started to be used in reinforced concrete structures due to the increasing need to objectively evaluate their condition. The aim was also to manage the safety of the structure and to eventually set up a maintenance plan [8-10]. NDT also opened up the possibility of preventive maintenance, which is three to twenty times less expensive than repair in terms of energy and financial resources [11]. This is possible because, with NDT, pathologies and damages in the concrete and even the reinforcing steel corrosion can be detected before their consequences can be observed.

In France, the management of the concrete structures has become a subject of interest for their managers. They want to ensure the security, preservation and quality of service provided to the

users of their structures at a minimum cost. In order to do this, they have to implement an effective system which allows monitoring a structure by also being able to predict its evolution. To this aim, different research projects were carried out like SENSO, ACDC-C2D2, etc. which objectives were the following:

- Combination of different NDT's to evaluate the properties and degradation state of a structure by doing measurements in laboratory slabs.
- Readjustment of the measurements made in a real structure and calculation of degradation indicators, which will allow to obtain an objective, useful and reliable information of the structure state.

The current French ANR project EvaDéOS (Evaluation non destructive pour la prédiction de la Dégradation des structures et l'Optimisation de leur Suivi) also aims to take into account the temporal variability of the measurements to choose and to develop degradation models, in order to propose an appropriate maintenance strategy by ensuring appropriate levels of serviceability and safety at a minimum cost. This project, contrary to the past two projects, is focused in the reinforcement steel corrosion, induced by carbonation, which is one of the most common pathologies. Moreover, they are directly related to structural damage and reduction of the structure durability.

EvaDéOS, contrary to other studies made before about the inspection and maintenance of corroding reinforced concrete structures [4], does not focus on structures already affected by corrosion of reinforcement steel. In contrast, the project is focused on structures that are not still affected by the reinforcement steel corrosion, but for which the process is likely to be initiated due to its specific exposure or to its age. Hence, this project takes place on a preventive stage, in which the indicators indicating the initiation of the corrosion (carbonation depth or chloride content) are not yet visible. This is why the use of NDT is vital, as well as the intervention of other disciplinary fields to be able to propose a complete plan, from the diagnosis to the decision of the maintenance strategy including the prediction of the concrete degradation.

1.2. Thesis subject

The project EvaDéOS is divided into 6 operational tasks as shown in figure 1.1. The task 3 which is "Evaluation and Characterization", involves all of the developments that are necessary in the domain of NDT, but also semi-destructive and destructive testing. The objectives of this task are:

- The multi-technical approach for structures inspection taking into account the spatial and temporary variability in the measured data.

- The quantification of a degraded depth in the concrete presenting mechanical, physical and chemical properties significantly different from the ones present in the core of the structural element.
- The validation and adjustment of the inputs used in the degradation models and also the evaluation of pathological indicators to update the outputs estimated by the degradation models.

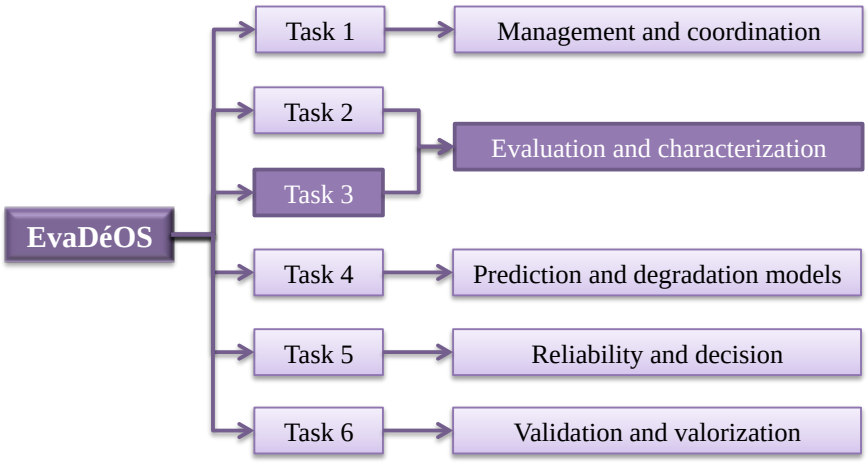

Figure 1-1. Operational tasks in EVADEOS project.

The current thesis which title is “Tools to optimize non-destructive testing campaigns on reinforced concrete structures” focused on the first objective of task 3. It concentrated primarily in the development of statistical tools that take into account the variability of the concrete properties/pathologies obtained by NDTs, or destructive testing. The study of the combination of different NDT methods to obtain the most reliable information of a concrete structure was also made. In order to do this, different skills were needed. That is why it was planned to divide the development of the thesis in three French laboratories with different, but complementary specialties.

One of the laboratories is the I2M. It is located in the city of Talence at the University of Bordeaux 1. This laboratory is specialized in some NDT like Electric Resistivity and Rebound hammer. It is also specialized in geostatistics applied to civil engineering, especially in the domain of spatial variability. They also specialized NDT combination methods like neural networks and surfaces of response. Another laboratory is the LMA-LCND. It is located in the city of Aix en Provence at the University of Aix-Marseille. This laboratory is specialized in the Ultrasonic technique, as well as a data fusion method called Theory of Possibilities. The last laboratory involved in this thesis is the LMDC, located in the city of Toulouse at the University Paul Sabatier – INSA Toulouse. This laboratory is specialized in the Ground-Penetrating Radar (GPR) and electrical resistivity method, as well as the neural networks as a NDT combination

method. As it can be seen, the three laboratories have different and complementary skills for the development of this thesis.

As it was said before, to estimate the degradation state of a concrete structure, it is important to plan a maintenance strategy at a minimum cost. For that aim, the development of an optimal diagnosis process is mandatory. Until now, projects like SENSO and ACDC have focused in developing the different NDT methods and have also developed a data fusion method to obtain the most reliable information of the properties of a concrete slab or structure. However, it is important to emphasize that often the diagnosis is limited by a budget. Hence, it is important to develop an optimal methodology for the assessment of concrete properties on real structures, taking into account variability of both NDT and DT. This was the main objective of this thesis.

The first axe of the thesis was about the study of the spatial correlation and variability of NDT for creating an optimal spatial sampling that will eventually be useful to plan this strategy. Its objective would be to evaluate the properties of a concrete structure accurately using a combination of fast and low cost NDT, higher quality NDT and eventually semi-destructive or destructive testing obtaining a convenient cost/benefice ratio (figure 2.2). The optimal location of the few semi-destructive or destructive testing (DT) would be obtained by two different methods. The first one consists in taking into account the spatial variability of the concrete properties obtained by a NDT combination method, data fusion or artificial neural networks (third axe of the thesis), to later locate optimally a fixed number of DTs using the spatial sampling method developed, thus, reducing the estimation error on the original field. The other one, treated in the second axe of the thesis, seeks the reduction on the number of DTs and their optimal location by studying the sensitivity of the error obtained on the concrete properties estimated by data fusion. This error is obtained by introducing and propagating a fixed value of DT uncertainty through the data fusion process.

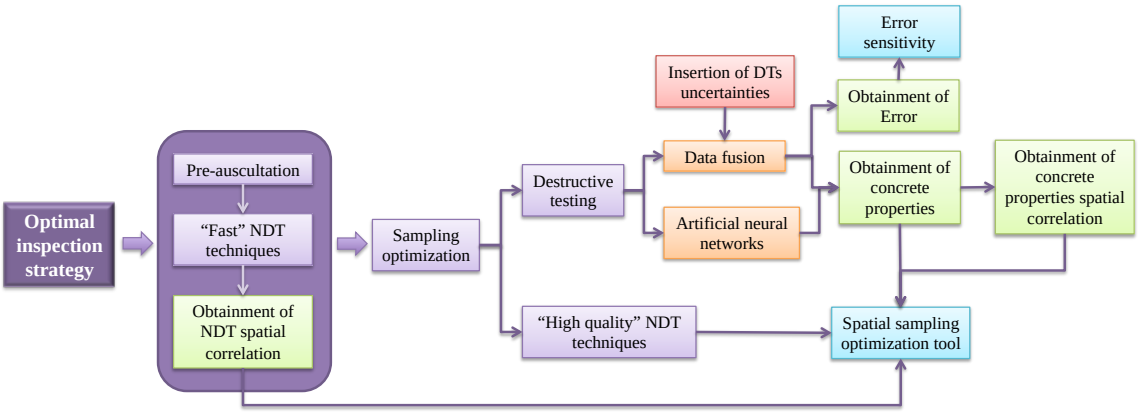

Figure 1-2. Optimal inspection strategy.

In this manuscript, a state of the art of the knowledge necessary to develop the proposed approach is presented (chapter 2). This knowledge includes destructive testing variability on laboratory and on-site samples, non-destructive and destructive testing spatial variability for on-site measurements, and the description of three NDT combination methods commonly used (surface response, data fusion and artificial neural networks). Moreover, this work was divided in three principal axes, which are at the same time concatenated and valuable to propose a reliable diagnosis strategy at a minimum cost. The first one (chapter 3), is the spatial variability analysis of NDT measurements, which objective is to propose an optimal spatial sampling of NDT measurements and coring of samples for complementary semi-destructive or destructive testing, taking into account the spatial correlation of NDT measurements of concrete properties obtained by a NDT combination method. The second one (chapter 4) consists on propagating the variability (uncertainties) of the concrete properties (porosity, water content, carbonation, etc.) obtained by destructive testing, through a NDT data fusion process developed in the ACDC project. The third one (chapter 5) consisted on testing a NDT combination method different to the data fusion one (Artificial Neural Networks) and comparing their performances. For this to be possible, it was used and exploited all the data concerning measurements of NDT made in SENSO and EVADEOS projects by the laboratories involved and their collaborators. Finally, an on-site application of the developed methods is presented (chapter 6).

References

[1] Balayssac, J.P., et al, ANR-GUI-AAP-04-Scientific Document, 2011.

[2] Balayssac, J.P., Laurens, S., Arliguie, G., Breysse, D., Garnier, V., Dérobert, X., et al. Description of the general outlines of the French project SENSO – quality assessment and limits of different NDT methods, Constr Build Master, Special issue.

[3] Barnes, R., Variogram Tutorial, Global Software, Inc.

[4] Bastidas-Arteaga, E., Schoefs, F., Stochastic improvement of inspection and maintenance of corroding reinforced concrete structures placed in unsaturated environments, Engineering Structures, vol. 41, 2012, p. 50-62.

[5] Bohling, G., Kriging, C&PE 940, 2005.

[6] Doetsch, J., Linde, N., Pessognelli, M., Green, A.G., Günther, T., Constraining 3-D electrical resistance tomography with GPR reflection data for improved aquifer characterization, Applied Geophysics, vol. 78, 2012, p. 68-76.

[7] Ferreyra, R.A., Apeztegui, H.P., Sereno, R., Jones, J.W., Reduction of soil water spatial sampling density using scaled semivariograms and simulated annealing, Geoderma, vol. 110, 2002, p. 265-289.

[8] Melles, S.J., Heuvelink, G.B.M., Twenhöfel C.J.W., Van Dijk, A., Hiemstra, P.H., Baume, O., Stöhlker, U., Optimizing the spatial pattern of networks for monitoring radioactive releases, Computers & Geosciences, vol. 37, 2011, p. 280-288.

[9] Pardo-Igdzquiza, E., Chica-Olmo, M., The Fourier Integral Method: An efficient spectral method for simulation of random fields, Mathematical Geology, vol. 25, n° 2, 1993.

[10] Ploix, M.A., Garnier, V., Moysan, J., Breysse, D., NDE data fusion to improve the evaluation of concrete structures, NDT&E, vol. 44, 2011, p. 442-448.

[11] Sbartaï, Z.M., Breysse, D., Larget, M., Balayssac, J.P., Combining NDT techniques for improved evaluation of concrete properties, Cement & Concrete Composites, vol. 34, 2012, p. 725-733

CHAPTER 2

DIAGNOSIS OF CONCRETE STRUCTURES - STATE OF THE ART

2.1. Introduction

The diagnosis of concrete structures has become an important issue due to the ever-increasing need for maintenance and repair interventions on structures. More importantly, the continuous increase of building costs often makes repair operations economically more viable, even if the deterioration of the structure is at an advanced stage. However, the diagnosis has its own cost, and it must be included in the maintenance/repair budget. Throughout the years, different strategies and methods have been used and normalized in different countries to evaluate the degradation state of a structure and for establishing a diagnosis. The strategies are usually based in the identification and evaluation of different pertinent properties of the concrete (i.e. compressive strength, water content, porosity). However, must of these strategies have focused on destructive tests that are variable, due to several factors like: the test protocols, the size of the samples/cores, the few number of samples/cores that are tested, etc. Besides, these samples are rather made in laboratory, where the conditions are not as the on-site conditions, or taken from a part of a structure, which will not be representative of the structure concrete actual state. Moreover, these strategies are also time/budget consuming, which leads to propose new strategies that include non-destructive testing (NDT), to obtain a more complete and less expensive assessment without decreasing the quality of the final diagnosis.

Nevertheless, the use of NDT adds a layer of uncertainty to the already uncertain concrete evaluation. NDTs measurements can also be variable or uncertain, due to factors such as weather conditions at the moment of measurement (temperature, humidity, etc.), the NDT used, among others. Hence, to reduce the uncertainties on the use of NDTs, different NDTs can be combined to evaluate a certain concrete property, reducing the variability or uncertainty of the measurement that each NDT may have. However, these combinations are often based on laboratory results, thus, it is difficult to obtain satisfactory results for an on-site case. This trouble will lead to the use of a calibration process that includes on-site NDT measurements and some destructive tests results from extracted cores.

In this chapter, a state of the art of different methodologies used throughout the years to evaluate the actual state of an existing concrete structure is presented. From destructive testing, passing through non-destructive test, to finally arrive to a combination of the two of them. It will also be shown different statistical tools that have been used in other fields with different purposes, and that have been slowly successfully incorporated into concrete structures evaluation.

2.2. Concrete variability

The concrete is a complex material which heterogeneity depends on many factors like the natural variability of its constituents, its formulation, the quality of vibration and compaction,

the initial concrete temperature, its evolution on different environmental conditions, etc. As a consequence, evaluating its initial quality and aging evolution has always been of major interest not only for structures monitoring, but also for structural design calculations during its service life.

Different evaluations are taken into account to assess different concretes or/and concrete properties or pathologies that are called indicators. For instance, Breysse [1] presents three principal categories of indicators: mechanical (e.g. compressive strength, Young's modulus), physical (e.g. porosity, water content) and linked to pathologies (e.g. carbonation, chloride content). These categories can provide a reliable concrete performance as they consider both mechanic and durability indicators. Traditionally, the methods used to evaluate different concrete properties (most of them focus on assessing the compressive strength of the concrete) are: i) destructive test on samples made in laboratory on controlled conditions, ii) destructive test on samples made with the same structure concrete or iii) destructive test on cores extracted directly from the structure. The two first methods provide what is usually called *potential concrete properties* and the third one provides *actual concrete properties*. In the following sections, indicator results will be compared by their mean values and their coefficient of variation (COV), which is the relationship between the mean and the standard deviation of the studied data samples. A high value of COV indicates an important variability of the measured indicator result, hence, a bad estimation of the studied indicator. Besides, the COV is also highly influenced by the number of samples used to estimate it, as it is noticed in the next sections.

2.2.1. Destructive test on laboratory samples

This kind of studies, were performed in the late nighties mostly to calibrate the existing standards to assure repeatability on laboratory destructive tests. For this aim, the projects AFREM "Durabilité des bétons" and GRANDUBE [2,3] performed different destructive tests to assess two indicators: carbonation and porosity, to compare different tests and concretes.

For porosity, two concrete types were used: a B25 and a B80. The maximal dimension of aggregates was 20mm. The cylindrical samples (30 for B25 and 30 for B80) were poured and held in a wet room for 60 days. The tests were made according to standards ISO 5017 and ISO 6275 with drying temperatures of 60°C, 80°C and 105°C. Table 2.1 shows the mean and coefficient of variation (COV) of porosity for the two studied concretes at the three drying temperatures.

Table 2-1. Mean and coefficient of variation (COV) of porosity obtained with the two standards (ISO 5017 and ISO 6275) for the two studied concretes, at the three drying temperatures with the two standards [2].

		ISO 5017 **60°C**	***ISO 5017*** ***80*****°C**	***ISO 5017*** **105°C**	***ISO 6275*** **105°C**
B25	Mean	16.6	17.2	18.1	17.7
	COV (%)	5.2	5.9	4.0	8.4
B80	Mean	6.7	8.6	11.8	11.1
	COV (%)	12.4	17.6	3.0	12.8

The conclusions for this study pointed that the results of the measured porosities for B25 after drying at 60°C, 80°C and 105°C increased slightly with the drying temperature but their values are close. In the case of B80, the drying process at 60°C and 80°C does not allow water draining from the samples quickly enough: after 30 days of drying the masses are not still constant. Only drying at 105°C allows a stabilization of the mass after a reasonable time length. At 105°C, the COV of the distribution of results is minimum for both concretes and, the values obtained at 105°C according to ISO 6275 are similar to those obtained according to ISO 5017. However, the COVs of porosity obtained with ISO 6275 is two to three times more important to the COVs obtained with the ISO 5017. The difference can be explained by the saturation methods used by both standards. For ISO 6275, the saturation is made by the immersion of the sample, while for the ISO 5017 is a vacuum saturation. Both saturation methods have the same aim, but the vacuum saturation is faster and according to COV values, ISO 5017 is more accurate.

Additionally, another study was made for carbonation [3]. The objective was to define more precisely the modalities of implementation of an accelerated carbonation process, in order to ensure the reproducibility of tests. The tested concrete was a B35. The cylindrical samples (4 for each laboratory involved in the study) were poured vertically and underwent the curing process in a wet room for 28 days. The CO_2 rate was of 50%, the preconditioning was made in two parts: saturation and then 2 days of drying at 40°C. The relative humidity was regulated at 65%. Table 2.2 shows the mean value and the coefficient of variation of carbonation depth obtained by 6 different laboratories for different times of carbonation exposure (0, 7, 14 and 28 days).

Table 2-2. Mean value and coefficient of variation of carbonation depth obtained by 6 different laboratories for different times of exposure (0, 7, 14 and 28 days) [3].

Time in days	***B35***	
	Mean (mm)	COV (%)
0	0	0
7	6.8	17.1
14	9	15.7
28	11.7	11.8

As it can be seen, the coefficients of variation are not important, but it can be explained mainly because of the exchange between the gas mixture and the concrete: CO_2 migration and water exchange. The local conditions in the vicinity of the surface of a test sample, the relative humidity of the gas mixture between others, are likely to be influenced by the presence of other test samples located near the studied sample.

To conclude this study, it was suggested that the critical factors to take into account for ensuring the reproducibility of the accelerated carbonation test were: the definition of a fabrication method of test sample, the identification of a preconditioning and the choice of an identical CO_2 content. Moreover, it was suggested to study the comprehension and if any, the control of the interactions, such as water exchange that may exist between different concrete samples during the accelerated carbonation test.

Finally, for assessing the concrete compressive strength by destructive test, many studies have been made considering different factors that can have an influence in the obtained compressive strength value, for instance, the diameter of the cylindrical sample. Neville, in his study [4], concludes that it is necessary to use 3 times more cylindrical samples of 50 mm of diameter than samples of 100 mm. The European program of measurement and testing [5] concludes in their study that samples of 100 mm of diameter have a compressive strength of approximately 7% superior than samples of 50 mm of diameter. Moreover, Nibikin and al. [6] made a study over 300 samples of 50 and 75 mm of diameter for two different kinds of concrete. The conclusion that can be seen in figure 2.1 was that the compressive strength decreases with the augmentation of the *l/d* radio, where *l* is the length and *d* is the diameter of the sample.

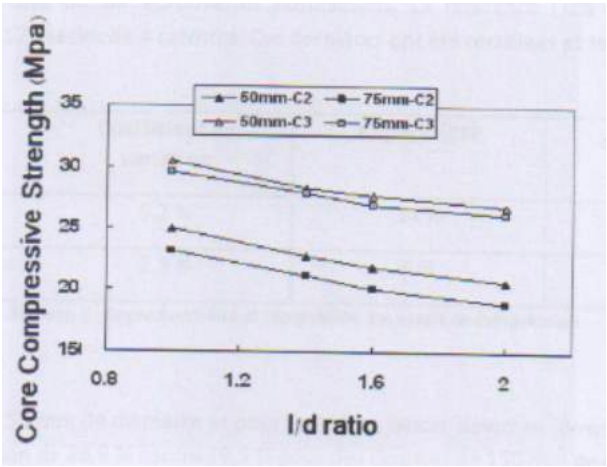

Figure 2-1. Compressive strength from the samples with 50 mm and 75 mm of diameter in function of *l/d* ratio.

Another factor that can modify the compressive strength value is the type of curing. A study made by Lydon et al. [7], compared 48 samples made with 8 different concretes submitted to 3 different curing methods: i) submerged in water at 20ºC, ii) sealed in two layers of plastic film and two of aluminum foil and iii) placed in a room at a constant temperature and humidity (20ºC and 68% RH), named CTHR. Table 2.3 shows that for different curing methods the coefficient of variation of the cubic compressive strength varies between 18 % and 21 %.

Table 2-3. Mean value and coefficient of variation of the cubic compressive strength obtained with different samples summited to the three different curing methods (Water, Sealed and CTHR).

Curing method	***Mean (N/mm^2)***	***COV (%)***
Water	60.8	21.0
Sealed	59.6	18.0
CTHR	57.3	20.4

As it can be seen above, different factors can have a great influence in the moment of obtaining a reliable and constant compressive strength value on samples. This could be confirmed by a study made by COFRAC [8]. Different samples, which diameters vary between 59 and 95 mm were extracted from 3 years old concrete blocks. They were tested by different laboratories to obtain the respective compressive strength value. At the end of the study, the mean compressive strength value obtained was of 38.7 MPa with a COV of around 15%, which is significant.

2.2.2. Destructive testing on samples made with the same concrete structure

The quantification of on-site concrete variability has been of major interest to include it on the models for the prediction of the lifespan of a structure. Notably, the studied indicators to be injected in these models are the mechanic properties, like the compressive strength or the Young's modulus, and durability indicators, such as the water content, porosity, chloride migration, carbonation, etc. The project APPLET [9] developed a large experimental program on two sites: the A86 tunnel on west Paris and the viaduct of Compiègne. Two different kinds of concretes (A1 and A2 respectively for each site) were tested in order to accomplish this objective. Forty cylindrical samples in total were made at the same time the concretes A1 and A2 were poured on their respective sites.

Different test were made in order to characterize both concretes. Table 2.4 shows the mean and coefficient of variation values for: compressive strength, Young's modulus, porosity, water content, chloride migration and carbonation depth for A1 and A2.

Table 2-4. Mean and coefficient of variation values for compressive strength, Young's modulus, porosity, water content, chlorates migration and carbonation depth for A1 and A2 [9].

	A1		***A2***	
	Mean	COV (%)	Mean	COV (%)
Compressive strength (MPa)	83.8	10.5	71.9	12
Young's modulus (GPa)	46.8	6.2	40.8	7
Porosity (%)	12.9	7.9	14.3	7
Water content (%)	4.3	8	4.9	8
Chloride migration coefficient (10^{-12} m^2/s)	2.53	12.4	2.56	21.9
Carbonation depth (Accelerated carbonation) (mm)	4.3	37	10.1	33

As it can be seen, the coefficients of variation are very similar between concretes A1 and A2, except for the chloride migration, which varies by 10% between A1 and A2. This study also allowed establishing a suitable probability density function for each studied property, which would be very useful for probabilistic approaches for service life prediction models. One could select from the database the parameters that are relevant for a new study in terms of physics and chemistry (indicators evaluation) but also for indicators sensitivity: depending on the considered phenomena and the associated modeling some indicators with low variability may have a pronounced influence on the outcome and vice versa. Table 2.5 shows the retained density functions for the different studied indicators.

Table 2-5. Retained density functions for the different studied indicators [9].

Studied indicators	***Retained density functions***
Compressive strength	Lognormal, normal
Elasticity modulus	Lognormal, gamma
Porosity	Lognormal, gamma
Water content	Not available
Chloride migration coefficient	Lognormal
Carbonation depth	Weibull, normal

2.2.3. Destructive test on cores extracted directly from the structure

As it is known, samples made with the same structure's concrete do not reflect the actual structure's state, because these samples are not exposed to the same conditions as the structure (mechanical and environmental). This is the reason for which other studies have been made in order to assess on-site concrete by extracting several cores from a structure element and making destructive tests to obtain the different mechanic and durability indicators.

Such is the case of the Punta Perotti's building in Italy [10]. It was a building of more than 10 years old, exposed to aggressive environmental conditions, such as its proximity to the sea and its location on a windy area. Thanks to its later demolition, a huge experimental campaign could be made to assess the concrete's compressive strength on each floor of this building. A

total of 103 cores were extracted from the interior columns of floors -1 (47 cores) and 2 (56 cores). For both floors, figure 2.2 shows the histogram of the compressive strength and table 2.6 shows the mean and coefficient of variation of the compressive strength.

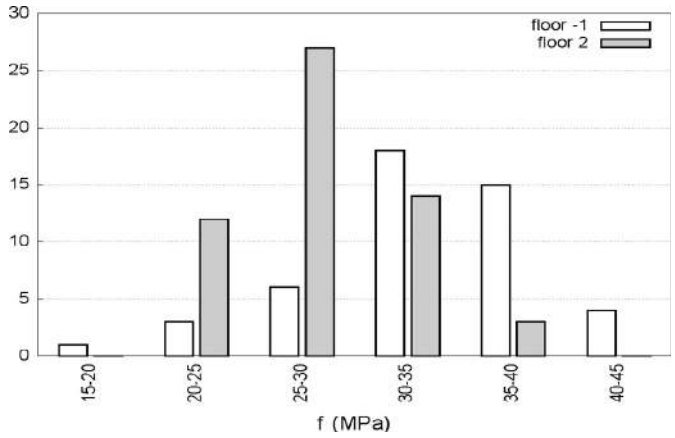

Figure 2-2. Histogram of the compressive strength for both studied floors.

Table 2-6. Mean and coefficient of variation of the compressive strength for both studied floors.

Floor	*Mean f (MPa)*	*COV (%)*
-1	33.0	18.3
2	28.2	14.4

It was expected that the compressive strength at floor -1 was higher, due to its lower location (granulate segregation at the moment of casting). Nevertheless, the coefficient of variation for floor 2 is smaller than the one of the floor -1. This can be explained looking at figure 2.2, which shows greater measurements dispersion for floor -1. From figure 2.2 it can also be observed a normal distribution of the compressive strength for both floors, in accordance to the results found on the table 2.5 from the APPLET project. However, from table 2.5 and table 2.4 it can be concluded, as it was expected, that on-site extracted cores have a coefficient of variation greater than on-site samples.

Another study made by Pucinotti [11], aims specifically to assess the compressive strength of on-site concrete. For this objective, 359 cores were extracted from samples made at the Laboratory for Materials and Structures of the Mediterranean University of Reggio Calabria (Mod IF, Mod AB and Mod CD) and from thirteen existing structures in Italy: four buildings (Mend 1, Mend 2, Mend 3 and Mend 4), three road viaducts (STR3, STR5 and STR7) and six road tunnels (STR1, STR2, STR4, STR6, STR8 and STR9). Structures STR were built in the province of Reggio Calabria between the years 2004 and 2008. Table 2.7 shows the mean and coefficient of variation for each one of the studied elements.

Table 2-7. Mean and coefficient of variation values for each one of the studied structure elements.

Core type	*Mean f (MPa)*	*COV (%)*
Mod IF	26.5	18.9
Mod AB	35.4	17.0
Mod CD	32.9	18.3
Mend 1	21.7	18.5
Mend 2	15.9	25.1
Mend 3	27.6	17.0
Mend 4	36.2	13.1
STR 1	37.8	9.3
STR 2	45.8	13.0
STR 3	38.0	10.5
STR 4	41.9	11.9
STR 5	42.9	15.4
STR 6	32.4	16.5
STR 7	37.2	15.4
STR 8	33.9	7.7
STR 9	37.1	17.7

As it can be seen, for the smallest mean compressive strength value (Mend 2) the coefficient of variation is the highest. However, for the highest mean compressive strength value (STR 5), the coefficient of variation is not the smallest. This can be explained by the difference between the numbers of cores used for each structure. Moreover, the smallest COV values (STR 1 and STR 8) correspond to high compressive strength values above all structure elements mean values, and they also correspond to structures where a high number of cores were extracted (52 and 28 cores respectively). In this study, compared to the previous one, COV values vary significantly and compared with the A1 and A2 concretes (COV sample values from table 2.5), all COV values from table 2.7 are not more important, which indicates the influence of the location and number of the extracted cores at the moment of evaluating a concrete structure indicator. A higher indicator COV can be obtained from the same structure element, rather if the indicator is not homogeneously distributed along the structure element (very different indicator values in different parts of the same structure element), or if the number of cores extracted is too small to be representative.

Another study made by Masi et al. [12], shows the effect of measuring a concrete property in different parts of a structure element. This study compares compressive strength values from cores extracted from different parts of a beam from an Italian school building. The beam was divided in zones, making the difference between the superior and inferior side (E and F), lateral sides (A, B, C and D) and end sides (G and H) at both ends of the beam (Figure 2.3). Moreover, another three zones were discriminated along the beam: beginning, middle and end. A total of 37 cores were extracted from this beam:

- thirteen cores from the inferior part of the lateral side (B-D),
- ten cores from the superior part of the lateral side (A-C),
- six cores from the superior side (E-F) and,
- eight cores at the end sides (G-H).

Figure 2.4 shows their location.

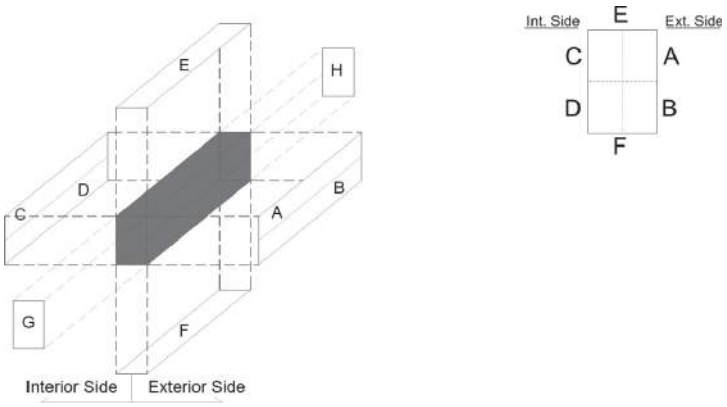

Figure 2-3. Zones of the studied beam.

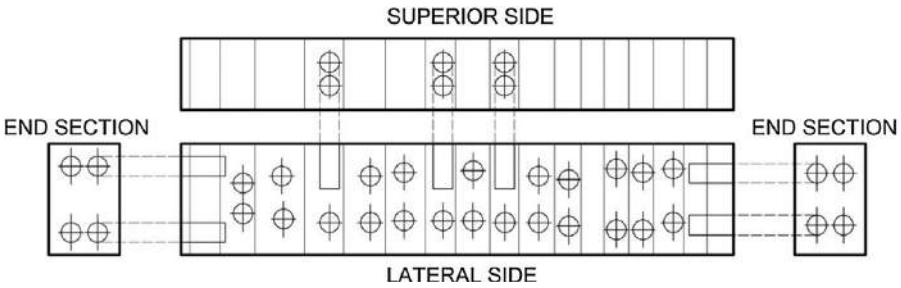

Figure 2-4. Location of the 37 extracted cores.

The mean value of the compressive strength for the beam is 23.1 MPa with a coefficient of variation of 21 %. However, if we take a look at table 2.8, where the mean compressive strength values are discriminated by zones (A-C, B-D, E-F and G-H), it can be clearly seen that the smallest mean value is obtained from the ends of the beam, followed by the mean value at the superior side. This can be explained, because of the solicitations at these parts of the beam for the G-H zone, and due to the effect of consolidation over bleeding for the E-F zone. Moreover, it can be seen that the COV value is the biggest between all zones, which can be explained by the combination of the effect of consolidation over bleeding and the small compressive strength value detected at the beginning of the beam (13.3 MPa).

Table 2-8. Mean and coefficient of variation values of compressive strength for the different studied zones of the beam.

Zone	*Mean f (MPa)*	*COV (%)*
A-C	25.2	14
B-D	25.3	14
E-F	19.5	31
G-H	17.2	18

This study, which discriminates zones of a structure element, shows very clearly that an indicator should not be evaluated with standard statistics (mean, COV, etc.). A more complex study of the variability of a concrete structure element should be made to discriminate critical zones for a diagnosis on a studied structure element.

2.3. Spatial variability of concrete

2.3.1. Introduction

The spatial variability represents the heterogeneity of a studied data set distributed on a studied structure element, such as the amount of erosion on a field or material's properties on a structure element. In the case of concrete, this spatial variability can be represented as variations of mechanical and physicochemical properties, or problematic areas in the elements of a structure. It can result from the intrinsic variability of the material, like the size or nature of the aggregates, its implementation or its exposure conditions, such as the temperature or humidity [13-15]. Determining the spatial variability in a structure would have a great implication on damage assessment of different parts of a structure or for reliability analyzes [16].

Spatial variability on concrete properties can be quantified by destructive, semi-destructive and non-destructive tests. The experimental data is normally analyzed with statistical and geostatistical tools. If spatial variability is determined by standard statistics (mean, COV, etc.), the property's data set of points are considered independent, in other words, each point value is independent from the others. In this case, the property variability is expressed in terms of standard deviation or coefficient of variation. However, most of the time, it can be said that, for a given number of measurements distributed on a surface, two close measurements have a higher similarity than two more distant ones. This spatial dependence can be noted as a spatial correlation, which can be crucial at the moment of reliability calculation for a structure element [17] and, at the same time, it can be represented by a geostatistical function known as the variogram [18].

2.3.2. Spatial correlation: Variogram

The variogram is defined as half the variance of the difference between two data items from two different locations separated by a distance h (Equation 2.1).

$$\gamma(h) = \frac{1}{2} Var[Z(x) - Z(x+h)] \tag{2.1}$$

For a series of observed measurements with a limited series of pairs separated by a distance h (N(h)), an empirical variogram can be determined as:

$$\gamma_e(h) = \frac{1}{2\,N(h)} \sum_{i=1}^{N(h)} Var\,[Z(x_i) - Z(x_i + h)]^2. \tag{2.2}$$

For each empirical variogram, a model can be fitted by the least squares method to obtain a mathematical function that can be used later to compute the expected value of the measurement at any additional point. Figure 2.5 shows an example of a variogram model (spherical type) that can be fitted to an experimental variogram (2.3):

$$\gamma(\mathrm{h}) = (\mathrm{Co} + \mathrm{C}) \left[1.5 \frac{\mathrm{h}}{a} - 0.5 \left(\frac{h}{a} \right)^3 \right] \qquad \text{if } 0 < \mathrm{h} < \mathrm{a}$$

$$\gamma(\mathrm{h}) = \mathrm{Co} + \mathrm{C} \qquad \text{if } \mathrm{h} > \mathrm{a} \tag{2.3}$$

In equation 2.3, three main parameters can be inferred: nugget (Co) that describes the variance of a measurement made several times at the same location (uncertainty due to lack of repeatability), sill (Co+C) that represents the global variance (global variability of the material tested on the structure), and range (a) which represents mathematically the maximum distance where data are correlated.

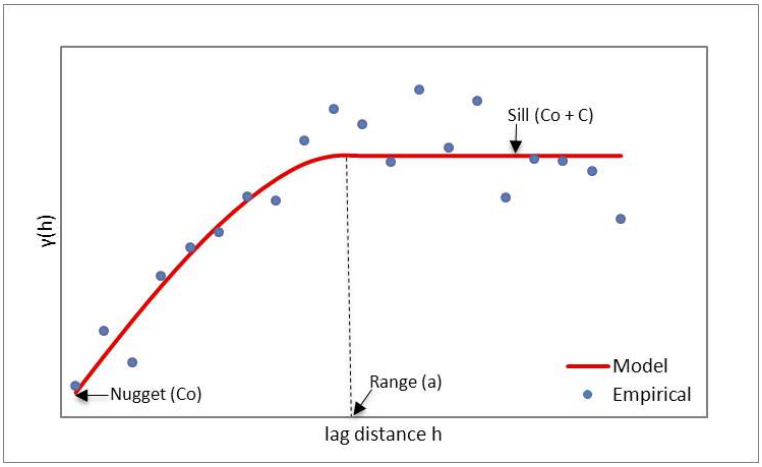

Figure 2-5. Empirical variogram and the fitted model with its parameters.

From figure 2.5, it can be deduced visually the correlation length, which is the real maximum distance where data are correlated. It provides information about the necessary sampling distance, such as to get statistically quasi-independent measurements. There are different variogram models that can be fitted to a certain experimental variogram. The most commonly used, are the spherical, exponential and Gaussian variograms. Its choice is usually

made by experience [19]. Figure 2.6 shows other examples of commonly used variogram models that can be fitted to an empirical variogram.

Name	***Equation***	***Form***
Gaussian	$\gamma(h)=C\left[1-\exp\left(-3\left(\frac{h}{a}\right)^2\right)\right]$	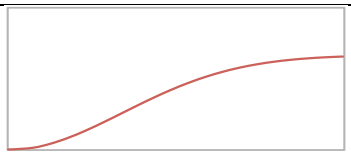
Exponential	$\gamma(h)=C\left[1-\exp\left(-3\frac{h}{a}\right)\right]$	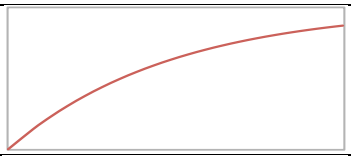
Linear	$\gamma(h)=Ch^b \qquad 0<b<2$	

Figure 2-6. Examples of commonly used variogram models that can be fitted to an empirical variogram.

Other possible way of modeling spatial correlation is by establishing a covariance function. This function, contrary to the variogram, tends to zero when the distance between two points tends towards infinity. This means that the two points values separated a distance h are independent from each other. This covariance function C(h), can be expressed by the equation 4, and it is also in function of the range (a) and the sill C.

$$C(h) = C.\exp\left(-\frac{h}{a}\right) \tag{2.4}$$

Few studies have been made regarding the indicators spatial correlation on a concrete structure element. De Larrard, for instance, made different measurements of porosity (ϕ), coefficient of tortuosity (τ) and the overall thermal activation parameter of the leaching kinetics (k_o), on concrete cores extracted from two vertical and one horizontal line of a concrete wall [20]. His objective was to establish a spatial autocorrelation of properties on the studied wall. Figure 2.7 shows the different covariance functions for the three lines and the three studied properties and table 2.9 shows the different correlation lengths found for the three studied properties. Peculiarly, in this case, the found correlation lengths are the same for the three studied lines. However, due to the low number of measurements made, the correlation lengths and the covariance functions may easily vary with more number of measurements.

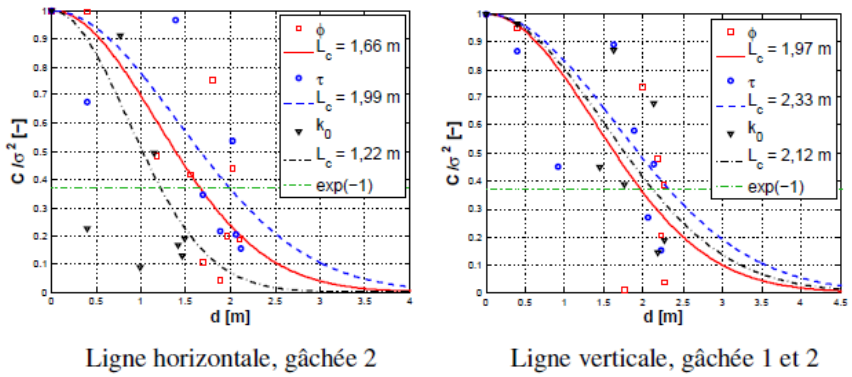

Figure 2-7. Different covariance functions for the three studied lines of the studied wall and the three studied properties (ϕ, τ and k_o).

Table 2-9. Different correlation lengths found for the three studied properties (ϕ, τ and k_o).

Property	***Correlation length (m)***
Porosity (ϕ)	0.4 -2
Coefficient of tortuosity (τ)	1.2 - 2.3
Thermal activation parameter of the leaching kinetics (k_o)	1.2 - 2.1

Another study made by O'Connor [21], aims to model the spatial correlation of surface chloride concentration and the apparent coefficient of diffusion. He did it by making destructive test on extracted cores of a beam from Ferrycarring Bridge in Ireland. Figure 2.8 shows the experimental and fitted Gaussian models with correlation lengths of 1-2 m for both indicators. Only 5 cores were extracted for testing. Hence, the variogram may not be reliable.

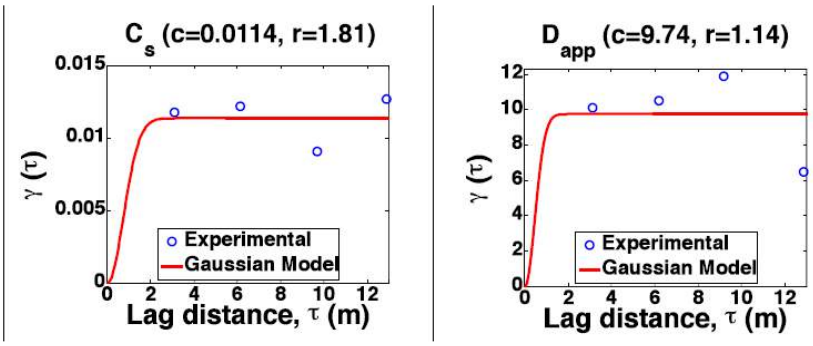

Figure 2-8. Experimental and fitted Gaussian models for the studied indicators: surface chloride concentration (C_e) and the apparent coefficient of diffusion (D_{app}).

The previous studies showed that the spatial modeling of an indicator is made by destructives test on a very few number of samples limiting their reliability. However, NDTs can also be modeled spatially and as they are sensitive to indicators, they can show the spatial

distribution of an indicator indirectly. Nguyen [17], shows an application of spatial modeling of two NDTs measurements (rebound hammer number (RH) and indirect ultrasound velocity (IUV)), on a bridge pile in Marly-France. Figure 2.9 shows the experimental and fitted spherical model for IUV and fitted exponential model for RH. The correlation lengths for both NDTs were of 40 cm. These variograms were estimated with a total of 30 IUV and 24 RH measurements, which makes them more reliable than the ones of the previous studies.

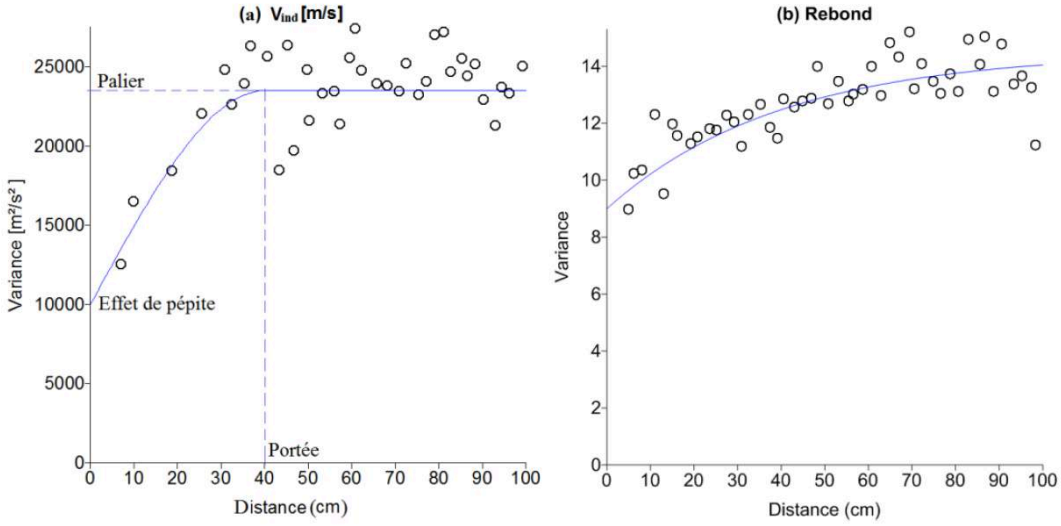

Figure 2-9. Experimental and fitted variograms for the studied NDTs: a) IUV and b) RH.

In these two first sections, it has been studied two ways of evaluating the concrete on a structure element through the variability of its indicator (mechanical or durability): the first one being punctual, concerns the concrete variability as a material and, the second one being continuous, concerns the modeling of the spatial variability of a concrete indicator on a structure element exposed to environmental conditions for a period of time. It is very difficult to dissociate both kinds of variability in the case of concrete. Hence, from now on they would be treated together as one. Besides, the difficulty to make a reliable spatial correlation modeling of a concrete indicator by destructive testing (generally very few number of measurements available) or, the impossibility to evaluate a structure element indicator by only destructive testing, lead us to considerate an alternative by NDT evaluation, which do not compromise the integrity of the studied structure and it is less expensive than destructive testing. Hence, the number of measurements can be increased significantly, increasing also the available information on the structure indicators to consequently increase the quality and reliability of the indicators assessment on a studied structure. However, the results from this section may be useful as a reference to posterior studies related to DTs uncertainty or for the calibration of indicators obtained by the combination of NDTs, in order to improve the NDT evaluation.

2.4. Concrete evaluation by combining NDT methods

2.4.1. Relationship between NDT and indicators

As it could be seen in the previous sections, concrete is a complex material that cannot be characterized like a fabricated material, such as the steel that is mostly homogeneous and its properties are well identified. Several studies have focused on the estimation of concrete indicator variability or the spatial indicator variability of a structure element by destructive tests [2-12, 23-27]. The issue is that to be able to make reliable studies for an entire structure element, it is necessary to extract a huge amount of cores, which can compromise the integrity of the studied structure element. It must also be counted the fact that the extraction of cores to make destructive test can be very expensive.

An alternative way for evaluating concrete indicators is by doing non-destructive tests. These methods are not only less expensive than the destructive ones, but they are also of easy implementation. NDT have traditionally been used on geology, due to the large studied surfaces. Civil engineering applications, most specifically, on concrete structures, were implemented in the nineties mostly to detect defects like cracks or voids in concrete [28-30]. Other more recent studies have focused on the evaluation of an indicator of a concrete structure element by the combination of NDTs and destructive tests (DT) [10, 31-36]. Most of them use one or several NDTs that are sensitive to an indicator. For example, while acoustic methods (e.g., ultrasound) are sensitive to mechanical properties and porosity, electric and electromagnetic methods are sensitive to water content and chloride contamination. However, to link a NDT to an indicator, it is important to choose correctly the information of the technique that is going to be useful to determine the required indicator. In the case of compressive strength, ultrasound pulse velocity (UPV) and rebound hammer number (RH) are often used together with some DTs to establish a correlation law. This is because UPV and RH are recognized to be sensitive to mechanical concrete properties. The use of both methods together reduces the uncertainty on compressive strength evaluation.

The problem of using NDTs is that even if they are related to the indicators, their relation to them is not constant. This is due to uncertainties encountered related to several factors like: material and exposure heterogeneities, limited measurement precision or quality of available data, and model uncertainties due to simplifications [37]. Breysse made a review of the assessment of concrete strength by ultrasound pulse velocity and the rebound hammer number by taking into account several correlation laws obtained in different studies [38]. The most common ones are the power law, linear law, polynomial and exponential laws (Table 2.10). None of the laws are related to each other and, besides, the results obtained have a degree of uncertainty. This study demonstrates that there is no universal law to assess the compressive

strength on concrete or any other indicator and that a model is established only from the actual measurements. Moreover, the quality of the assessment strongly depends on the model used and the quality of measurements.

Table 2-10. Number of existing models in the literature for concrete strength estimation [38].

Model type	***Form***	$f_c = f(US)$	$f_c = f(R)$
Exponential	$X = a\, e^{bY}$	26	8
Power	$X = a\, Y^{b}$	17	31
Linear	$X = a\, Y + b$	18	28
Polynomial (2)	$X = a\, Y^{2} + b\, Y + c$	6	15

In France, in order to approach this problem in a more objective way, a national project called SENSO was implemented [39]. The objective of this project was to establish correlation laws between NDTs and indicators. For this aim, several laboratory samples were made, with different kind of concretes and different saturation degrees. Several NDTs were used and by means of a statistical analysis the most relevant NDT information/measurements were selected. These relevant measurements are called *Observable.* Five non-destructive methods and 17 observables were chosen after a large database analysis [40]. Table 2.11 shows the different observables chosen and their sensibility to the indicators (porosity, saturation degree and compressive strength).

It is to be expected that all chosen observables have not the same reliability. To assess the quality of each observable, one must be able to determine the uncertainties of measurements for each observable. A measurement may be wrong, thus, it must be removed from the calculation. It can also be imprecise (noise measurement) or, it can be inconsistent (drift on the measurements) [41]. These uncertainties on the observables measurements can lead to a low quality of the established correlation law. However, these uncertainties can be limited by increasing the number of measurements in a limited area considered homogeneous, or by eliminating imprecise and extreme values.

Table 2-11. Chosen observables and their sensitivity to the indicators studied at the SENSO project (porosity, saturation degree and compressive strength).

			Indicators	***Saturation degree***	***Porosity***	***Compressive strength***
Laboratories	***Technique***	***Code***	***Observable***			
EC Lille	Ultrasound	US-moy	Surface Ultrasound - Average velocity (m/s)	LS	S	S
IFSTTAR	Ultrasound	US-ap	Surface Ultrasound - Apparent velocity (m/s)	LS	S	S
IFSTTAR	Ultrasound	US-1cm	Surface Ultrasound - Wave velocity 1 cm (m/s)	LS	S	S
IFSTTAR	Ultrasound	US-3cm	Surface Ultrasound - Wave velocity 3 cm (m/s)	LS	S	S
LMA	Ultrasound	UP-250	Ultrasound Pulse - 250kHz transmission velocity (m/s)	LS	S	S
EC Lille	Ultrasound	US-at	Surface Ultrasound - Average attenuation (dB/m)	LS	S	S
IFSTTAR	Impact Echo	IE-Edyn	Impact Echo - Dynamic modulus of Young (GPa)	NS	S	S
IFSTTAR	Impact Echo	IE-VP	Impact Echo - Compressive waves velocity (m/s)	NS	S	S
IFFSTAR	CAPA	Ca-gel	Capacity of large electrodes - Permittivity	S	NS	NS
IFFSTAR	CAPA	Ca-mel	Capacity of medium electrodes - Permittivity	S	NS	NS
I2M	Resistivity	Re-5cm	Log of the quadrupole resistivity 5 cm	S	S	NS
I2M	Resistivity	Re-10cm	Log of the quadrupole resistivity 10 cm	S	S	NS
LMDC	Resistivity	Re-We5	Wenner resistivity 5cm	S	S	NS
LMDC	GPR	Ra-ampl	Pic to pic amplitude	S	NS	NS
LMDC	GPR	Ra-VTo	Direct wave GPR velocity (cm/s)	S	NS	NS
IFFSTAR	GPR	Ra-VNa	Direct wave GPR velocity (cm/s)	S	NS	NS
IFFSTAR	GPR	Ra-te15	Time of arrival, offset 14.7 cm	S	NS	NS

NS: Not sensitive

LS: Low sensitivity

S: Sensitive

The mentioned uncertainty on NDT's observables can also be quantified by the variability. This can allow the estimation of the number of measurement necessary to obtain a punctual value with a given confidence level [42-43].

Three kinds of variability were identified on the ACDC and SENSO French projects [17], which represents different scales of the NDT studied:

- *Punctual*, which represents the repeatability of the measurements made on the same point. It reflects the measurement error due to the equipment, the study protocol, or environmental conditions at the moment of the measurements, like the temperature or the humidity.

- *Local*, which represents the intrinsic variability of the concrete at a local scale or the reproducibility of the measurements. It reflects the concrete's heterogeneity due, for example to the casting.

- *Global*, which represents the concrete variability on a larger scale, like a concrete batch.

As the correlation laws were established for a limited range of validity, not all the possible concretes are included in these estimated correlation laws. Nevertheless, it is always possible to estimate out of the valid range, but the quality of the estimation decreases with the increment of the validity field interval. Thus, for another concrete not included for estimating the correlation laws, for example an in-situ concrete, a calibration process should be required.

The calibration is normally based on DTs made on extracted on-site cores. However, as mentioned before, their number must be limited, thus, the importance of their pertinent location. Two approaches are proposed by the EN 13791: the correlation (A) and the calibration (B). The approach A consists on identifying a specific law in the form of a correlation curve based on experimental measured data and, the approach B consists on recalculating the estimated value by a chosen law (already defined). In the study mentioned above and made by Breysse [38] based on synthetic data simulations it is shown, that for a number of cores (N) higher than 5, approach A is more reliable. For N equal to 5, both approaches have the same reliability. For N between 3 and 4, approach B is more reliable. Finally, for N between 1 or 2, it is only possible to use approach B, but the uncertainty can be pretty high.

Studied observables may also be sensitive to several indicators simultaneously as shown in table 2.11. When the variability of these indicators is not controlled, the value obtained directly of the evaluated indicator can have a high uncertainty. Hence, to improve the correlation between the studied indicator(s) and the NDTs, studies on the combination of NDTs have been

made since the sixties. Malhotra cited in his paper [30], that a higher correlation is expected if the ultrasonic and rebound methods are combined for the determination of compressive strength, rather than use them separately.

However, combining the methods does not prevent them from technical limitations attached to each one of them. The quality of an evaluation can be affected by several factors. Such as, the characteristics of the inspected concrete, the spatial or temporal (evolution) variability of the concrete indicators, the form of the correlation law used, and errors related to measurements if measurement conditions are not well controlled.

As it is the case for one technique, the interest of a combination must be weighed against the evaluation quality, the increased cost related to the number of measurements and to "expensive" methods, the technique accessibility for constrained auscultation, and the complexity in the interpretation of the results.

The following sections describe three combination methods used in the frame of ACDC, SENSO and EVADEOS projects to assess the indicators on auscultated concrete structures: response surface, data fusion and neural network. These approaches will be detailed, as well as their interest and applications will be mentioned.

2.4.2. Response Surface

A response surface (RS) studies the relationship between several input variables (x) and one or more response or measured variables (y) [44]. The input variables “x” are characterized by a set of recorded statistical information as distribution functions (which could be correlated or not), standardized moments, etc. These are generally spatial-temporal processes, called stochastic processes and they are reduced to random variables when time and space indices are fixed.

Usually the response is unknown, but it can be represented by a low-degree polynomial model:

$$y = f'(x)\beta + \epsilon \tag{2.5}$$

Where β is a vector of unbiased ordinary least-squares estimators of the same size as x and $\in$ is a random experimental error. Two principal models are generally used in RS:

- The first-degree model that is used generally as multiple regression:

$$y = \beta_0 + \sum_{i=1}^{k} \beta_i x_i + \epsilon \tag{2.6}$$

- And the second-degree model:

$$y = \beta_0 + \sum_{i=1}^{k} \beta_i x_i + \sum \sum_{i<j} \beta_{ij} x_i x_j + \sum_{i=1}^{k} \beta_{ii} x_i^2 + \epsilon \tag{2.7}$$

The idea is to use a sequence of designed experiments to obtain an optimal response. The surface design can be represented as a design matrix (D) of order n x k (n: number of variables, k: number of measurements):

$$\mathcal{D} = \begin{bmatrix} x_{11} & x_{12} & \dots & x_{1k} \\ x_{22} & x_{22} & \dots & x_{2k} \\ . & . & \dots & . \\ . & . & \dots & . \\ . & . & \dots & . \\ x_{n1} & x_{n2} & \dots & x_{nk} \end{bmatrix} \tag{2.8}$$

An easy way to estimate a first-degree polynomial model is to use a factorial design [45]. This would be enough to determine which independent variables have an impact on the response variable(s). Once the significant independent variables are determined, a more complicated design, such as a central composite design [46] can be implemented to estimate a second-degree polynomial model, which continues to be just an approximation. However, the second-degree model can be used to optimize (maximize, minimize, or attain a specific target), such as the minimization of the response prediction variance.

This kind of combination method, have been used in different fields for different objectives. For example, to enhance surface layer properties of aircraft aluminum alloy by shot peening [47] or to optimize the laser cutting parameters for composite [48]. In the geology field, RS has been used for probabilistic assessment of rock slope stability [49] or for practical geotechnical reliability analysis [50]. In the case of concrete, RS is mostly used for optimizing a concrete mixture to enhance some properties of specific concretes (e.g. alkali-slag concrete, ASR concrete, concrete containing paper mill residuals, concrete with hybrid blends of metakaolin and fly ash, foam concrete, steel fiber reinforced concretes, etc.), like fracture properties, process improvement, density, strength or ductile behavior [51-62].

RS has not been used frequently for concrete evaluation by the combination of NDTs. A study made by Sbartaï et al [63], aims to evaluate the compressive strength and water content of a concrete by the combination of GPR, electrical resistivity and ultrasonic pulse velocity. In this study, the SENSO project database was used to train and test the RS. The entire database was used for training the RS, but to validate the results, only a part of the SENSO database was chosen (testing data). A full quadratic response surface (with cross terms) is used because of the mathematical form of the correlations between the observables of NDT methods (e.g.

ultrasound pulse velocity) and studied indicators (compressive strength and water content). For the training database, good correlation can be observed (Figure 2.10) between actual data and the data calculated by RS.

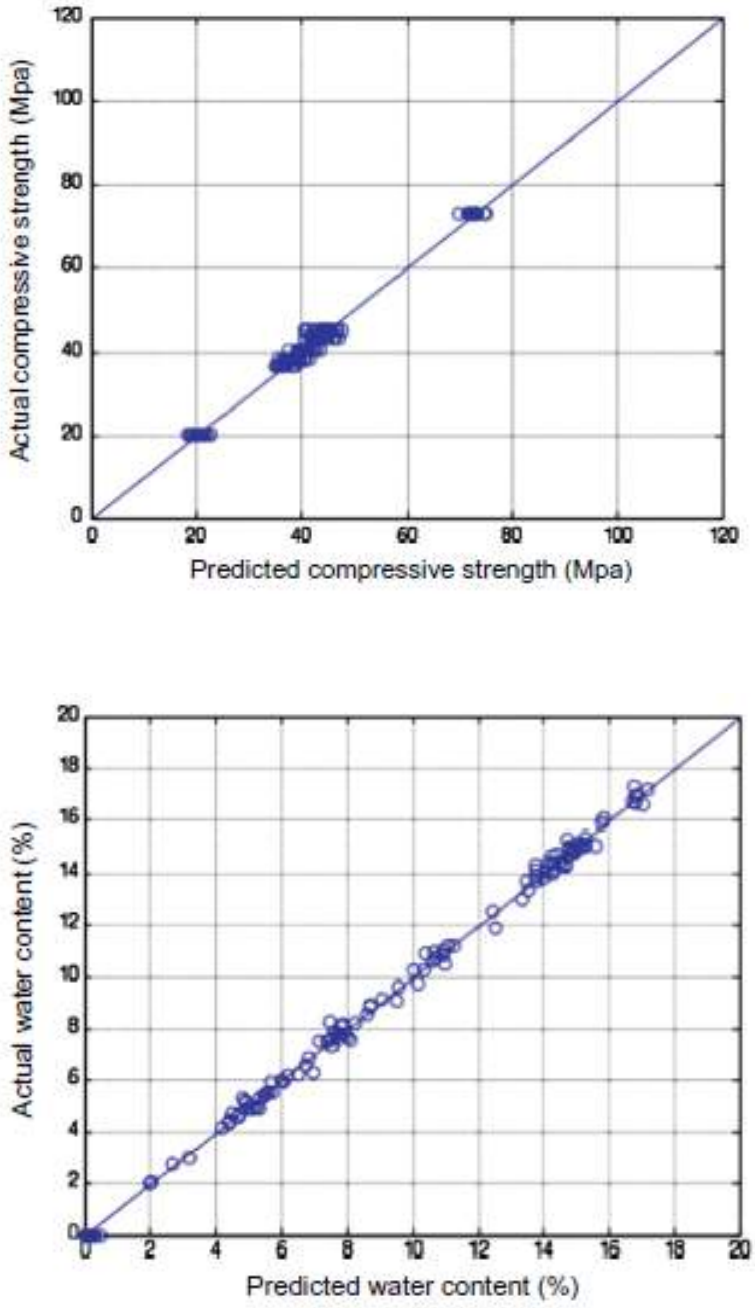

Figure 2-10. Correlation between actual data and the data calculated by response surface for the training database [63].

However, on the testing database, the correlations are not as good. Figure 2.11 shows that the correlations are more dispersive on the testing database for both compressive strength and water content. It is also important to highlight that the RS tends to over-estimate the compressive strength.

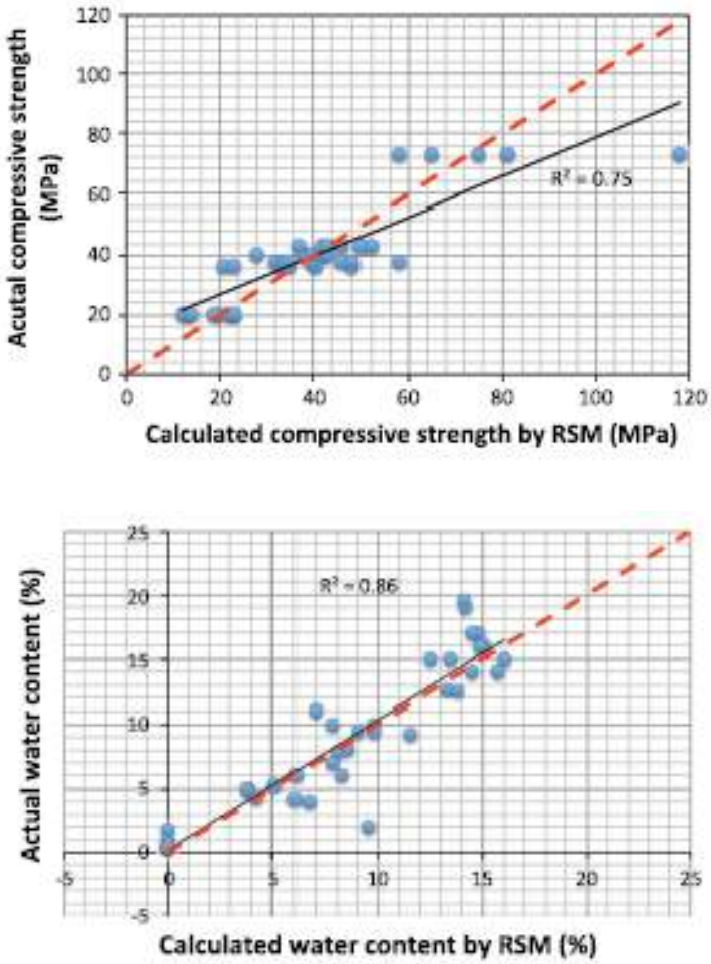

Figure 2-11. Correlation between actual data and the data calculated by response surface for the testing database [63].

2.4.3. Data Fusion

Data fusion is the integration of data as a combination of multiple sources to obtain improved information (less expensive, of higher quality or more relevant information). There are two terms commonly used to refer to data fusion: one is *information fusion*, which is employed mostly to define already processed data, and the other is *data fusion*, which is used for raw data [64].

The data fusion methods can be classified into three principal categories: data association, state estimation and decision fusion.

The data association methods must determine the set of measurements that correspond to each target. The goal is to establish a set of observations or measurements that are generated by the same target over time.

The state estimation methods aim to determine the state of the target under movement (normally the position) given by the observations, like the case of sensors. They are also

known as tracking methods, but in their general form it is not sure that the target information are relevant. This means that some of the observations could come from the target and the others could be noise. The goal is to obtain a global target state from the observations.

Finally, the decision fusion methods are based on the knowledge of the perceived situation, which is provided by many sources of data. These methods aim to make a relevant conclusion about the events and activities that are produced from the detected targets. These methods often use symbolic information, and they must give a pertinent result considering the uncertainties and constraints.

The choice of the technique can be made according to the following criteria:

- Considering the relationships between input data sources that can be defined as: complementary (when the information provided by the input sources represents different parts of the scene and could then be used to obtain more complete global information), redundant (when two or more input sources provide information about the same target and could then be fused to increment the confidence), or cooperative (when the provided information is combined into new information that is typically more complex than the original information).
- Considering the input/output data types and their nature.
- Considering the abstraction level of the employed data: raw measurements, signals, characteristics or decisions.

In most data fusion methods, the input information (numerical or symbolic) is represented as a degree of confidence in an event with real values, taking into account the imprecise, uncertain, and incomplete nature of the information [65]. This degree of confidence is represented as a behavior operator, which can be context dependent, context independent variable and context independent constant.

The *context dependent* operators rely on a global knowledge or the sources to be fused (conflict between the information given by the sources or reliability of the different sources). These kinds of operators are interesting for classification problems, since they are adaptable. The *context independent variable* operators may be independent of the context, but their behavior depends on the information to combine. Lastly, the *context independent constant* operators have the same behavior whatever the values of the information to fuse. Moreover, they are treated without any contextual or external information. They are also used on the three most commonly used data fusion formalisms, which are the probabilistic and Bayesian theory, the fuzzy sets theory and the possibility theory.

The *probabilistic and Bayesian theory* takes into account the information intrinsically statistical by nature [65]. Its degrees of confidence are represented by probabilities. If we consider E an event to be evaluated an x_1 and x_2 the pieces of information provided by two different sources, from the Bayes theorem we have:

$$\begin{aligned} p(E \mid x_1, x_2) &= \frac{p(x_2 \mid E, x_1)p(E \mid x_1)}{p(x_2 \mid x_1)} \\ &= \frac{p(x_2 \mid E, x_1)p(x_1 \mid E)p(E)}{p(x_2 \mid x_1)p(x_1)} \\ &= p(x_2 \mid E, x_1)p(x_1 \mid E)\frac{p(E)}{p(x_1, x_2)} \\ &= p(x_1 \mid E, x_2)p(x_2 \mid E)\frac{p(E)}{p(x_1, x_2)}. \end{aligned} \tag{2.9}$$

The operator involved is a product of probabilities, which is conjunctive. The term $p(x_1,x_2)$ is normalized, hence, constant for all events. In the case of independent sources, the expression on equation 2.9 would be reduced to:

$$\frac{p(x_2 \mid E)p(x_1 \mid E)p(E)}{p(x_1)p(x_2)} \tag{2.10}$$

The *fuzzy set theory* is used when the information included is uncertain. This means that the information given is between the *true* and *false* states. True can be represented by 1, and can also mean *belongs.* On the contrary, false can be represented by 0, and it can also mean *does not belong*. Examples of fuzzy sets can be the size of a person [41], or the state of the temperature [66]. Figure 2.12 shows the difference in the representation of classic sets and fuzzy sets for the state of temperature.

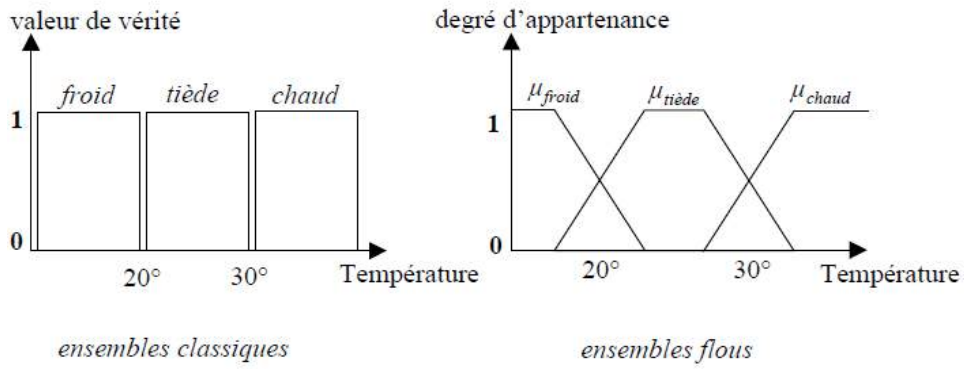

Figure 2-12. True values for the theories of classical and fuzzy sets.

Essentially, the classic sets are a simplified version of fuzzy sets, where the value of temperature can only be 1 or 0. Hence, a temperature value (X) can only belong to one of the three sets (Ω): cold (froid), warm (tiède) and hot (chaud). However, in the case of the fuzzy sets, X can belong to two sets at the same time (cold-warm or warm-hot). Each set is

characterized by a membership function (μ_{cold}, μ_{warm} and μ_{hot}), and the degrees of membership associated with each element $\mu\Omega_{cold}$, $\mu\Omega_{warm}$ and $\mu\Omega_{hot}$, are included between 0 and 1. There is no general method to obtain these functions. It is more of a subjective choice made by an expert in the field. The algorithm of Fuzzy C Means is commonly used, which is based on the minimization of a criterion of classification. Fuzzy sets essentially represent imprecise information. Uncertainty is accessible only by the deduction of different membership functions.

A way of deducing the membership functions is by the *theory of possibilities*. A fuzzy set represents a restriction on the variable X, which in this case is the temperature. This restriction is associated to a possibility distribution (Πi_x), and it is defined to be numerically equal to the membership function (uF), which means that its value also varies between 0 and 1.

A membership function is not a measure of confidence on fuzzy sets. This is why the use of possibility theory can be justified [67]. There are two confidence measurements:

- The measure of possibilities that is used when fuzzy sets are concordant:

$$\Pi(A \cup B) = \max(\Pi(A), \Pi(B)) \tag{2.11}$$

- The measure of necessity that is used when the fuzzy sets are not concordant:

$$N(A \cap B) = \min(N(A), N(B)) \tag{2.12}$$

The possibility Π and necessity N are respectively defined from the possibility distribution for an event $A \subset \Omega$ by the equations 22 and 23, with A^C as the opposite event of A. These measures offer great flexibility in modeling because they have not undergone the constraints imposed initially by the probabilities.

$$\Pi(A) = \sup\left\{\pi(x), x \in A\right\} \tag{2.13}$$

$$N(A) = \inf\left\{1 - \pi(x), x \notin A\right\} = 1 - \Pi(A^C) \tag{2.14}$$

Normalization constraints are introduced in the theory of possibilities, but they are lower than in probability theory. One of the two measurements (need or possibility) is always located at one end of the interval [0, 1]. These constraints are described in the following equations:

$$\sup\left\{\pi(x), x \in \Omega\right\} = 1 \tag{2.15}$$

$$\Pi(A) < 1 \Rightarrow N(A) = 0 \tag{2.16}$$

$$N(A) > 0 \Rightarrow \Pi(A) = 1 \tag{2.17}$$

$$\max\left\{\Pi(A), \Pi(A^C)\right\} = 1 \tag{2.18}$$

$$\min\left\{N(A), N(A^C)\right\} = 0 \tag{2.19}$$

In the theory of fuzzy sets and possibilities, one of the advantages is that symmetrical sums and operators considering the conflict or reliability of the sources are possible. The most common operators are T-norms, T-conorms and medium [68]. A common feature of these operators is that they provide a result of the same nature as the starting functions and thus has the same interpretation in terms of imprecision and uncertainty. Moreover, they can take no partial binary decision before the combination, which could complicate the overcoming of contradictions. The decision is taken after obtaining the result of the combination. The choice of a fusion operator can be based on the criteria proposed by Bloch [69]: the behavior of the operator, the properties assigned to the operator, the relative behavior to conflict situations, and the ability to discriminate different situations.

The first applications of data fusion concern mainly multi-sensor military applications [70-71]. In 1994, the terminology related to NDT data fusion was first introduced, but was thought to be too complex [72-73]. However, with time and because of the growing interest of the aerospace and nuclear industries, NDT data fusion became more easily accepted and started to move from the laboratory to reach on-site testing. Nowadays, NDT data fusion is used in a wide range of NDT methods applications. For instance, increasing the expertise of natural risks by mixing fuzzy logic and evidence theory [74]. Other application on non-concrete materials would be to facilitate signal interpretation and to increase defect detection and characterization of a carbon fiber reinforced composite material [75]. In this study, they used data fusion processes of eddy current and infrared thermography based on statistical and probabilistic algorithms.

In the case of concrete, data fusion has been used for improving the effectiveness of the GPR and ultrasonic pulse echo technique due to the automated measurements on bridges. Additionally, the high potential of reconstruction and data fusion was demonstrated for the improvement and simplification of the interpretability of large data sets measured with impulse-echo methods [76]. Furthermore, the multi sensor data fusion approach has been used for automatic honeycomb detection in concrete [77]. For this study, they combined impact-echo, ultrasonic pulse echo and GPR data using the Dempster's rule of combination and the Hadamard product.

Two studies about the evaluation of durability indicators on concrete elements using the theory of possibility have been made [78-79] during the French SENSO project. In this context, Ploix et al. [79] made a study to estimate simultaneously two pairs of indicators: saturation degree and porosity, or saturation degree and young's modulus, for undamaged concretes, under laboratory conditions. These estimations are obtained by a method based on the theory of possibilities and fuzzy sets. As this method is then used for further studies on this thesis, its principle is going to be described as follows:

First, linear correlation laws between the observables of table 2.11 and each of the studied pair of indicators pair are obtained. Then, the fuzzy set membership functions for each observable are created using the theory of possibilities, called *distribution of possibilities*.

These distributions of possibilities have a trapezoidal form and are composed of two principal parameters:

- a (equation 2.20), which depends on the local variability of the observable's measurement and defines the width of the distribution.

$$a = \left(\frac{\sigma\sqrt{6}}{\sqrt{1+\beta^2}}\right) \tag{2.20}$$

- and β, which is a number between 0 and 1, which assess the slopes and the width of the set that is equal to 1. For further studies, the value of β is equal to 0.2.

Figure 2.13 shows an example of the distribution of possibility function for a measured central frequency of direct radar wave of 1.1 GHz.

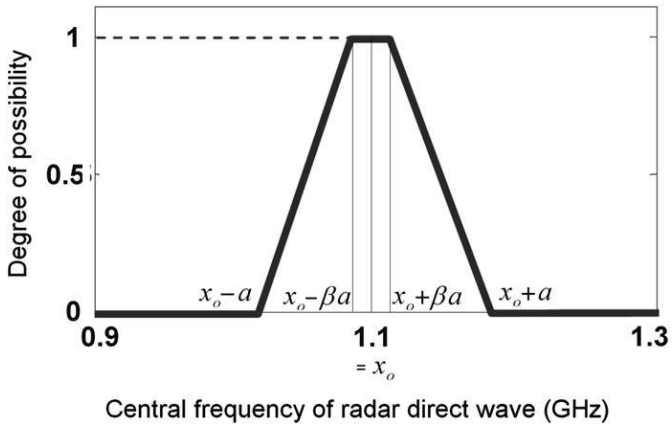

Figure 2-13. Example of the distribution of possibility function for a measured central frequency of direct radar wave of 1.1 GHz.

Then, using the extension principle, this distribution of possibility function is expressed in terms of the studied pair of indicators (equation 2.21), as it is illustrated in figure 2.14 for porosity (P) and saturation degree (S).

$$\pi_{indic}(P,S) = \pi_{param}(Q_i)\,|_{Q_i=\Phi_i(P,S)} \quad (2.21)$$

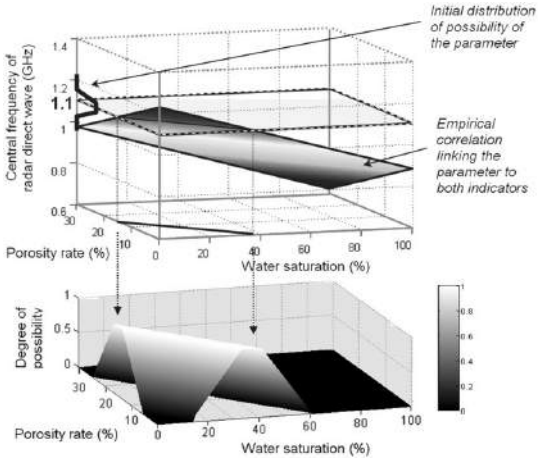

Figure 2-14. Extension principle for porosity (P) and saturation degree (S).

For the fusion process, the adaptive operator obtained by Delmotte (equation 2.22) was used. Its definition implies that its global behavior will be disjunctive (max), if only a few sources are reliable and/or inconsistent, and on the contrary, conjunctive (min), if most of the sources are reliable and/or consistent.

$$\pi_o(P,S) = (1-\alpha^2)\ \max_i\left(t_i\pi_i(P,S)\right) + \alpha^2 \min\left[\min_i\left(1-t_i\pi_i(P,S)\right), \max_i(\pi_i(P,S))\right] \quad (2.22)$$

In equation 2.22, α is the average reliability over all sources and t_i is the global reliability (equation 2.23), which is composed of:

- The *proper reliability* (t_i^{proper}), which corresponds to the general ability of the source to evaluate unknown parameters,
- And the *concordance reliability* (t_i^{conc}), which represents the degree of agreement of one source's data with all of the other sources.

$$t_i = \frac{1}{2}\left(t_i^{conc} + t_i^{proper}\right) \quad (2.23)$$

Finally, to obtain a solution for P and S, or any other pair of indicators, two decision criterions were used: the *maximum criterion*, which provides the solution where the values of indicators reach 1 for the degree of possibility. Also, the *threshold criterion*, which provides a set of solutions for a degree of possibility greater than a chosen threshold. Figure 2.15 shows an example of the decision criteria for a resulting distribution for P and S.

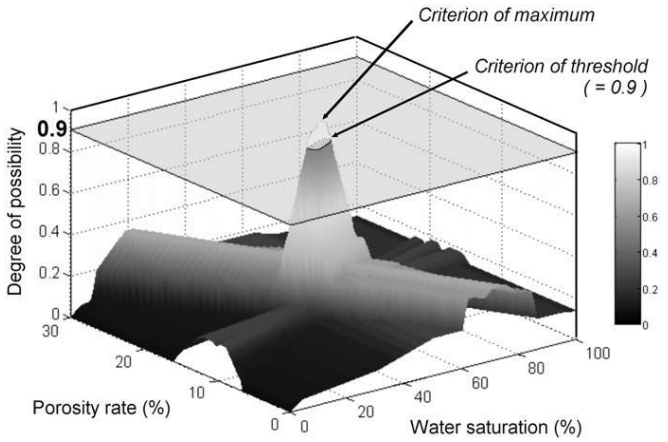

Figure 2-15. Example of the decision criteria for a resulting distribution for P and S.

The quality of the results is then evaluated by a quality estimator (EQ) [80], which allows quantifying both, the quality and the reliability of the indicator evaluation. This estimator is based on the morphology of the possibilities surface produced by data fusion and more specifically on the emergence of the peak solution as shown by "h_s" in figure 2.16.

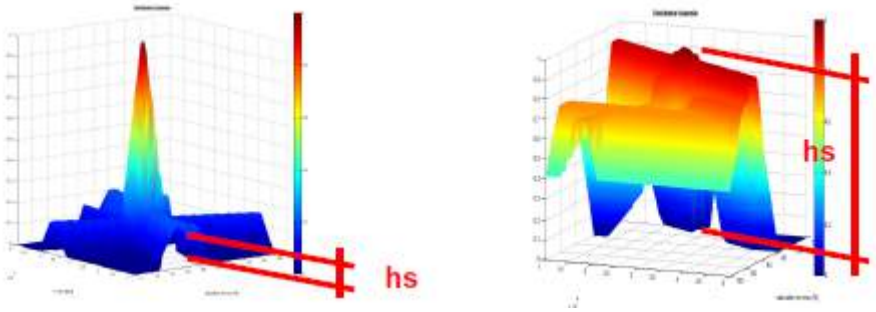

Figure 2-16. Fusion of the three distributions of three observables in the space with 2 indicators a) coherent distributions b) non coherent distributions.

Quality assessment is associated with the consistency of the information obtained from the observables and not with the absolute value of the indicator. Smaller the hs, better the quality EQ of the indicators estimation and more reliable the information.

Villain and al. [78], tested this method to estimate the indicators: porosity (P) and chloride content (Cl) on a concrete beam from a wharf in a tidal zone of the Nantes–Saint-Nazaire Port. Three observables were combined: capacitive large-sized electrode permittivity, GPR wave velocity and impact echo frequency to obtain the targeted indicators. Moreover, to this aim, three inversion methods were used: one based on a matrix inversion of the complete model, a second based on a 2D graphical solution and the last one based on a 2D-data fusion process. Similar results were obtained with all three methods, but the result of the data fusion method showed a satisfactory porosity prediction (12.2%), and an estimated chloride content value too low (-0.07 g/100 g). Figure 2.17a and b, shows the fusion distribution before fusion (2D) and

after fusion (3D). It can be noted that the three observables converge even though the result for Cl does not correspond to the expected result.

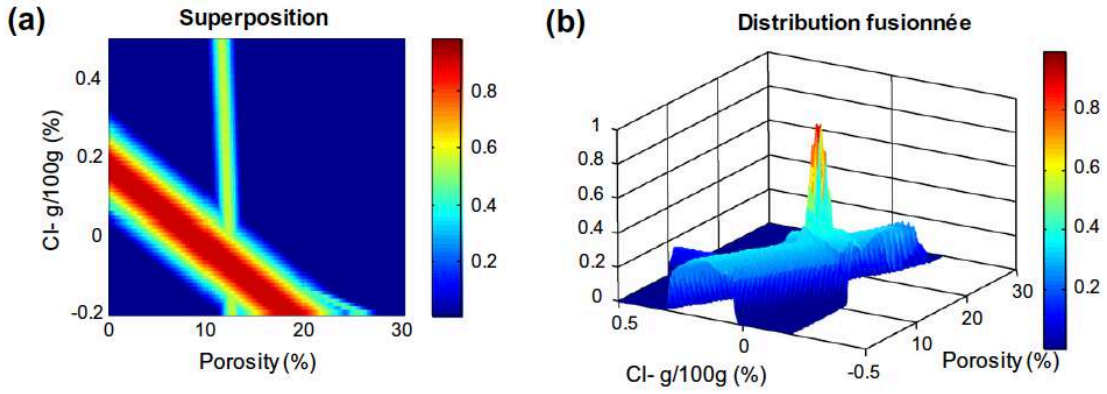

Figure 2-17. Fusion distributions for the wharf beam (a) Before fusion in 2D and (b) After fusion in a 3D perspective.

This on-site application shows that the linear regression curves of NDT methods on a specific concrete cannot be directly used on another unknown concrete (even if it appears to be very similar in description). Consequently, calibration procedures including the inputs and outputs of the data fusion tool may be proposed in order to design new regression curves that are adapted to the test structure, improving the quality of fusion results. Additionally, another calibration procedure including the analysis of several cores from the studied structure can be made in order to adjust fusion results to it. In order to do this, it is also important to overcome the uncertainties of uncontrolled concrete parameters obtained by NDTs and DTs that significantly alter the dependence between the NDT and the indicator.

2.4.4. Artificial Neural networks

The Artificial Neural Networks (ANN) is a statistical method that tries to simulate the learning capacity of the brain. It is non-parametric, which means that the adjusted model's parameters do not have a physical meaning, and can work with non-linear models, which makes it flexible and able to respond to decision support, diagnosis and prediction issues.

The base of the ANN is the artificial neuron (figure 2.18). It is represented by an activation function (F), which depends on the inputs (X), the bias term (b), and the attributed input weights (w_i). The activation function can take different forms, normally non linear. Table 2.12 shows the most commonly used activation functions.

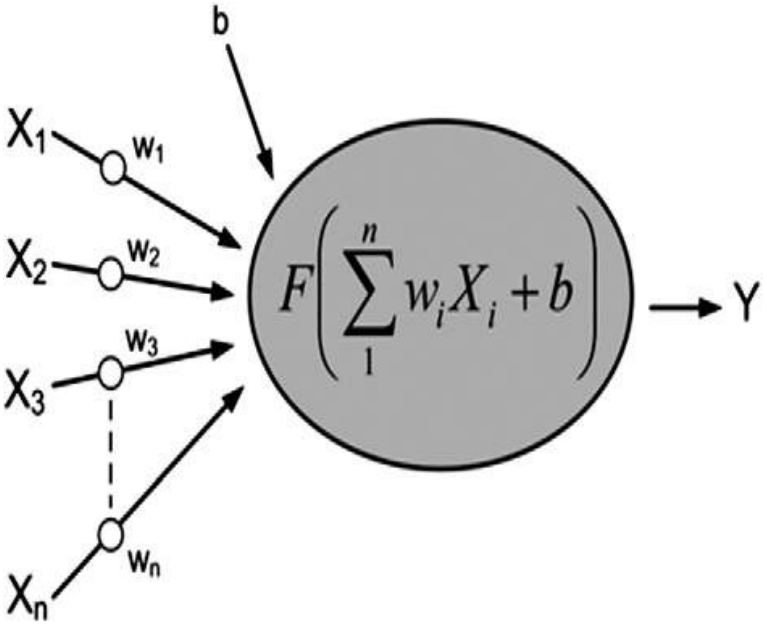

Figure 2-18. Artificial neuron.

Table 2-12. Most commonly used activation functions.

Name	***Equation***
Linear	f (S) = S
Hyperbolic tangent	$f(S) = \frac{e^{S} - e^{-S}}{e^{S} + e^{-S}}$
Sigmoid	$f(S) = \frac{1}{1 + e^{-S}}$

The association of several neurons is called artificial neural network. The most commonly used is the Multi-Layer Perceptron (MLP), where the information travels in a unique sense, form the inputs to the outputs. It is composed from three layers minimum, which are:

- The *inputs layer* that is composed of the inputs.
- The *hidden layer*, which is composed from the neurons.
- And the *output layer*, which is composed from the outputs.

The idea is to introduce input and output data to the ANN, and to make it learn the relationship between both through a process called training. It is usually done in five steps illustrated in figure 2.19. The objective of this process is to find the most accurate weights that minimize the error between the theoretical output and the one calculated by the ANN. For this, a series of steps must be followed:

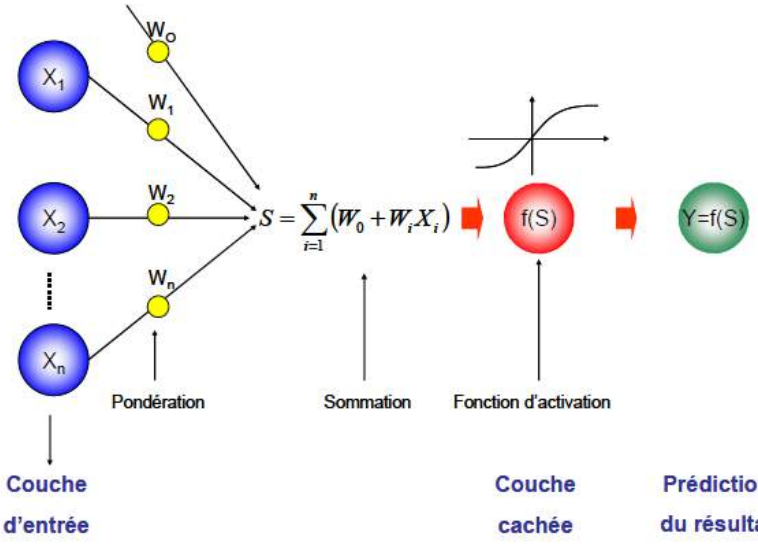

Figure 2-19. Learning process and functioning of ANN.

(i) ***Data structuration:*** A database composed from pertinent inputs and their respective outputs must be divided in three smaller bases: The first one is the *training base*, which is the one used for the training process. The second one is the *test base*, which is used to control and to stop the training process. Finally, the third one is the *validation base* that is not involved in the training process, which means that it will be useful to test the ability of the trained ANN for unknown data.

(ii) ***Learning process:*** It consists on adjusting the parameters w_i and b from the activation functions of the neurons, in order to minimize the error between the ANN's estimated outputs and the targeted outputs. The most used error is the Mean Square Error (MSE) and the algorithm most used is the back propagation of the gradient error. This algorithm is based on the calculation of the error gradient, and aims to minimize the output error of the network by changing the weight. The gradient of the error denoted E_n, is calculated as follows:

$$\nabla E_{n/W} = \frac{\partial E_n}{\partial W} \tag{2.24}$$

Where W is the weight matrix. The new weights of the matrix W in step (n +1) are then calculated by the equation 2.25, where η is the training step.

$$W_{n+1} = W_n - \eta \nabla E_{n/W} \tag{2.25}$$

The advantage of ANN lies in their generalization ability [81]. The application of this type of model appeared only in the early 1990s for the prediction of the concrete's compressive strength [82-84]. Other applications have been made regarding the durability of concrete. For instance, damage assessment of pre-stressed concrete beams by using natural frequency data [85], or the prediction of drying shrinkage of concrete, which is directly related to the apparition of new

cracks in the concrete [86]. However, a limited number of works have been published regarding ANN developments in the field of the non-destructive evaluation of reinforced concrete structures. For example, to interpret of GPR images of reinforced concrete to detect the presence, the size, and the depth of a reinforcing bar [87-88]. Also, for the extraction of dimensional information from steel reinforcing bars in concrete using images generated by an inductive sensor [89]. Besides, using impact-echo bispectra to detect and to classify the flaws in a concrete structure [90].

In order to estimate properties in the concrete by using NDT and ANN, even fewer works have been made. Viriyametanont [91], used two kinds of information from the GPR (direct air signal and the reflected steel signal information) to estimate the water content of concrete. For the first model (PCM1- direct air signal), the inputs were:

- Maximal amplitude of the direct air signal first positive pic.
- Maximal amplitude of the direct concrete signal first positive pic.
- Temporal position of the direct concrete signal first positive pic.
- Maximal amplitude of the direct concrete signal first negative pic.
- Temporal position of the direct concrete signal first negative pic.
- Maximal amplitude of the direct concrete signal first positive pic.
- Maximal amplitude of the direct concrete signal second positive pic.
- Temporal position of the direct concrete signal second positive pic.

Hence, for PCM1 he used 7 inputs, one hidden layer with 14 neurons and one output. On the contrary, for the second model (PCM2 - reflected steel signal), he used the same inputs as PCM1, 16 neurons and also, 1 output. Figures 2.20a and 2.20b show the results for the validation database for both models (PCM1 and PCM2). As it can be seen, for PCM1, the absolute error for 76% of the examples is less than 1%, while for PCM2, the absolute error for 83% of the examples is also less than 1%. This shows that both models can evaluate pertinently the water content.

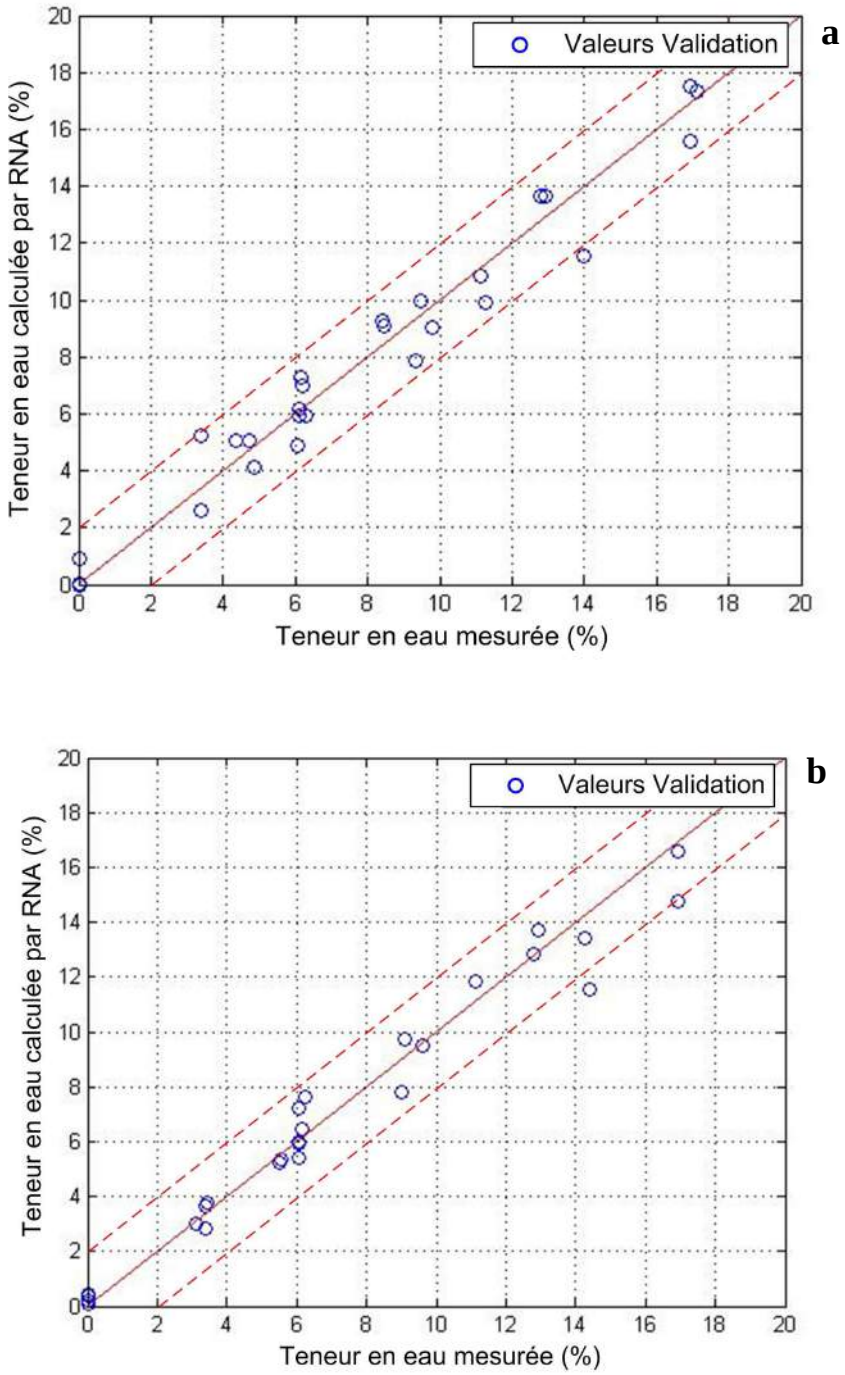

Figure 2-20. Results of the validation database for the chosen ANN water content models: a) PCM1 and b) PCM2**.**

Sbartaï [92], used a perceptron model with three inputs:

- Direct signal attenuation.
- Reflected signal attenuation.
- Temporal position of the reflected signal.

The objective was to estimate the concrete water content and the chloride content. For the water content a model (PCM1) with three inputs mentioned before, one hidden layer with 5 neurons and one output was used.

As for the chloride content, a model (PCM2) with four inputs, which are the three inputs mentioned before and the output of PCM1 (estimated water content) were used. Moreover, one hidden layer with 5 neurons and one output was also used. Figures 2.21a and b show the results for the test database for both models (PCM1 and PCM2). As it can be seen, for PCM1, the absolute error for 70% of the examples is less than 1%, while for PCM2, the absolute error for 90% of the examples is also less than 0.5 kg of Cl/m^3. This shows that not only PCM1 can evaluate pertinently the water content, but if we add the output of PCM1 as an input of PCM2, it is possible to evaluate an even more complex indicator as is the chloride content, in a pertinent way.

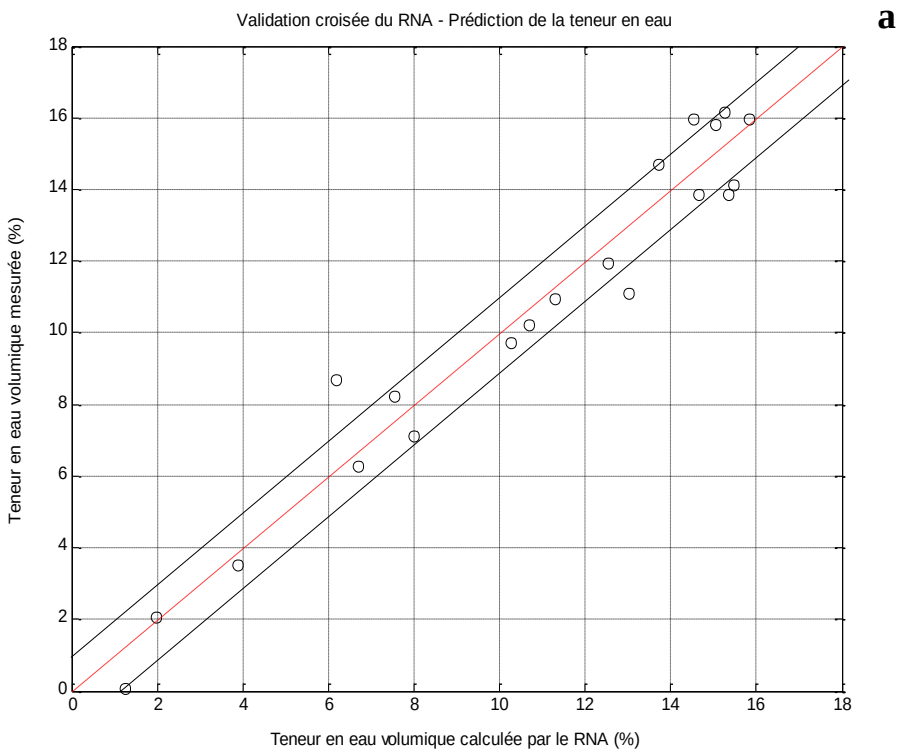

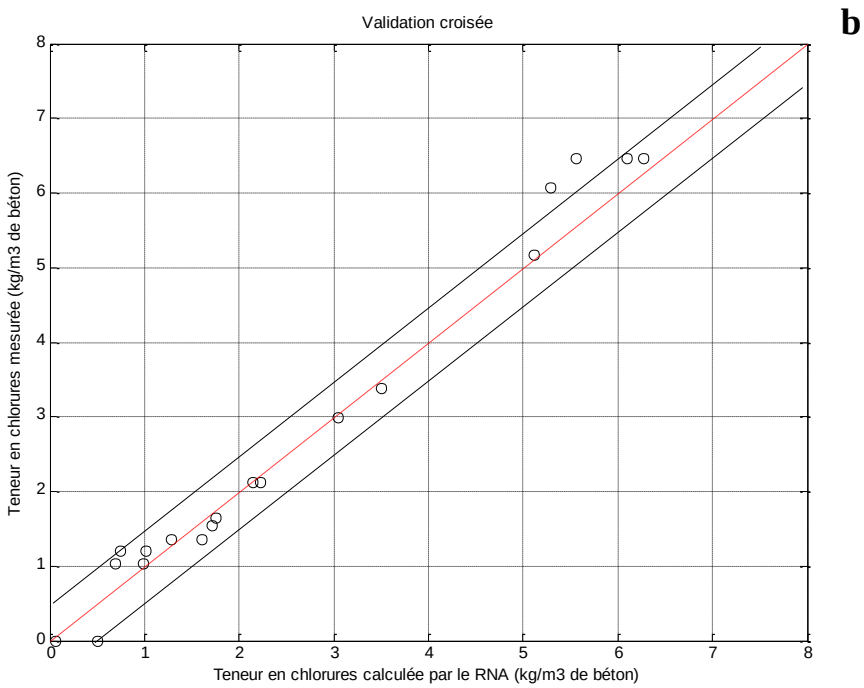

Figure 2-21. Results of the test database for the chosen ANN chloride content models: a) PCM1 and b) PCM2.

Finally, Sbartaï et al [63], made another study, which aims to evaluate the compressive strength and water content of a concrete by the combination of GPR, electrical resistivity and ultrasonic pulse velocity. In this study, the SENSO project database was used to train and test the ANN. A model with 10 inputs, one hidden layer with 16 neurons and 1 output were used to estimate the respective studied indicators. Figures 2.22a and b show the results for the test database for both indicators. The compressive strength is estimated with a mean absolute error of 5 MPa, and the water content is estimated with a mean absolute error of 0.9 %, which is very promising.

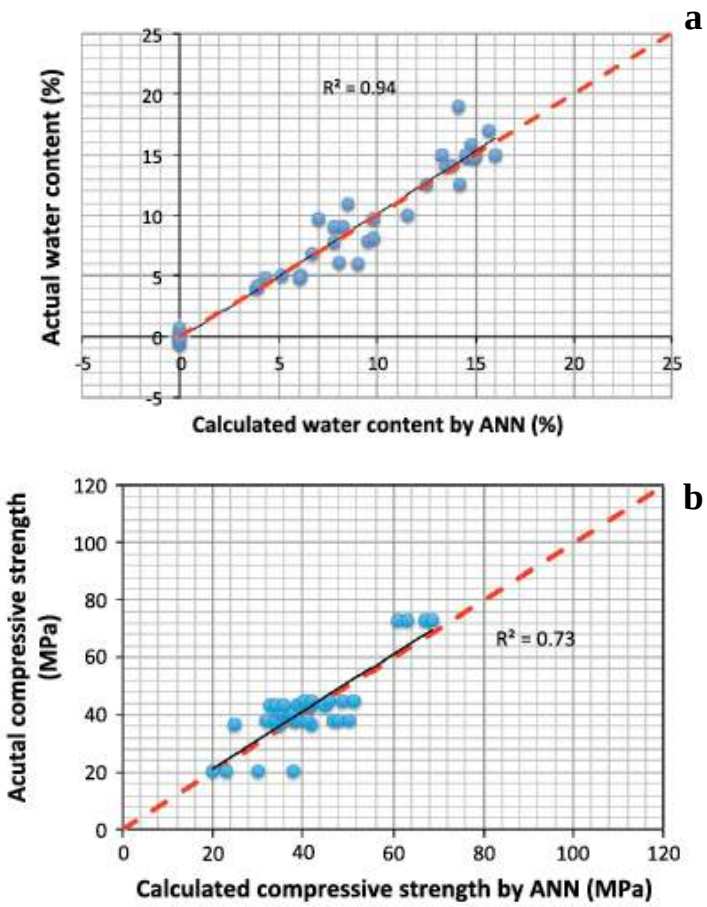

Figure 2-22. Results for the test database for water content ANN and compressive strength ANN.

2.5. Conclusions

The objective of this chapter was to establish a state of the art of different methodologies used throughout the years to evaluate an existing concrete structure from NDT measurements. It was described the use of different methods (destructive and non-destructive and the combination of both of them) to assess different indicators of the concrete (e.g. compressive strength, porosity, carbonation, etc.).

For destructive test, it was highlighted that an indicator on a studied concrete can be variable, and this variability can be intrinsic to the material or it can be due to other factors, like type of test, test's conditions, size of the sample, etc. The variability of concrete obtained by destructive tests was also discriminated in three groups: laboratory samples, in-site samples and on-site cores. Later, it was also emphasized that if different cores are extracted from different parts of a structure element, the evaluated indicator will not have the same values, introducing a new kind of variability, which is called spatial variability. A geostatistical tool called a variogram can model the spatial variability, and at the same time, the variogram can be used to make a spatial interpolation (kriging) to estimate unknown values in a studied area. It was also emphasized that

even if destructive tests are not fully adapted to evaluate an indicator on a structure element, they may be useful to posterior studies related to DT indicators uncertainty.

Later, the idea of using non-destructive tests to evaluate a concrete indicator was introduced, sustained by the fact that destructive test are expensive, time consuming and damaging to the structure. It was also highlighted that NDTs are variable themselves and that indicators can have combined effects on NDT measurements. Relationships between NDTs and indicators were presented to estimate the indicators, as well as the idea to use DTs for calibrating the results of the regression. As a simple regression is inadequate to evaluate an indicator of different concrete structures, the notion of NDT combination was presented. Three different commonly used methods were described: response surface, data fusion and artificial neural network. Their applications in different fields were described, as well as their successful incorporation into concrete structures evaluation.

References

[1] Breysse, D. “Non-Destructive Assessment of Concrete Structures: Reliability and Limits of Single and Combined Techniques”. Springer, RILEM, 2012, 374p.

[2] Ollivier, J.P., “Les résultats des essais croises Afrem pour la Détermination de la masse volumique apparente et de la porosité accessible à l’eau des bétons”, AFREM, 1998, 6p.

[3] Rougeau, P., “Les résultats d'essais Croises Afrem: Essai de carbonatation acceleré”, AFREM, 1998, 18p.

[4] Neville, A.M., “Propriétés des bétons”, Eyrolles, CRIB Sherbrooke-Laval, 1995, 806p.

[5] Project MAT1-CT94-0043, “Inter-laboratory comparison to support revision CEN/ISO standards called up in EN 206”, Concerte, 1997.

[6] Nikbin, I.M., Eslami, S.H., Rezvani, D. “An experimental comparative survey on the interpretation of concrete core strength results”, European journal of scientific research, Vol. 37, 2009, p. 445-456.

[7] Lydon F.D., Mahawish, A.H., “Strength and permeability results from a range of concretes”, Cement and Concrete Research, Vol. 19, 1989, p. 366-376.

[8] CEBTP Service Matériaux, “Essais d’intercomparaison 12ème campagne”, COFRAC, 2005.

[9] Aït-Mokhtar A., Belarbi R., Benboudjema F., Burlion N., Capra B., Poyet S. et al. “Experimental investigation of the variability of concrete durability properties”, Cement and Concrete Research, Vol. 45, 2013, p. 21–36.

[10] Pfister, V., Tundo, A., Luprano, V.A.M., "Evaluation of concrete strength by means of ultrasonic waves: A method for the selection of coring position", Construction and Building Materials, Vol. 61, 2014, p. 278-284.

[11] Pucinotti, R., "Assessment of in situ characteristic concrete strength", Construction and Building Materials, Vol.44, 2013, p. 63-73.

[12] Masi, A., Chiauzzi, L., "An experimental study on the within-member variability of in situ concrete strength in RC building structures", Construction and Building Materials, Vol.47, 2013, p. 951-961.

[13] Borosnyoi A., Szilagyi K. Studies on the spatial variability of rebound hammer test results recorded at in-situ testing. Építőanyag - Journal of Silicate Based and Composite Materials, vol. 65, 2013, pp. 102-106.

[14] Schoefs F, Tran TV, Bastidas-Arteaga E, Villain G, Derobert X, O'Connor AJ, Bonnet S. Optimization of non-destructive testing when assessing stationary stochastic processes: application to water and chloride content in concrete. Proceedings of the International Conference Durable Structures (ICDS12), Lisbon – Portugal, 31 May – 1 June 2012, p. 14.

[15] Stewart MG, Suo Q. Extent of spatially variable corrosion damage as an indicator of strength and time-dependent reliability of RC beams. Engineering Structures, Vol 31, 2009, pp. 198–207.

[16] Van Groeningen, J.W., Siderius, W., Stein, A., Constrained optimization of soil sampling for minimization of the kriging variance, Geoderma, vol. 87, 1998, pp. 239-259.

[17] Nguyen, N.T., "Évaluation non destructive des structures en béton armé: Étude de la variabilité spatiale et de la combinaison des techniques", Doctoral Thesis, Bordeaux University, 2014.

[18] Barnes, R., Variogram Tutorial, Global Software, Inc., p. 1-23.

[19] Clark, I., Practical Geostatistics, Geostokos Limited, 2001, p. 24-29.

[20] De Larrard, T., Benboudjema, F., Colliat, J.B., Torrenti, J.M., "Caractérisation expérimentale de la variabilité spatiale des propriétés d'un béton: Identification des longueurs de corrélation et recherche de corrélations entre indicateurs de durabilité". JFMS2012, Chambéry - France, 2012, 15p.

[21] O'Connor, A.J., Kenshel, O., "Experimental evaluation of the scale of fluctuation for spatial variability modeling of the chloride-induced reinforced concrete corrosion", Journal of Bridge Engineering, Vol. 18, 2013, p. 3-14.

[22] Bohling, G., Kriging, C&PE 940, 2005, p. 1-20.

[23] Newman, J., Seng Choo, B., "Testing an quality", Advanced Concrete Technology, 2003, 313p.

[24] Bungey, J.H., "Determining concrete strength by using small cores", Concrete Research, Vol. 31, 1979, p. 91-98.

[25] Bungey, J.H., Millard, S.G., "Testing of concrete structures", Chapman & Hall, Glasgow, 1996.

[26] Turatsinze, A., Castel, A., Bascoul, M., Mouret, M., "Comparaison entre la résistance des éprouvettes normalisées en béton et la résistance du béton in situ", Annales du Bâtiment et des Travaux Publics, 1999, p. 43-51.

[27] R.A.M, "A comparison between cube strength and in situ concrete strength developement". In Proceedings of the Institution of Civil Engineering Structures and Buildings, 1996, p. 138-153.

[28] Davis, A.G., "Nondestructive Test Methods for Evaluation of Concrete in Structures", ACI 228.2R-98, 1998, 62 p.

[29] International Atomic Energy Agency (IAEA), "Guidebook on non-destructive testing of concrete structures", Vienna, Austria, 2002, 242 p.

[30] Malhotra, V.M., Carino, N.J., "Handbook on Nondestructive Testing in Concrete", CRC Press, Boca Raton, FL, 2004, 384 p.

[31] Ferreira, R.M., Jalali, S., "NDT measurements for the prediction of 28-day compressive strength", NDT & E International, Vol. 43, 2010, p. 55-61.

[32] Colombo, M., Felicetti, R., "New NDT techniques for the assessment of fire-damaged concrete structures", Fire Safety Journal, Vol. 42, 2007, p. 461-472.

[33] Belagraa, L., Abdelaziz, M., Miloud, B., "Study of the Physico-Mechanical Properties of a Recycled Concrete Incorporating Admixtures by the Means of NDT Methods", Procedia Engineering, Vol. 108, 2015, p. 80-92.

[34] Pei, H., Li, Z., Zhang, J., Wang, O., “Performance investigations of reinforced magnesium phosphate concrete beams under accelerated corrosion conditions by multi techniques”, Construction and Building Materials, Vol. 93, 2015, p. 989-994.

[35] Krzemień, K., Hager, I., “Post-fire assessment of mechanical properties of concrete with the use of the impact-echo method”, Construction and Building Materials, Vol. 96, 2015, p. 155-163.

[36] Haach, V.G., Juliani, L.M., Da Roz, M.R., “Ultrasonic evaluation of mechanical properties of concretes produced with high early strength cement”, Construction and Building Materials, Vol. 96, 2015, p. 1-10.

[37] Angst, U.M., Polder, R., “Spatial variability of chloride in concrete within homogeneously exposed areas”, Cement and Concrete Research, Vol. 56, 2014, p. 40–51.

[38] Breysse, D., “Nondestructive evaluation of concrete strength: An historical review and a new perspective by combining NDT methods”, Construction and Building Materials, Vol. 33, 2012, p. 139-163.

[39] Balayssac J.P., Laurens S, Arliguie G, Breysse D, Garnier V, Dérobert X, Piwakowski B. Description of the general outlines of the French project SENSO – Quality assessment and limits of different NDT methods. Construction and Building Materials, Vol. 35, 2012, p. 131-138.

[40] Sbartaï, Z.M., Breysse, D., Larget, M., Balayssac, J.P., “Combining NDT techniques for improved evaluation of concrete properties”, Cement and Concrete Composites, Vol. 34, 2012, p. 725-733.

[41] Pollard, E., “Évaluation de situations dynamiques multicibles par fusion de données spatio-temporelles”. Doctoral Thesis, Grenoble University, 2010, 268 p.

[42] Breysse, D., Lataste, J.F., Balayssac, J.P., Garnier, V. “Quality and accuracy of concrete assessment provided by NDT measurement”, 6th International Probabilistic Workshop, Darmstadt, Germany, 2008, 15 p.

[43] Lataste, J.F., Breysse, D., “A Study on the variability of electrical resistivity of concrete”, Nondestructive Testing of Materials and Structures, RILEM Bookseries, 2013, p. 255-262.

[44] Box, G.E., Wilson, K.B., “On the Experimental Attainment of Optimum Conditions”, Journal of the Royal Statistical Society, Vol. 1, 1951, p. 1–45.

[45] Ratkoe, B.L., Hedayat, A., Federer, W.T., “Factorial Designs”, John Wiley & Sons, 1981.

[46] Khuri, A.I., Mukhopadhyay, S., “Response surface methodology”, John Wiley & Sons, Vol. 2, 2010, 22 p.

[47] Nam, Y.S., Jeong, Y.I, Shin, B.C., Byun, J.H., “Enhancing surface layer properties of an aircraft aluminum alloy by shot peening using response surface methodology”, Materials & Design, Vol. 83, 2015, p. 566-576.

[48] Adalarasan, R., Santhanakumar, M., Rajmohan, M., “Optimization of laser cutting parameters for Al6061/SiCp/Al2O3 composite using grey based response surface methodology (GRSM)”, Measurement, Vol. 73, 2015, p. 596-606.

[49] Shamekhi, E., Tannant, D.D., “Probabilistic assessment of rock slope stability using response surfaces determined from finite element models of geometric realizations”, Computers and Geotechnics, Vol. 69, 2015, p. 70-81.

[50] Zhang, J., Chen, H.Z., Huang, H.W., Luo, Z., “Efficient response surface method for practical geotechnical reliability analysis”, Computers and Geotechnics, Vol. 69, 2015, p. 496-505.

[51] Li, O., Cai, L., Fu, Y., Wang, Zou, H.Y., “Fracture properties and response surface methodology model of alkali-slag concrete under freeze–thaw cycles”, Construction and Building Materials, Vol. 93, 2015, p. 620-626.

[52] Şimşek, B., İç, Y.T., Şimşek, E.H., Güvenç, A.B., “Development of a graphical user interface for determining the optimal mixture parameters of normal weight concretes: A response surface methodology based quadratic programming approach”, Chemometrics and Intelligent Laboratory Systems, Vol. 136, 2014, p. 1-9.

[53] Cai, L., Wang, H., Fu, Y., “Freeze–thaw resistance of alkali–slag concrete based on response surface methodology”, Construction and Building Materials, Vol. 49, 2013, p. 70-76.

[54] Bektas, F., Bektas, B.A., “Analyzing mix parameters in ASR concrete using response surface methodology”, Construction and Building Materials, Vol. 66, 2014, p. 299-305.

[55] Cihan, M.T., Güner, A., Yüzer, N., “Response surfaces for compressive strength of concrete”, Construction and Building Materials, Vol. 40, 2013, p. 763-774.

[56] Mohammed, B.S., Fang, O.C., Hossain, K.M., Lachemi, M., "Mix proportioning of concrete containing paper mill residuals using response surface methodology", Construction and Building Materials, Vol. 35, 2012, p. 63-68.

[57] Aldahdooh, M.A., Bunnori, N.M., Johari, M.A., "Evaluation of ultra-high-performance-fiber reinforced concrete binder content using the response surface method", Materials & Design, Vol. 52, 2013, p. 957-965.

[58] Cho, T., "Prediction of cyclic freeze–thaw damage in concrete structures based on response surface method", Construction and Building Materials, Vol. 21, 2007, p. 2031-2040.

[59] Güneyisi, E., Gesoğlu, M., Algın, Z., Mermerdaş, K., "Optimization of concrete mixture with hybrid blends of metakaolin and fly ash using response surface method", Composites Part B: Engineering, Vol. 60, 2014, p. 707-715.

[60] Nambiar, E.K., Ramamurthy, K., "Models relating mixture composition to the density and strength of foam concrete using response surface methodology", Cement and Concrete Composites, Vol. 28, 2006, p. 752-760.

[61] Buratti, N., Ferracuti, B., Savoia, M., "Response Surface with random factors for seismic fragility of reinforced concrete frames", Structural Safety, Vol. 32, 2010, p. 42-51.

[62] Bayramov, F., Taşdemir, C., Taşdemir, M.A., "Optimisation of steel fibre reinforced concretes by means of statistical response surface method", Cement and Concrete Composites, Vol. 26, 2004, p. 665-675.

[63] Sbartaï, Z.M., Laurens, S., Elachachi, S.M., Payan, C., "Concrete properties evaluation by statistical fusion of NDT techniques", Construction and Building Materials, Vol. 37, 2012, p. 943-950.

[64] Castañedo, F., "A review of data fusion techniques", The Scientific World Journal, 2013, 19 p.

[65] Bloch, I., "Information combination operators for data fusion: A comparative review with classification", IEEE, Vol. 26, 1996, p. 52-67.

[66] Dupuis O., "Fusion entre les données ultrasonores et les images de radioscopie à haute résolution: application au contrôle de cordon de soudure", Doctoral thesis, Lyon INSA, 2000.

[67] Dubois, D., Prade, H., "Théorie des possibilités: application à la représentation des connaissances en informatique", Doctoral thesis, Masson, Paris, 1988.

[68] Martin, A., "La fusion d'informations, Polycopié de cours ENSIETA", 2005.

[69] Bloch, I., Maitre, H., "Fusion de données en traitement d'images: modèles d'information et decisions", Traitement du Signal, Vol. 11, 1994.

[70] Koller J., Ulmke M., "Data Fusion for Ground Moving Target Tracking", IEEE International Conference on Multisensor Fusion and Integration for Intelligent Systems, 2006, p. 217–224.

[71] Valet L., Mauris G., Bolon P., "A Statistical Overview of Recent Literature in Information Fusion", In proceedings of the 3rd International Conference On Information Fusion, Paris, 2000, p. MoC3-22.

[72] Georgel, B., Lavayssière, B., "Fusion de données: un nouveau concept en CND", In Procedings of the 6th European Conference on NDT, Vol. 1, 1994, p. 31–5.

[73] Gros, X.E., Strachan, P., Lowden, D.W., Edwards, I., "NDT data fusion", In Procedings of the 6th European conference on NDT, Vol. 1, 1994, p. 355–359.

[74] Tacnet, J.M., Richard, D., Dezert, J., Batton-Hubert, M., "Aide à la décision et fusion d'information pour l'expertise des risques naturels: Analyse de l'efficacité des ouvrages de protection", JFMS, Toulouse, 2010.

[75] Gros, X.E., Bousigue, J., Takahashi, K., "NDT data fusion at pixel level", NDT&E International, Vol. 32, 1999, p. 283–292.

[76] Kohl, C., Streicher, D., "Results of reconstructed and fused NDT-data measured in the laboratory and on-site at bridges", Cement & Concrete Composites, Vol. 28, 2006, p. 402–413.

[77] Völker, C., Shokouhi, P., "Multi sensor data fusion approach for automatic honey comb detection in concrete", NDT&E International, Vol. 71, 2015, p. 54–60.

[78] Villain, G., Sbartaï, Z.M., Dérobert, X., Garnier, V., Balayssac, J.P., "Durability diagnosis of a concrete structure in a tidal zone by combining NDT methods: Laboratory tests and case study", Construction and Building Materials, Vol. 37, 2012, p. 893-903.

[79] Ploix, M.A., Garnier, V., Breysse, D., Moysan, J., "NDE data fusion to improve the evaluation of concrete structures", NDT&E International, Vol. 44, 2011, p. 442–448.

[80] Martini, D., Garnier, V., Ploix, M.A., “Evaluation of an intrinsic error estimator for the data fusion of NDT techniques used to identify the material and damage properties of concrete structures”, 6th workshop on structural health monitoring, Dresden, 2012.

[81] Dreyfus G., Samuelides M., Martinez J.M., Gordon M.B., Badran F., Thiria S., Hérault L., “Réseaux de neurones: Méthodologie et applications”, Eyrolles, 2nd ed., 2004, 386p.

[82] Yeh, I.C., “Modeling of strength of high-performance concrete under normal outdoor exposure”, RILEM Seminar on durability, Hanover, 1984.

[83] Dias, W.P., Pooliyadda, S.P., “Neural networks for predicting properties of concretes with admixtures”, Construction and building materials, Vol. 15, 2001, p. 371-379.

[84] Trocoli, A., Dantas, A., Batista, M. De Jesus Nagahama, L.K., “Prediction of compressive strength of concrete containing construction and demolition waste using artificial neural networks”, Construction and Building Materials, Vol. 38, 2013, p. 717-722.

[85] Atici, U., “Prediction of the strength of mineral admixture concrete using multivariable regression analysis and an artificial neural network”, Expert Systems with Applications, Vol. 38, 2011, p. 9609-9618.

[86] Bal, L., Buyle-Bodin, F., “Artificial neural network for predicting drying shrinkage of concrete”, Construction and Building Materials, Vol. 38, 2013, p. 248-254.

[87] Shaw, M.R., Millard, S.G., Molyneaux, T.C., Taylor, M.J., Bungey, J.H., “Location of steel reinforcement in concrete using ground penetrating radar and neural networks”, NDT & E International, Vol. 38, 2005, p. 203-212.

[88] Molyneaux, T.C., Millard, S.G., Bungey, J.H., Zhou, J.Q., “Radar assessment of structural concrete using neural networks”, NDT & E International, Vol. 28, 1995, p. 281-288.

[89] Zaid, M., Gaydecki, P., Quek, S., Miller, G., Fernandes, B., “Extracting dimensional information from steel reinforcing bars in concrete using neural networks trained on data from an inductive sensor”, NDT & E International, Vol. 37, 2004, p. 551-558.

[90] Xiang, Y., Tso, S.K., “Detection and classification of flaws in concrete structure using bispectra and neural networks”, NDT & E International, Vol. 35, 2002, p. 19-27.

[91] Viriyametanont, K., “Reconnaissance physique et géométrique d’éléments en béton armé par radar et réseaux de neurones artificiels”, Doctoral thesis, Toulouse university, 2008.

[92] Sbartaï, Z.M., “Caractérisation physique des bétons par radar approche neuromimetique de l’inversion”, Doctoral thesis, Toulouse and Sherbrooke universities, 2005.

CHAPTER 3
OPTIMAL SPATIAL SAMPLING METHOD (OSSM)

3.1. Introduction

NDT methods are sensitive not only to anomalies in the concrete but also to its physical and mechanical properties variation. For instance, ultrasound, impact-echo and rebound hammer are used to assess the concrete compressive strength, while electrical resistivity and GPR are sensitive to water content. Moreover, concrete inhomogeneity often leads to spatial variability in structures [1-4]. In addition, recent reliability studies have shown that the spatial correlation may govern the reliability of structural components [5]. Some studies have been carried out with the aim of analyzing spatial variability but, none of them has focused on sampling optimization for optimal inspection.

Among NDT methods, some, such as ultrasonic pulse velocity, rebound hammer, GPR, etc. are fast and inexpensive. The general frame that is promoted is that of a two-step approach where a fast technique is first used to obtain a general view of the spatial distribution for a particular property of the concrete (strength, moisture, etc.), and where the critical zones can be analyzed more into details in a second step, with NDT measurements of higher quality and/or cores. This approach takes advantage of the two types of ND investigations (fast and slow) and destructive testing while keeping the cost/benefit ratio within reasonable limits.

Nonetheless, to maximize the contribution of NDT methods or coring procedure in a previously investigated structure, it is imperative to carry out optimal spatial sampling for localizing the most critical zones in order to optimize the diagnosis.

This chapter presents a new idea for the diagnosis of reinforced concrete structures based on an original methodology of NDT spatial sampling optimization, making use of geostatistical tools such as the variogram, described in the previous chapter, and kriging, described in the next section. An algorithm inspired on the Spatial Simulated Annealing (SSA) [6], which is used for geostatistical applications [7] was developed in order to attain a NDT spatial sampling optimization. SSA has been used for instance in other fields such as measuring radioactivity releases [8], and ecosystem studies [9]. However, this algorithm has never been used on concrete structures studies.

This approach offers a new solution for a very important problem in concrete structure evaluation and can be applied to any NDT technique and to a large variety of concrete structures as bridges, buildings, tunnels, nuclear plants, etc. An original Optimization Spatial Sampling Method (OSSM) was developed and tested with three different fitness functions: the mean kriging standard deviation, the mean prediction error and the variance estimation error [10]. The performance of the OSSM was explored a) with simulated 2D data inferred from a specified spatial correlation (variogram) and b) with two different observables: ultrasonic pulse velocity measurements

obtained on a horizontal profile (1D case) and capacity of large electrodes – Permittivity measurements obtained on two horizontal profiles (2D case) of a wall of a thermal power plant located in Le-Havre, France.

3.2. Spatial interpolation: Kriging

Kriging is a widely used method for spatial interpolation [11] that can predict an unobserved measurement (Z_v*) using the weights of the surrounding observed measurements (Z_i) according to the following equation:

$$Z_v^* = \sum_{i=1}^{N} \lambda_i \, Z_i, \tag{3.1}$$

where λ_i is the weight of the i^{th} observation. The method is based on the minimization of the variance of the interpolation error (e) (equation 3.2) of the estimated value (equation 3.3).

$$e = Z_i - Z_v{}^* \tag{3.2}$$

$$\sigma_e^2 = Var(Z) + \sum_{i=1}^{N} \sum_{j=1}^{N} \lambda_i \lambda_j \, Cov\left(Z_i \, , Z_j\right) - 2 \sum_{i=1}^{N} \lambda_i \, Cov(Z_v{}^*, Z_i) \tag{3.3}$$

The minimization is obtained by doing the derivation of σ_e^2 and equaling to zero. After doing this procedure, the equation obtained is:

$$\sum_{j=1}^{N} \lambda_j \, Cov\left(Z_i \, , Z_j\right) = Cov(Z_v{}^*, Z_i) \qquad \forall i = 1 \dots N. \tag{3.4}$$

In matrix form the equation obtained is:

$$K_s \lambda_s = k_s, \tag{3.5}$$

Where K_s is the Covariance matrix of the known values; k_s is the covariance vector of each known value Z_v* and λ_s is the weight vector of each known value. The objective of this minimization is to obtain the weights λ_i associated to each of the rounding points of the unobserved measurement (Z_v*).

In the case of the ordinary kriging, which statement is that the mean is unknown, there is a constrained minimization problem. Therefore, it is convenient to use the Lagrange method to solve it. The Lagrange method consists on adding the Lagrange multiplier (μ) to σ_e^2 (equation. 3.6) to assure the inverse of the matrix K_s.

$$L(\lambda, \mu) = \sigma_e^2 + 2\mu\left(\sum_{i=1}^{N} \lambda_i - 1\right) \tag{3.6}$$

After doing the minimization, the equation obtained is:

$$\sum_{j=1}^{N} \lambda_j \, Cov\left(Z_i \, , Z_j\right) + \mu = Cov(Z_v{}^*, Z_i) \qquad \forall i = 1 \dots N \qquad \sum_{j=1}^{N} \lambda_j \, . \tag{3.7}$$

After obtaining the weights λ_i, the variance of interpolation error of the estimated value in the ordinary kriging (σ_k^2) is:

$$\sigma_k^2 = Var\,(Z) - \sum_{i=1}^{N} \lambda_i\, Cov\,(Z_v^*, Z_i) - \mu. \tag{3.8}$$

This variance can be seen as the uncertainty of the estimated value Z_v*. This uncertainty becomes more important as the distance between the observed and the estimated value increases. On figure 3.1, case of one dimension, synthetic simulation is implemented supposed a spherical variogram, with a sill equal to 1, nugget equal to 0 and range equal to 2 m. It can be seen for a different number of observed points (N) that the σ_k^2 increases with the increment of the distance between the estimated and known value and that σ_k^2 reach a maximum when the estimated value is right in the middle of two known measurements. It can also be seen that σ_k^2 increases with the decrease of N and in the case of 2 measured points, σ_k^2 reach a maximum when the distance between the estimated and known value is the same as the range. Therefore, it can be inferred that when the σ_k^2 achieves its maximum, the data are no longer correlated, hence, the estimated values with a distance from the observed points more important than the correlation length, will have the same value and the same σ_k^2.

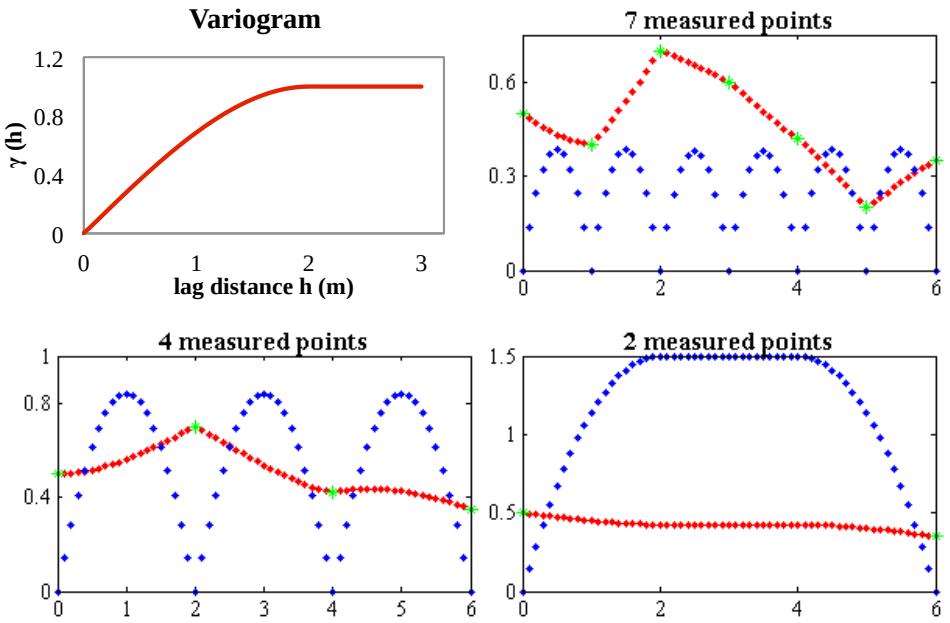

Figure 3-1. Case one dimension. Effect of sampling on $\boldsymbol{\sigma_k^2}$ for a spherical variogram with nugget of 0, sill of 1 and range of 2 m. Known values (green points), estimated values (red points) and kriging variance for each estimated point (blue points).

In figure 3.2a and b, three simulations were implemented with the same variogram model, the same sill and nugget but different ranges (correlation lengths) 1m, 2.5m and 5m. The simulated variograms can be seen in figure 3.2a. Figure 3.2b presents the relationship between the Kriging variance and the number of points. From this figure, it can be seen that the necessary sampling

points (N) is less with the variogram of range equal to 2.5 m, than that for the variogram of range equal to 1m to obtain the same σ_k^2.

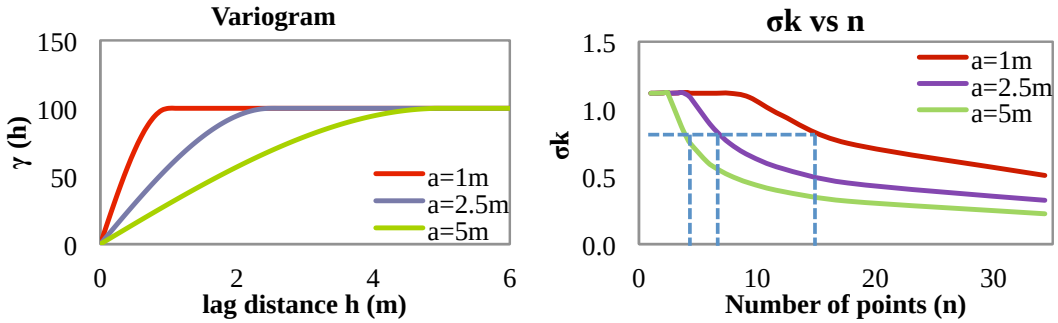

Figure 3-2. Effect of the range/correlation length on the $\boldsymbol{\sigma_k^2}$ and the sampling with three variograms with the same model, nugget and sill, but with ranges of 1 m, 2.5 m and 5 m respectively.

From the presented simulation, it can be inferred that Kriging is an interesting tool for a sampling strategy implementation. The correlation length of the distributed points is significantly dependent of the number of point's measurements. This means that the correlation length play an important role (Kriging interpolation, sampling evaluation) and should be evaluated on site. The next section will focus on the use of the variogram and Kriging tools for implementing spatial optimization sampling strategy.

3.3. Presentation of the strategy

For the structure manager, it is important to regularly assess the condition of the structure to know when he must proceed to some maintenance or reparations. Visual inspection is not enough or might be inadequate, while several NDT measurements are time consuming and expensive. Taking cores throughout the structure is not just expensive, but it would also affect structural stability and safety. In addition, the results provided by NDT remain local information and cannot be generalized to the whole structure. Hence, a good compromise between different inspection strategies would be required to classify and evaluate accurately the maintenance and/or repair zones in the structure, accounting for both time and cost efficiency.

To define an appropriate maintenance/reparation strategy at a minimum cost, it is necessary to implement an optimal inspection strategy (OIS). This strategy consists of carrying out first a pre-auscultation of the structure under test, using a "fast" and low cost NDT to evaluate and model the spatial variability. In a second step, the Optimization Spatial Sampling Method (OSSM) developed for this study will make possible to define the number and the optimal locations of more refined measurements or of samples to be taken for complementary diagnosis or future monitoring of the concrete structure.

The OSSM, which will be fundamental to the planning of an OIS, uses the spatial correlation and variability of NDT to evaluate the mechanical properties of a concrete structure in the best way possible, using a combination of fast and low cost NDT, higher quality NDT, and eventually coring in order to reach a relevant diagnosis of the actual condition of the concrete structure at an acceptable cost/benefit ratio (Figure 3.3).

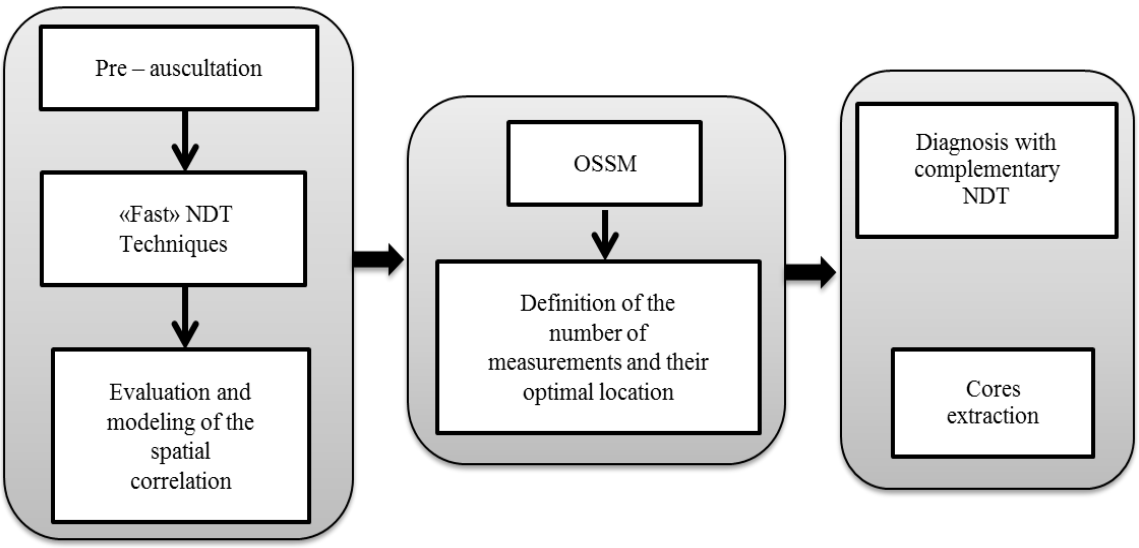

Figure 3-3. Optimal inspection strategy.

3.4. Optimization algorithm

3.4.1. Principle of the method

The optimization algorithm has the aim to optimize the first sampling of pre-auscultation using fast NDT methods and to find the best locations with less number of sampling. An example of the method is presented on figure 3.4. To find the best locations, a fitness functions are minimized using a specific algorithm. This specific algorithm is inspired by Spatial Simulated Annealing (SSA), which was adopted for our case study.

The Optimization Spatial Sampling Method (OSSM) starts with an initial set "s_o" of n values distributed on a regular grid in a space S of N measurements organized in a regular grid "SO". This set is progressively modified by relocating one value of s_o to a random available location in SO. When the new configuration, s_1, is established, the fitness function is evaluated. This configuration will be accepted with a probability of acceptance P calculated with the step function described in (equation 3.9):

$$\Delta = J_o - J_1$$
$$P = 0 \qquad If\ \Delta \leq 0, \tag{3.9}$$
$$P = 1 \qquad If\ \Delta > 0,$$

where J_o is the fitness function value for s_o and J_1 is the fitness function value for s_1. Figure 3.4 shows the illustration of this method for one step.

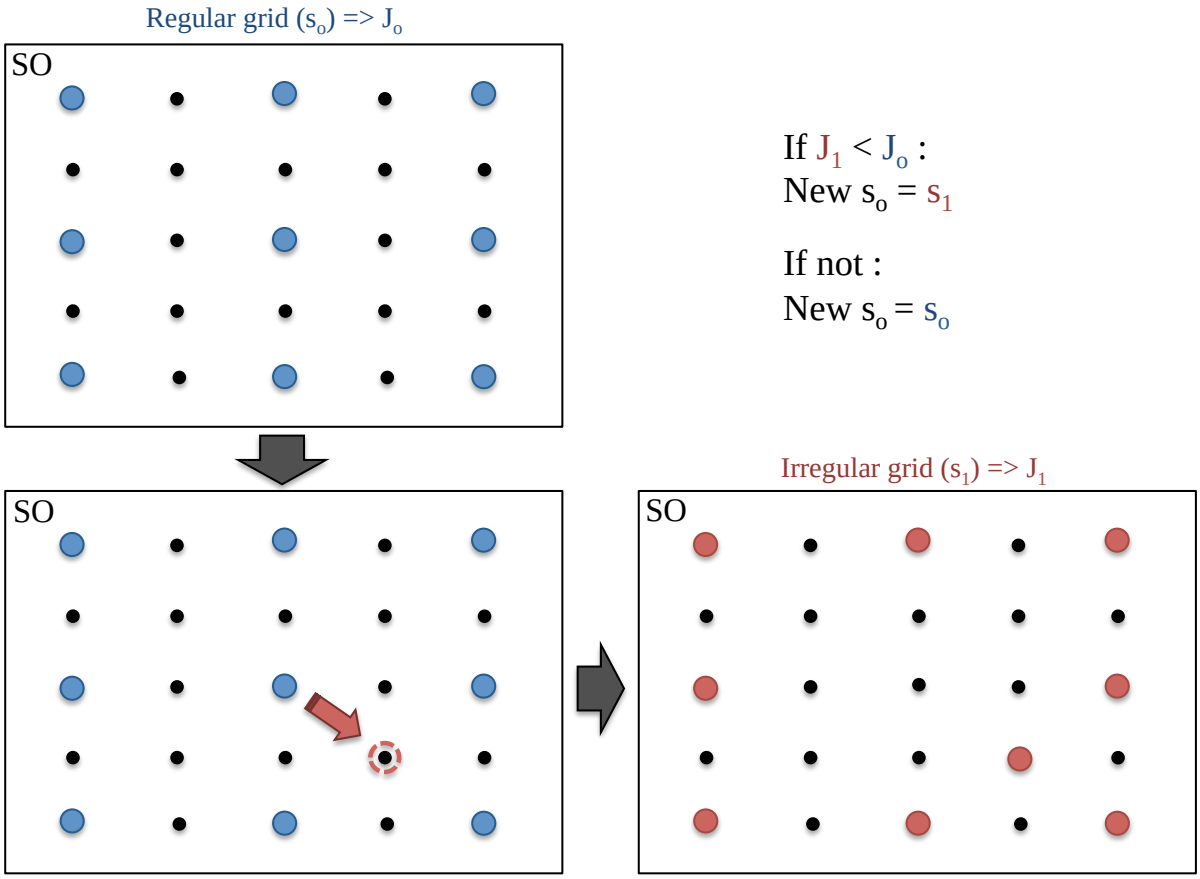

Figure 3-4. One step's illustration of the OSSM.

Three fitness functions were tested for the optimization algorithm. They are defined below.

3.4.2. Fitness functions definition

3.4.2.1. Mean kriging estimation error standard deviation (MKSD)

At each iteration "i" of the algorithm, ordinary kriging is used for estimating J_1. This spatial interpolation method not only estimates unobserved measurements but also predicts the kriging variance for each estimated value. Hence, the first fitness function used is the mean of the square of the kriging variance calculated for all the estimated points, and normalized with respect to the mean value of the N original points (Mean_R).

$$MKSD = \frac{\sigma_k^2}{Mean\_R} \ (\%) \tag{3.10}$$

This function represents the uncertainty that exists when one tries to represent the original measured field with a smaller number of measurements, n (n<N). Moreover, this fitness function that is used in SSA and other geostatistical applications has the advantage that s_1 is not limited to

the available locations of SO, but the moved value of s1 can be place anywhere in S. Hence, MKSD is a flexible fitness function that can cover all the space S without the necessity of extra measurements.

3.4.2.2. *Mean prediction error (MPE)*

This function is the mean of the prediction error, which is the absolute difference between the measured (Z) and the estimated (Z*) values calculated across all the points n, and normalized with respect to the average of the N original points (Mean_R).

$$MPE = \frac{|Z - Z^*|}{Mean\_R} \ (\%) \tag{3.11}$$

This function represents the error that is committed when attempting to represent the original measured field with a smaller number of measurements n.

3.4.2.3. Variance estimation error (VEE)

This function represents the error in the calculation of the global variance with a smaller number of known measurements (n). Zero error means that the global variance calculated with n is the same as the global variance calculated with the N original measurements. Thus, the VEE is evaluated as one minus the ratio between the variance of n known measurements (V_i) and the variance of the N original measurements (V_N):

$$VEE = 1 - \frac{V_i}{V_N} \ (\%) \tag{3.12}$$

Unlike MKSD, to be able to use MPE and VEE as fitness functions, the moved value of the new configuration s_1 must be placed in an available location of the SO grid.

The algorithm developed in this work differs from the original SSA for a few reasons: (i) while the SSA works in a continuous domain, the original domain is discretized on the grid S; (ii) rather than the Metropolis Accepting Criterion (MAC) [6], it uses a step function criterion, which was found to give better results than MAC since the resulting fitness function values after the optimization were smaller and the optimization process ran faster; (iii) there is no need to use a cooling factor (as in SSA) [6] because the new location of the moving point is chosen randomly among the candidate locations in S.

3.5. Validation of the algorithm

The potential of the OSSM with each of the three fitness functions (MKSD, MPE, VEE) has been tested first on a synthetic case, then on a real case study.

3.5.1. Validation of the OSSM on simulated data

3.5.1.1. Performance of OSSM fitness functions

The potential of the OSSM proposed above with each of the three fitness functions (MKSD, MPE, VEE) was explored first in a synthetic field of 9 m x 9 m, with 49 known values regularly separated by a distance of 1.5 m, that was simulated using a Fourier Integral Method [12] (Figure 3.5a). This field was generated using a spherical variogram, with a nugget equal to 0, a sill equal to 4.56 and a range of 2.6 m (Figure 3.5b). To simplify, the simulated variogram was omnidirectional, which implies that the material structuration of the variability is the same in all directions of the simulated area. This is a limit of the simulation, because in some cases, some heterogeneity in a particular direction due for instance to the casting process is possible which can modify the variogram. It was an unconditional simulation with a mean of 9.94 and a variance of 4.13.

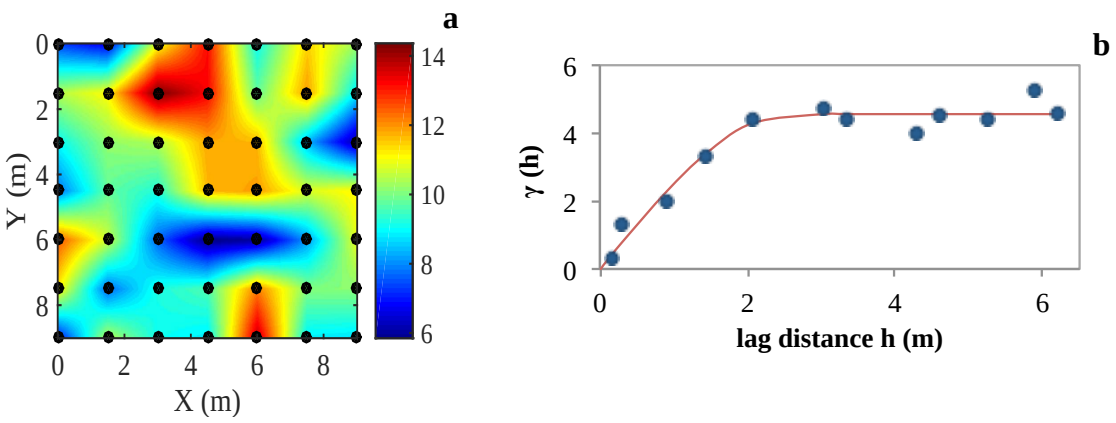

Figure 3-5. a) Simulated field, b) Variogram used to simulate the synthetic field.

After the simulation of a 2D surface that represents a concrete slab, the three fitness functions are evaluated with a number of measurements decreasing from 49 to 3. For each number of points the locations of the points are in regular configuration. The fitness functions are then calculated for each case representing a number of points “n”. Figures 3.6a and 3.6b show the relationship between each fitness function and the number, n, of known values in the case of a regular grid. As expected, all the fitness function values (FFV) decrease as n increases. It can also be seen that VEE is a little more sensitive to n than MPE and MKSD. The contrast between the minimum and maximum number of points is about 75% for VEE and about 73% for MPE and MKSD.

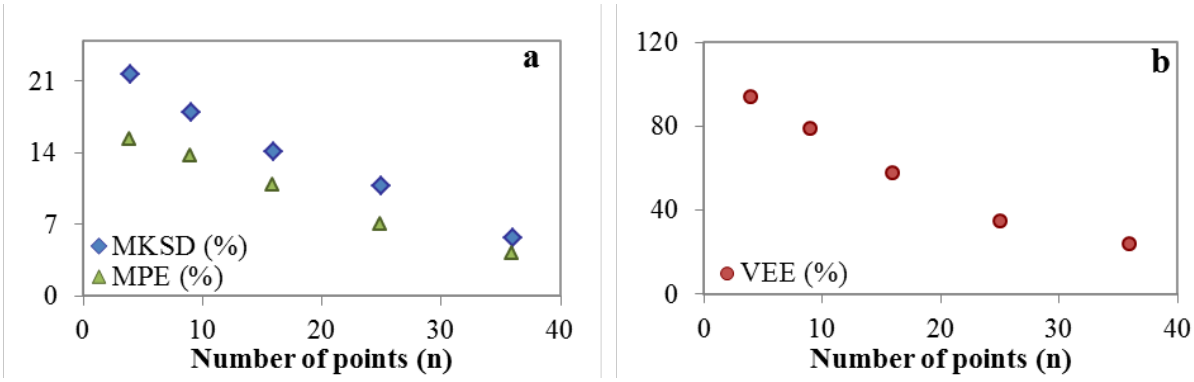

Figure 3-6. Relationship between each fitness function (MKSD, MPE and VEE) and the number of known values (n) in the case of a regular grid.

With a fixed number "n" of known values, the OSSM is used later to minimize the FFV just by relocating the n values on the grid, passing from a regular grid to an irregular one. For a clearer view of the impact of the OSSM, as an example, let us assume that 16 NDT measurements are to be made on the field considered. The first step for the optimization consists in obtaining a kriging map for a regular grid with the 16 NDT measurements (figure 3.8b). The fitness function initial values (FFV_o) are shown in table 3.1. Starting from the initial values of fitness functions obtained with the regular grid, the OSSM is applied for 4000 iterations to obtain the final fitness function values (FFV_f) shown in table 3.1.

The results of the optimization shows that, in the case of optimization with MKSD as the fitness function, the FFV only decreased by 0.39% from a regular grid to an optimal irregular grid. In fact, the value of MKSD did not decrease even if the number of iterations was increased (figure 3.9c). Additionally, the kriging map obtained with this fitness function (figure 3.8c) is not a good representation of the original field. The variance obtained at the end of the optimization is not only significantly smaller than the real variance but is also lower than the variance obtained with a regular grid, moving farther from the real global variance value. Several optimizations were carried out on different sets of simulated data using this fitness function and poor performance of the algorithm was always observed, even for different n known points as it can be seen in figures 3.7a-c.

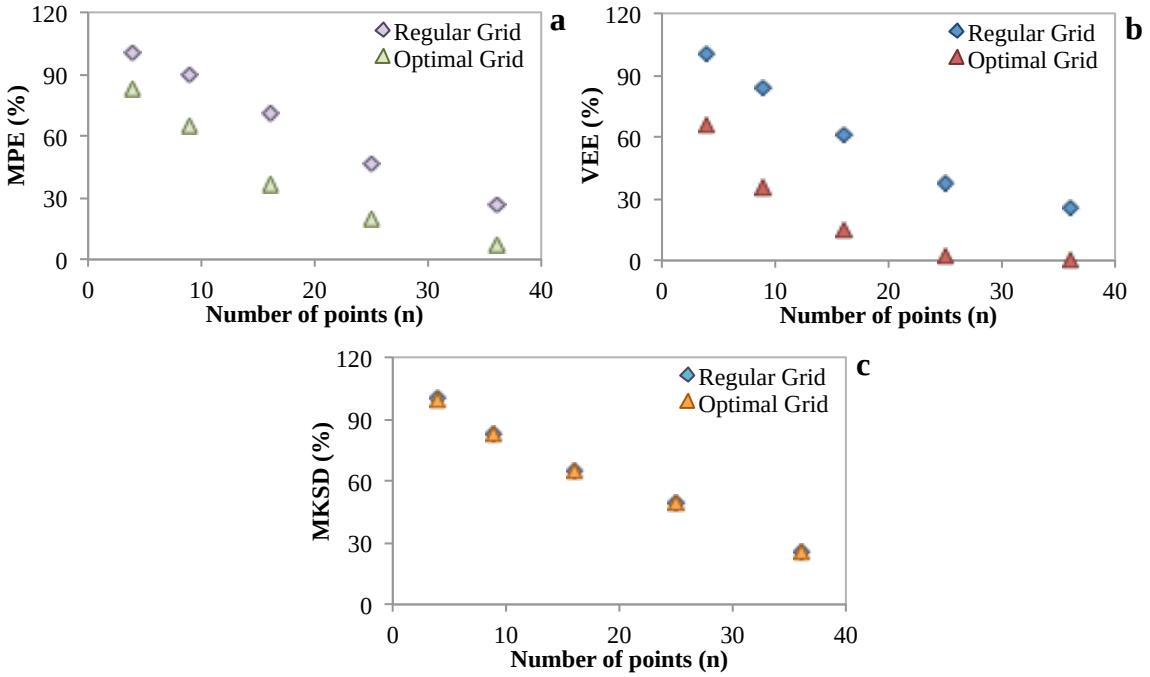

Figure 3-7. Relationship between each fitness function and the number of known values (n) in the case of a regular grid. a) MPE, b) VEE and c) MKSD.

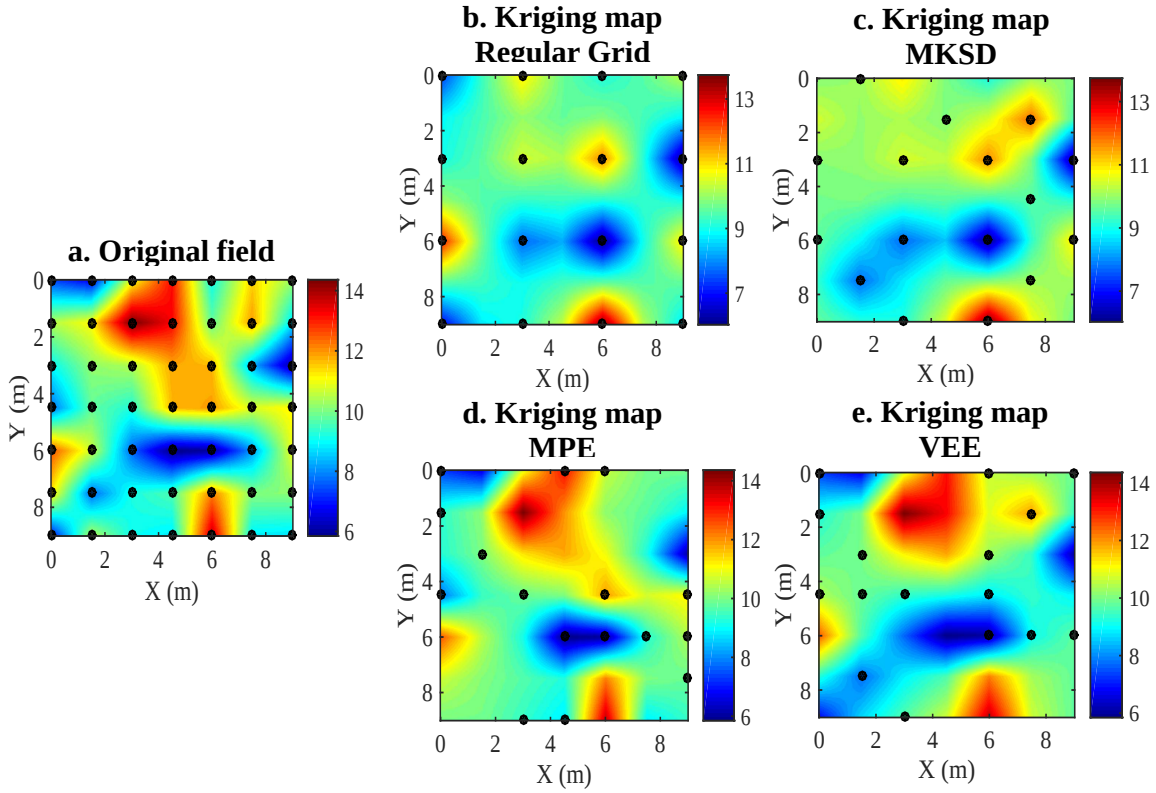

Figure 3-8. (a) Simulated field. (b) Kriging map obtained with a regular grid of 3m x 3m and 16 known values and Kriging maps obtained after the OSSM with each fitness function. (c) MKSD. (d) MPE. (e) VEE.

Table 3-1. Initial fitness function values (FFVo) for a regular grid composed of 16 known value and final fitness function values (FFV_1) for an irregular grid composed of 16 known values after 4000 iterations of OSSM.

	Original Statistical Values	REGULAR GRID			OPTIMIZED REGULAR GRID		
		MKSD	MPE	VEE	MKSD	MPE	VEE
FFV (%)	-	14.06	10.84	57.76	14	5.54	13.72
Mean	9.94	9.42			9.7	9.97	9.82
Variance	4.13	1.74			1.51	3.15	3.56

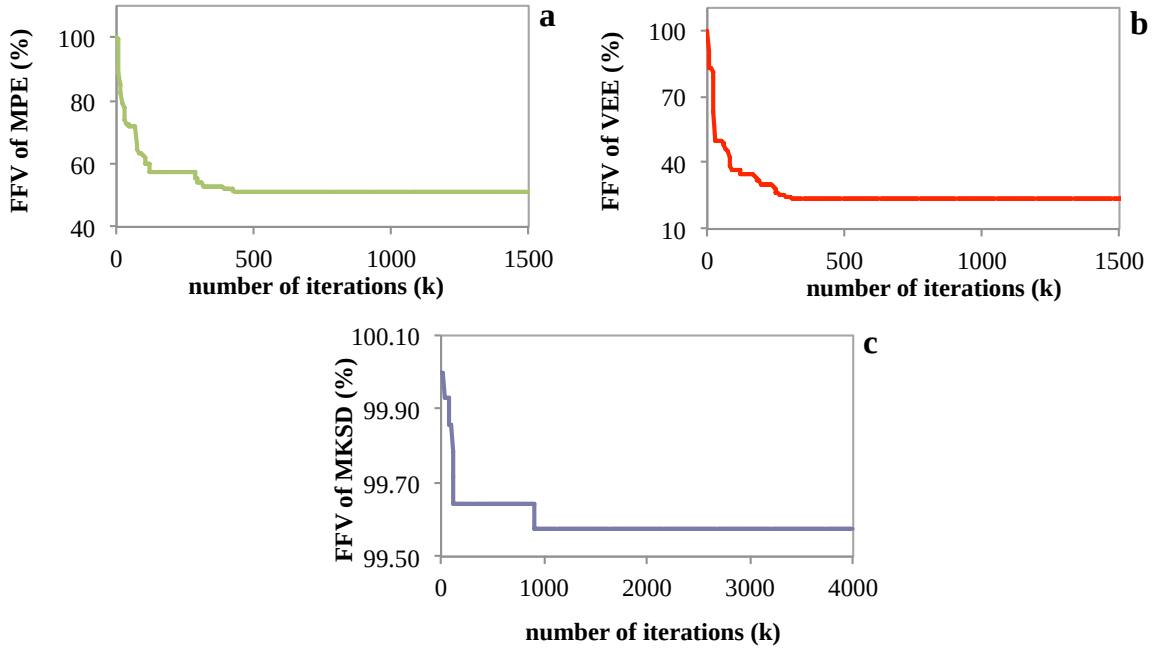

Figure 3-9. Evolution of the fitness functions with the number of iterations. (a) MPE. (b) VEE. (c) MKSD.

In the case of the optimization with MPE as the fitness function, the FFV of MPE decreases by 49% from a regular grid to an optimal irregular grid. Moreover, figure 3.8d shows that the kriging map obtained is close to the original field. This fitness function seems to give more importance to the zones where the variability is stronger. Finally, in the case of the optimization with the VEE as the fitness function, the value of VEE is reduced by 76% by passing from a regular grid to an irregular one, and the kriging map obtained (figure 3.8e) is in good agreement with the original field.

In figure 3.10, it can be seen the illustration of OSSM comparing the regular grid and the optimized irregular grid for 36, 25, 16, 9 and 4 number of points (n) and MPE and VEE as the fitness functions. As MKSD was proven to be ineffective, it was not illustrated.

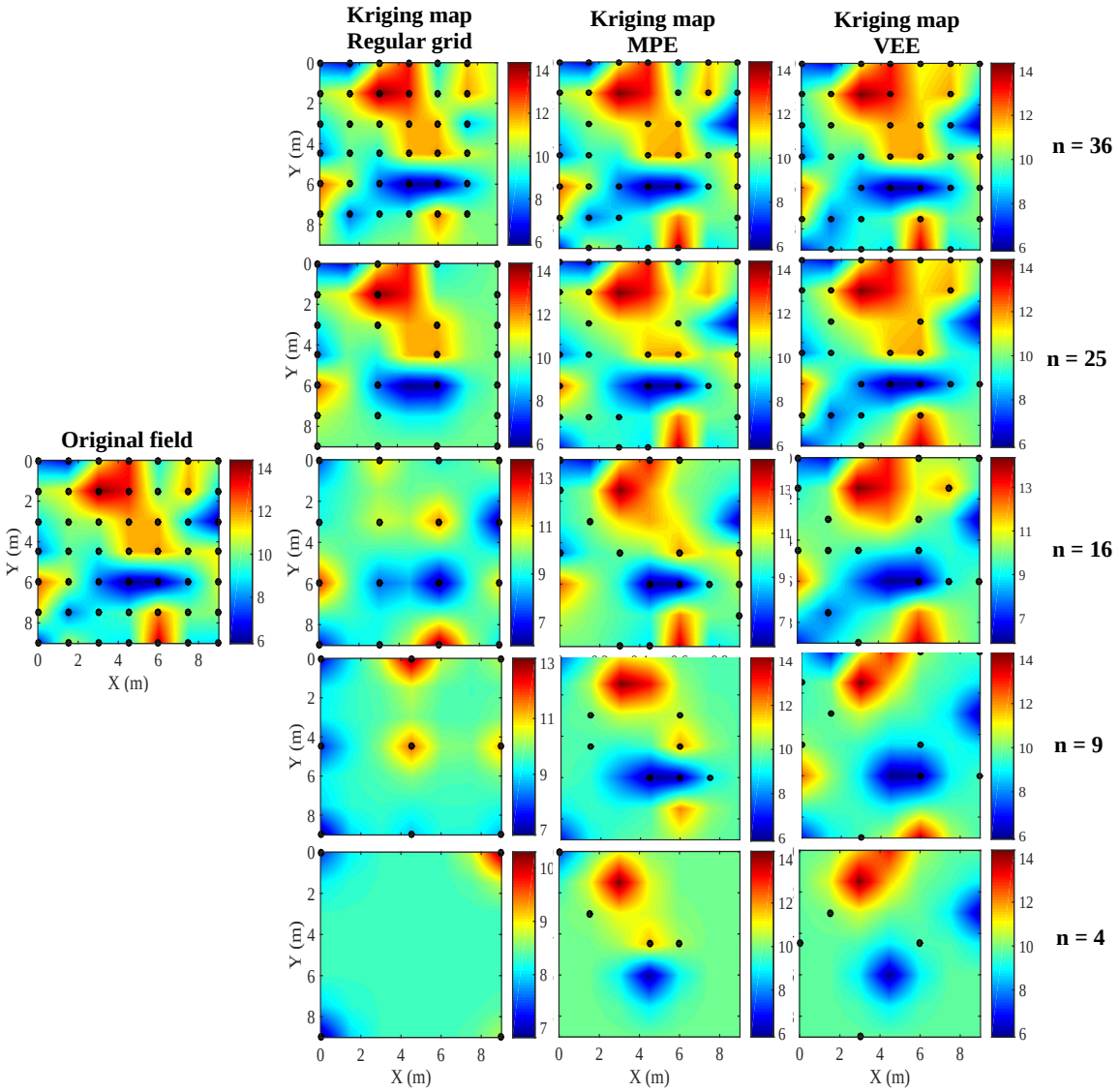

Figure 3-10. Illustration of OSSM comparing the regular grid and the optimized irregular grid for 36, 25, 16, 9 and 4 number of points (n) and MPE and VEE as the fitness functions.

As it can be seen, the difference between the regular grid kriging maps and the MPE and VEE maps, start being noticed at n = 25, but it becomes evident from n = 9. Additionally, when n = 36 not significant difference can be seen between the kriging maps of MPE and VEE. However, when n decreases, the difference starts to become more noticeable. MPE tries to choose the points that will create a kringing map more similar to the original field, including intermediary values. On the contrary, VEE will choose the points that will define the extreme values on the field (minimums and maximums).

3.5.1.2. Performance of OSSM with the modification of the range

As it was shown in section 3.2, the performance of kriging to predict unknown values can be affected by the correlation length. If C and Co are constant for different variograms, a higher prediction error will be obtained if the correlation length value is smaller, and less important if it is higher. As the chosen fitness functions (MPE and VEE) depend directly from the kriging results, it

is important to consider the affectation of OSSM when the correlation length is modified. In order to do this, OSSM performance was evaluated when different simulated fields have the same C, Co variogram parameters and same mean value, but different range (a).

A studied area with a correlation length too short (homogeneous field) or too long (highly heterogeneous field) can affect the performance of OSSM. Two alternative simulated fields with the same C, Co variogram parameters and same mean value as the simulated field of the previous section, but different *a* were created to this aim. Figure 3.11 shows the simulated fields and variograms for the three different ranges (*a* = 1.6, 2.6 and 3.6 m). As it can be seen, the correlation length can highly modify the appearance of a field with the same global variance and the same mean value. While the field with a = 1.6 m seems quite homogeneous, the field with a = 3.6 m seems very heterogeneous.

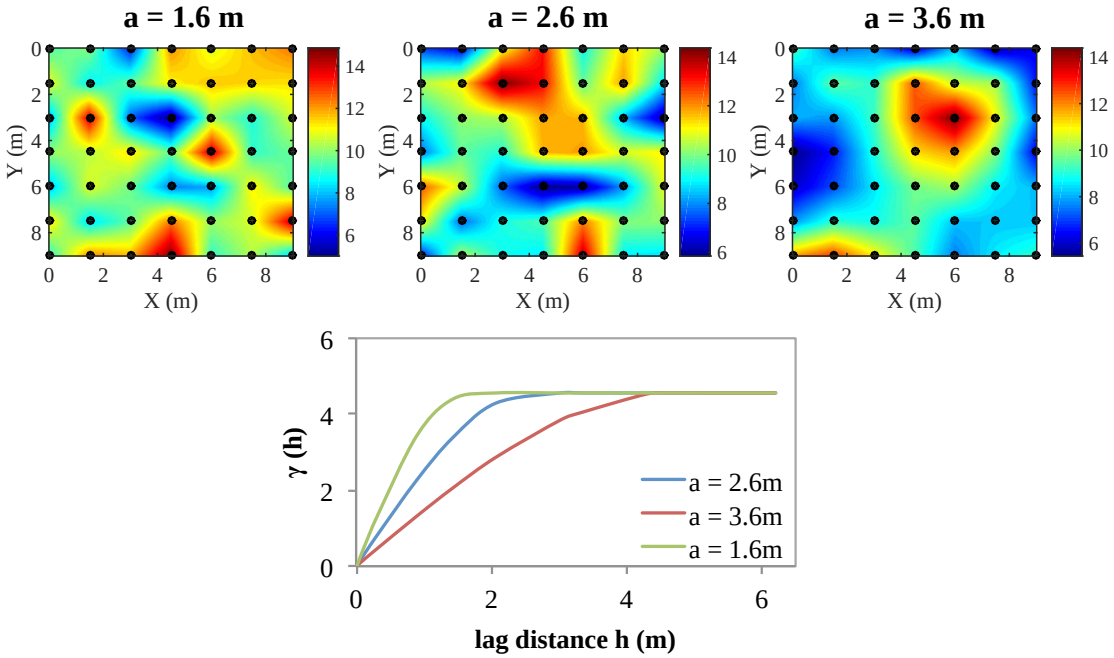

Figure 3-11. Simulated fields and variograms for a = 1.6, 2.6 and 3.6 m.

The performance of the OSSM was tested for the three data sets of the three different fields for an n = 16. Figure 3.12 shows the MPE and VEE in function of the range for the cases of n = 16 and n = 9. As it can be seen MPE decrease as *a* increases for the optimal grids of both *n*. The same behavior can be seen for the regular grid of *n* = 16, but for *n* = 9 the MPE values are similar for the regular grid. VEE seems to decrease as *a* increases for both *n* and both regular and optimal grid. Moreover, it can also be seen that a better optimization (decrease of fitness function values from a regular grid to an optimal one) can be obtained as the value of *a* is more important.

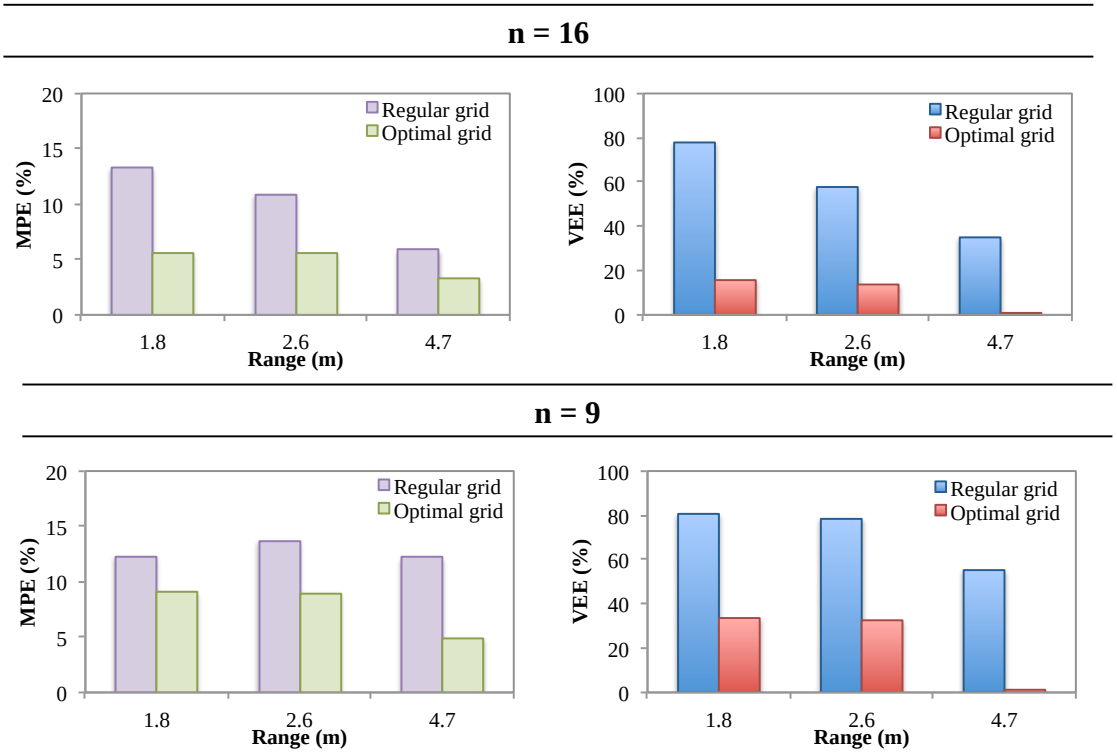

Figure 3-12. MPE and VEE in function of the range for the case of n = 16 and n = 9.

3.5.2. Validation of the OSSM on a case study: Thermal power plant in Le-Havre

3.5.2.1. Presentation of the structure

The thermal power plant operated by EDF and located in Le-Havre, France, is one of the sites being investigated for two French national research projects (C2D2-ACDC and EVADEOS), in which EDF is a partner. The objectives of these projects were to test a methodology to evaluate, by NDT, the concrete properties, and its variability in order to implement it in a model, which would predict the structure lifespan. The case study concerns confinement walls in three sub-zones of the plant (I, III and IV). The walls of these three zones were built in 1965, 2004, and 1973 respectively. The proximity of the sea induces severe environmental conditions for the concrete in terms of humidity and chloride content. The length of the walls varies from 5 to 20 m and their height is about 2 m. Figure 3.13a shows the location of the walls considered for the projects.

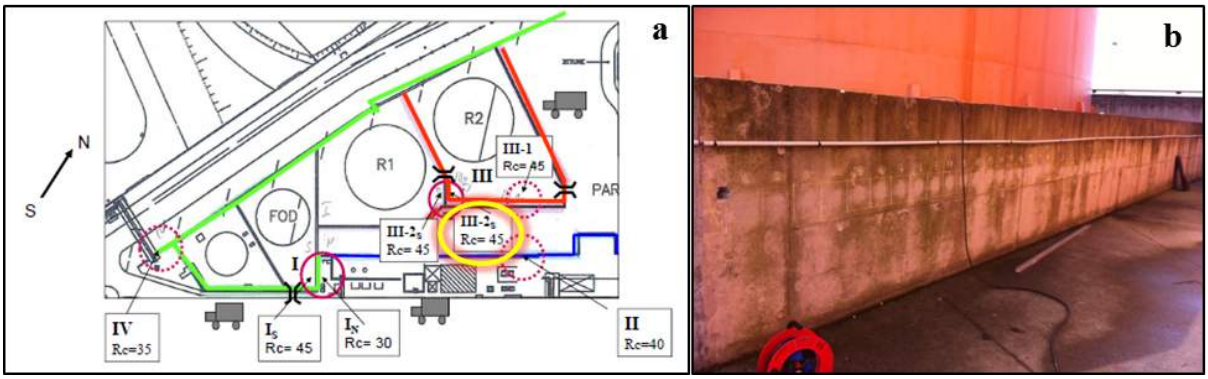

Figure 3-13. (a) Location of the chosen walls for the project. (b) Chosen wall for the case study (wall III-N).

The industrial approach of concrete assessment implies to reduce the number of NDT tests and cores to optimize the auscultation cost. Hence, the wall chosen for the case study was the wall III-N (figure 3.13b), which was built in 2004. Many NDT methods have been used in the projects, but only two methods, one acoustic (sensitive to compressive strength) and one electric (sensitive to saturation degree) were used here and analyzed to apply and validate the OSSM. The observables chosen were: ultrasonic pulse velocity and capacity of large electrodes – Permittivity.

3.5.2.2. Experimental tests using ultrasonic and capacitive measurements

Two types of measurements were made: one horizontal profile (1D) and two parallel horizontal profiles (2D). Because the low height of the wall (~1.80 m), it was decided to inspect only a horizontal profile to estimate the variograms for each studied observable. A series of 30 ultrasonic pulse velocity (UPV) and capacity of large electrodes – Permittivity (CLEP) measurements were made for pre-auscultation of the wall III-N to attain this objective. Additionally, a series of 10 CLEP measurements organized in two horizontal profiles were made for auscultation. Figure 3.14 shows the grid detail for pre-auscultation and auscultation, while figures 3.15a and 3.15b display the UPV at different locations of the wall along a horizontal profile with a fixed step and the CLEP map at different locations of the wall along two horizontal profiles with a fixed step.

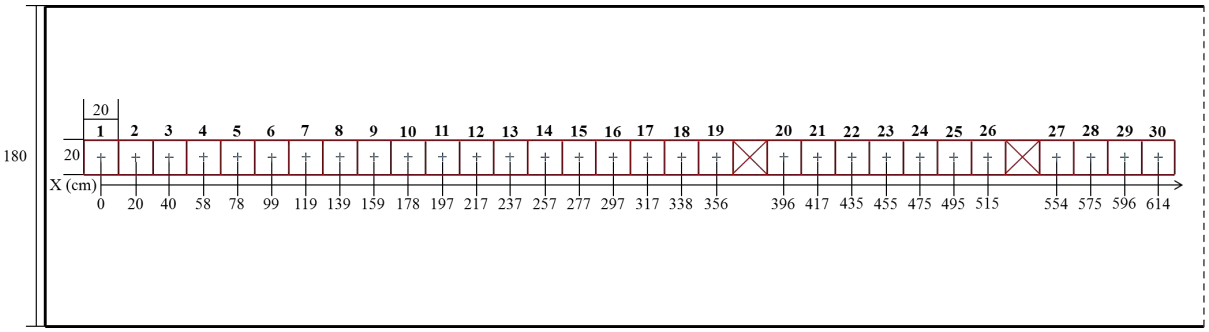

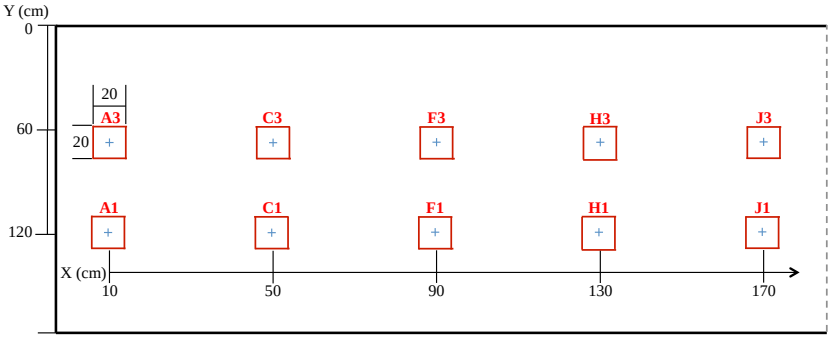

Figure 3-14. Grid detail for pre-auscultation and auscultation.

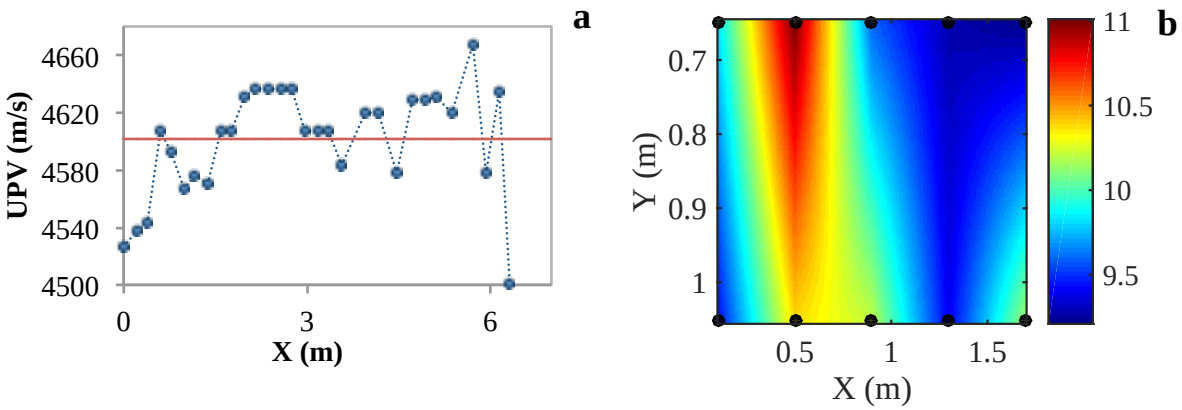

Figure 3-15. a) UPV original profile. b) CLEP original field.

Each mesh is 20x20 cm. UPV and CLEP measurements were taken at the center of each mesh to keep a distance of 20 cm between two measurements. This distance was chosen in order to be smaller than the expected correlation length. Such a value also guarantees that the volumes of concrete investigated with ultrasonic waves at two close measuring points are not overlapping.

3.5.2.3. Spatial sampling design for ultrasonic measurements

In the simulated data, we used a general case with 2D data. However, we consider 1D and 2D data on the case study. It can be emphasized that the 2D is more general, and the 1D is a particular simplified case. The algorithm is then adapted for the two cases. Figures 3.16a and 3.16b show the corresponding variogram of the measured values for each observable. The variograms in this case are unidirectional. For the UPV, an exponential variogram model (10) was fitted on the experimental data. The curve fitting results are a nugget equal to 0 $(m/s)^2$, a range of 0.62 m and a sill equal to 1 426 $(m/s)^2$.

$$\gamma(h) = 1\,426\left[1 - \exp\left(-\frac{h}{0.62}\right)\right] \tag{3.10}$$

However, for the CLEP a gaussian variogram model (11) was fitted on the experimental data. The curve fitting results are a nugget equal to 0.038, a range of 1.58 m and a sill equal to 0.062.

$$\gamma(h) = 0\ 062\left[1 - \exp\left(-3\left(\frac{h}{1.58}\right)^2\right)\right] \quad (3.11)$$

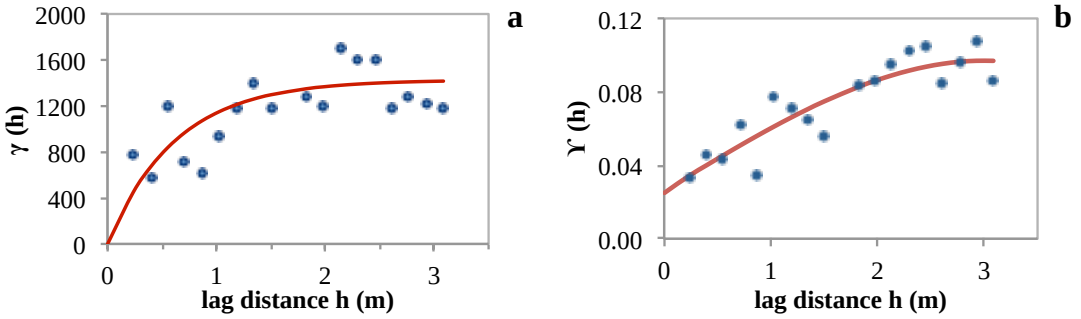

Figure 3-16. Variograms of UPV and CLEP.

The efficiency of the OSSM was explored with different sampling sizes (n). Figures 3.17a-d shows the variation of the two fitness functions – MPE (figure 3.17a and 3.17c) and VEE (figure 3.17b and 3.17d) – with n measurements organized on a regular grid (before the OSSM) and with location optimized on an irregular grid (after the OSSM). The MKSD was not taken into account due to the ineffectiveness of the function, previously demonstrated in the synthetic data example.

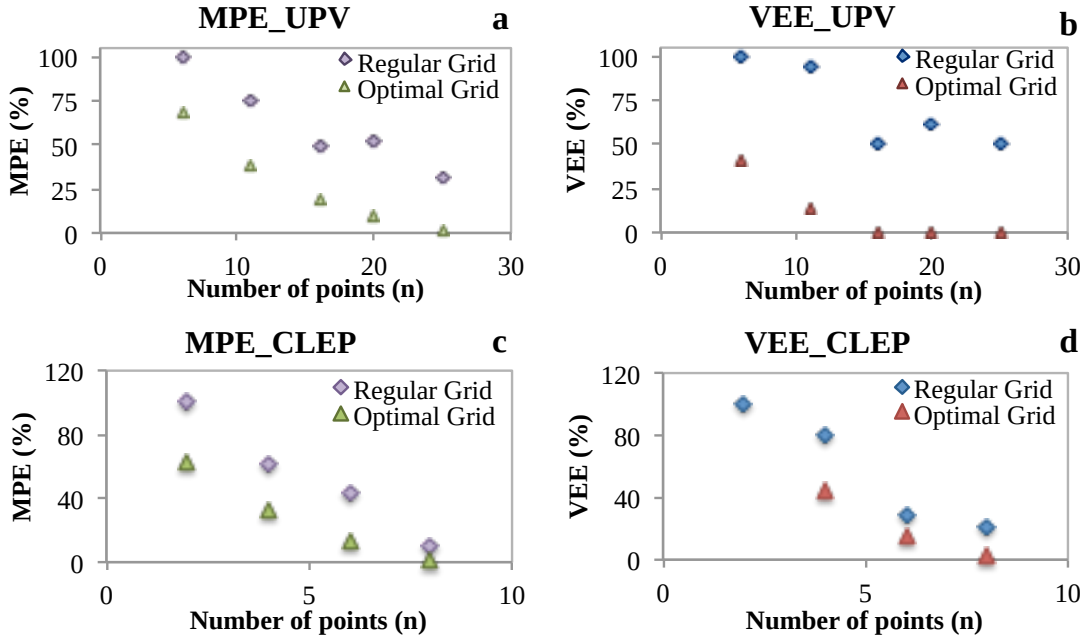

Figure 3-17. Relationship between each fitness function and the number of known values (n). a) MPE_UPV, b) VEE_UPV, c) MPE_CLEP and d) VEE_CLEP.

For the UPV case, if MPE is used as the fitness function, a significant decrease in the FFV can be seen (figure 3.17a). FFV decreases 34 % on average from a regular grid to an irregular one. Moreover, for the case of 20 measured values, the FFV decrease is around 42 %, and even for the minimum number of measured values (n = 6), the FFV decreases by 32 % from a regular grid to an irregular one. On the contrary, if VEE is used as the fitness function, a decrease of FFV even more important in average than the one from MPE (approximately 60%) is obtained. From figure 3.17b,

it can be inferred that, if n is reduced to 25, 20 or 16, the new global variance is equal to the one obtained with the original 30 measurements.

For the CLEP case, the decreases of the FFV values for both fitness functions (MPE and VEE) are not as significant as for the UPV case. However, if MPE is used as the fitness function, FFV decreases 26 % on average from a regular grid to an irregular one. Moreover, it can be seen in figure 3.17c that the reduction of FFV for different number of known values (n) is constant in average (approximately 30%), although for the case of 8 known values the decrease of FFV is only of 9%. This is expected knowing that the total number of CLEP measurements (N) is 10. On the contrary, if VEE is used as the fitness function, a decrease of FFV similar in average than the one from MPE (approximately 22%) is obtained. In figure 3.17d can be inferred that, if n is reduced to 8, the new global variance is equal to the one obtained with the original 10 measurements. However, it can also be seen that there is no tendency in the decrease of FFV from a regular grid to an irregular one and n, although no better solution could be found for the case of n = 2.

In the case of a small number of measured values, the difference between the two fitness functions (MPE and VEE) can be seen more clearly. In the case of UPV (figures 3.18a-c), an example of the kiging profiles obtained after OSSM with MPE (figure 3.18b) and VEE (figure 3.18c) as the fitness functions, and 6 known values (n = 6). Hence, 20% of the total number of measured values (N). In figure 3.18b, it can be seen that MPE searches for values to mimic the original UPV profile (figure 3.18a) as well as possible, while VEE searches for extreme values (figure 3.18c) to better approach the global variance. In the case of CLEP (figures 3.18d-f), an example of the kiging maps obtained after OSSM with MPE (figure 3.18e) and VEE (figure 3.18f) as the fitness functions, and 6 known values (n = 6), which means 60% of the total number of measured values (N). In figure 3.18e, it can be seen that with MPE it is almost obtained the same original CLEP field (figure 3.18d). However, with VEE, the extreme values zones (figure 3.18f) can be well identified.

In other words, reproducing the original UPV profile or CLEP field implies that all values (measured and predicted) will be as close as possible to original values, and the mean of all values will be similar to the mean of original values. Furthermore, the fact that VEE searches for extreme values induces that the variance of all values (measured and predicted) will be similar to the variance of original values. In table 3.2, it can be seen the statistical values (mean and variance) for both observables (UPV and CLEP) of the original fields and the kriged fields obtained after OSSM with MPE and VEE as the fitness functions, and n = 6. As it was expected, for both cases (UPV and CLEP), with MPE a mean closer to the original one is obtained, and with VEE a global variance closer to the original one is obtained.

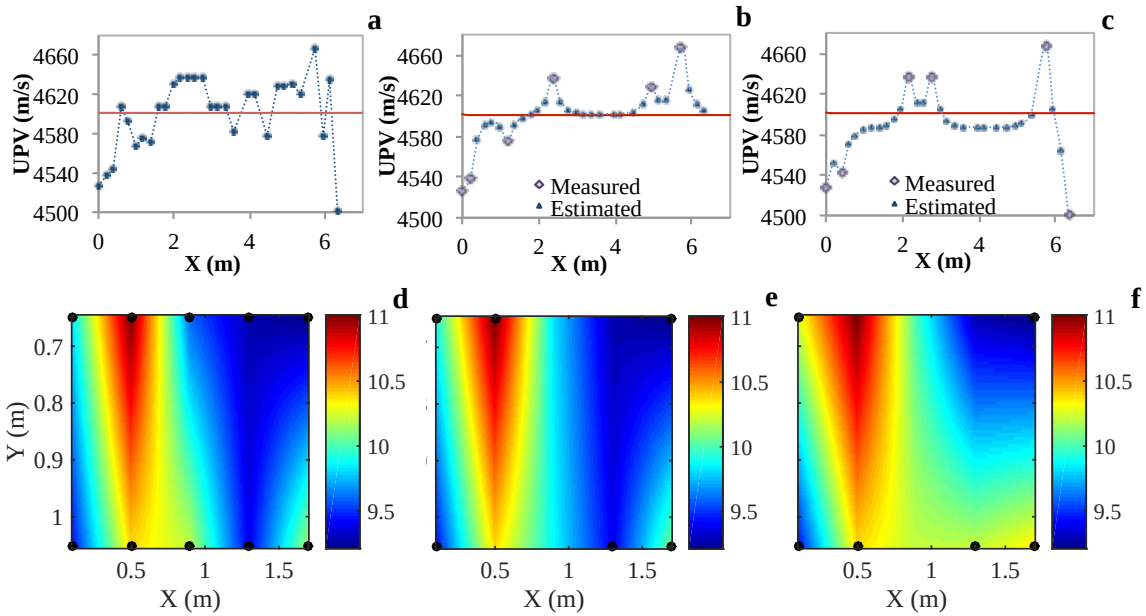

Figure 3-18. a) Original UPV profile, b) Kriging UPV profile after OSSM obtained with MPE as the fitness function and n = 6, c) Kriging UPV profile after OSSM obtained with VEE as the fitness function and n = 6, d) Original CLEP field, e) Kriging CLEP map after OSSM obtained with MPE as the fitness function and n = 4, f) Kriging CLEP map after OSSM obtained with VEE as the fitness function and n = 4.

Table 3-2. Mean and variance values for UPV and CLEP of the original fields and the kriged fields obtained after OSSM with MPE and VEE as the fitness functions, and n = 6.

		Original	MPE	VEE
UPV	Mean (m/s)	4601	4602	4589
	Variance (m^2/s^2)	1466	669	1002
CLEP	Mean	9.85	9.84	10.03
	Variance	0.34	0.31	0.32

The MPE and the VEE showed then interesting performance (a FFV decrease between 26% and 49% for MPE and between 22% and 76% for VEE from a regular grid to an optimal irregular one). It should be noted that the MPE leads to a smaller mean prediction error in the kriging map and a mean value closer to the original one than the VEE. On the other hand, the VEE provides a variance closer to the global variance than the MPE. Thus a specific attention must be paid to what is expected before selecting the most suitable fitness function for analyzing a particular data set. For instance, if the structure manager wants to know the spatial distribution of a property for future structure control or to locate the zones of maintenance, MPE should be used. If, on the contrary, he wants to estimate the global variability of the material for reliability computation, VEE should be used. However, a good compromise can be the combination of the two fitness functions using for example a multi-objective optimization for a better evaluation of mean and variance.

3.6. Conclusions

This chapter proposes an approach that may enable a concrete structure to be characterized efficiently by taking advantage of NDT methods with a good cost/benefit ratio. This approach is based on a 2-step strategy, in which a first investigation is carried out with a quick and low cost NDT technique, thus followed by the identification of specific areas where a refined investigation will be carried out with NDT or destructive test.

This contribution offers a new and formalized solution for an important problem of concrete structure evaluation and can be applied to a large variety of NDT methods and concrete structures such as bridges, building, tunnels, nuclear plants, etc. Moreover, it can be also expanded to other type of structure investigations (soils, masonries, tunnels, etc.).

Here, a preliminary study of a structure was carried out with a single NDT technique. Then, to select the most reliable and critical zones for complementary diagnosis (high quality NDT, coring, semi-destructive tests, etc.), an optimization spatial sampling method (OSSM) was developed. Three fitness functions were tested to quantify their efficiency in the OSSM: the Mean Kriging Standard Deviation (MKSD), the Mean Prediction Error (MPE) and the Variance Estimation Error (VEE).

These functions were analyzed for a simulated field and also for on-site ultrasonic pulse velocity and capacitive large electrodes permittivity measurements made on a wall of a thermal power plant in Le-Havre, France. The main conclusions are the following:

- It is possible to improve the knowledge of the material properties (mean, variance, extreme values) and to locate specific areas where the investigation will be refined, by using a methodology based on variographic theory. When compared to investigation programs based on a regular grid, it enables to reduce the number of measurements to reach a given quality and/or to increase the quality if the number of measurements remains constant.

- The MKSD fitness function does not provide an improvement in the representation of the simulated field from *n* measurements organized in a regular grid to *n* measurements arranged in an irregular grid after OSSM. This was revealed by a decrease of only 0.39% in the FFV of MKSD. Furthermore, the global variance calculated after OSSM was almost the same as the one obtained with a regular grid.

- MPE and VEE as fitness functions showed a high improvement in the representation of all cases studied (simulated field and on-site ultrasonic velocity measurements). The use of these two fitness functions considerably increased the global variance value from a regular

grid to an optimal irregular grid, not only in the case of simulated data but also in the case study.

- In the simulated data case, the FFV of MPE decreased by 49% on average for all numbers of points *n*, while the FFV of VEE decreased by 76%. The performance of the OSSM algorithm was not as good in the on-site case, where the FFV of MPE decreased by 34% for UPV and by 26% for CLEP, while the FFV of VEE decreased by 60% for UPV and by 26% for CLEP. This is due to the fact that the simulated case presents more variability and the measurement error was not considered. It may seem that VEE is the best choice for a fitness function but it is important to point out that MPE and VEE have different objectives and they may be complementary. The choice of one fitness function has to be done by considering the real objectives of the material assessment (mainly mean values or variance).

- The MPE and VEE values are affected by the variation of *n* and *a*. Both values decrease as *a* increases, and both values increase as *n* decreases.

- As VEE and MPE have complementary information, a good compromise can be the combination of the two fitness functions using for example a multi-objective optimization for a better evaluation of mean and variance.

References

[1] Nguyen, N.C., Sbartaï, Z.M., Lataste, J.F., Breysse, D., Bos, F., Assessing the spatial variability of concrete structures using NDT techniques – Laboratory tests and case study, Construction and Building Materials, vol. 49, 2013, pp. 240-250.

[2] O'Connor AJ, Kenshel O. Experimental evaluation of the scale of fluctuation for spatial variability modeling of the chloride-induced reinforced concrete corrosion. Bridge Engineering, vol. 18, 2013, pp. 3-14.

[3] Borosnyoi A., Szilagyi K. Studies on the spatial variability of rebound hammer test results recorded at in-situ testing. Építőanyag - Journal of Silicate Based and Composite Materials, vol. 65, 2013, pp. 102-106.

[4] Schoefs F, Tran TV, Bastidas-Arteaga E, Villain G, Derobert X, O'Connor AJ, Bonnet S. Optimization of non-destructive testing when assessing stationary stochastic processes: application to water and chloride content in concrete. Proceedings of the International Conference Durable Structures (ICDS12), Lisbon – Portugal, 31 May – 1 June 2012, p. 14.

[5] Stewart MG, Suo Q. Extent of spatially variable corrosion damage as an indicator of strength and time-dependent reliability of RC beams. Engineering Structures, Vol 31, 2009, pp. 198–207.

[6] Van Groeningen, J.W., Siderius, W., Stein, A., Constrained optimization of soil sampling for minimization of the kriging variance, Geoderma, vol. 87, 1998, pp. 239-259.

[7] Ferreyra, R.A., Apeztegui, H.P., Sereno, R., Jones, J.W., Reduction of soil water spatial sampling density using scaled semivariograms and simulated annealing, Geoderma, vol. 110, 2002, pp. 265-289.

[8] Melles, S.J., Heuvelink, G.B.M., Twenhöfel C.J.W., Van Dijk, A., Hiemstra, P.H., Baume, O., Stöhlker, U., Optimizing the spatial pattern of networks for monitoring radioactive releases, Computers & Geosciences, vol. 37, 2011, pp. 280-288.

[9] Stein, A., Ettema, C., An overview of spatial sampling procedures and experimental design of spatial studies for ecosystem comparisons, Agriculture, Ecosystems and Environment, vol. 94, 2003, pp. 31-47.

[10] Gomez-Cardenas, C., Sbartaï, Z.M., Balayssac, J.P., Garnier, V., Breysse, D., "New optimization algorithm for optimal spatial sampling during non-destructive testing of concrete structures", Engineering Structures, vol. 88, 2015, pp. 92-99, http://dx.doi.org/10.1016/j.engstruct.2015.01.014.

[11] Bohling, G., Kriging, C&PE 940, 2005, p. 1-20.

[12] Pardo-Igdzquiza, E., Chica-Olmo, M., The Fourier Integral Method: An efficient spectral method for simulation of random fields, Mathematical Geology, vol. 25, n° 2, 1993, pp. 177-217.

CHAPTER 4

CONSIDERATION OF UNCERTAINTIES ON DESTRUCTIVE TESTS IN THE DATA FUSION PROCESS

4.1. Introduction

Non Destructive Testing (NDT) provides on-site measurements by following procedures that allow the creation of concrete sustainability indicators by data fusion. Its exploitations are initially studied in the laboratory. They lead to correlation laws between the NDT measurements called "observables" and the concrete properties called "indicators". As described in chapter 2, these laboratory laws were developed in the SENSO project in a multi-linear form, mostly involving two indicators regarding data fusion applications for concrete characterization.

Nevertheless, the direct use of these correlations laws for in situ measurements and the identification of the concrete indicators are not possible: supplementary and unmonitored parameters others than the evolution of indicators due to environmental conditions (moisture, wind, etc.), generate biases between the known laboratory correlation laws and the unknown on-site ones. A fusion data tool developed in the ACDC project and described in chapter 2 [1] improves the assessment of indicators (Saturation, Compressive strength, porosity, etc.) on concrete structures from on-site NDT measurements. This tool takes into account the reliability and sensitivity of observables for each one of the indicators. Moreover, for the transfer of the correlation developed in laboratory to on-site measurements, it is required an adaptation and updating phase in order to take into account the potential biases, due to concrete variability.

In this chapter, two types of updating proposed and developed in the ACDC project are described to adapt the fused values to the studied structure: i) updating by the inputs made directly from on-site NDT and DT measurements, and ii) updating by the outputs using the results of the fusion [2]. Figure 4.1 shows the fusion process with the mentioned updating methods. As it can be seen, the fusion process starts by combining the measured observables using the described data fusion tool to obtain the Fused Indicators (FI) and the quality estimators (EQ) [3] for each auscultated point. If the EQs are not acceptable, the updating by inputs will be made. This update will take into account not only the measured observables, but also the indicators obtained by destructive tests (DTI) when available, in order to modify the correlation laws. The fusion process will be repeated to obtain new FI and new EQs for each auscultation point. If the EQs are still not acceptable, an updating by outputs called coherence (COH) will be made. This updating will take into account only the EQs to modify the correlation laws. The fusion process will be repeated until the FI obtained have acceptable EQ values. Finally, to adapt FI values to the DTI values a updating by outputs called Affine Transformation (AT) is made. This updating will take into account the DTIs and the FIs obtained after the first updating to obtain the final values of the adjusted indicators (FI_{AT}) for each auscultation point.

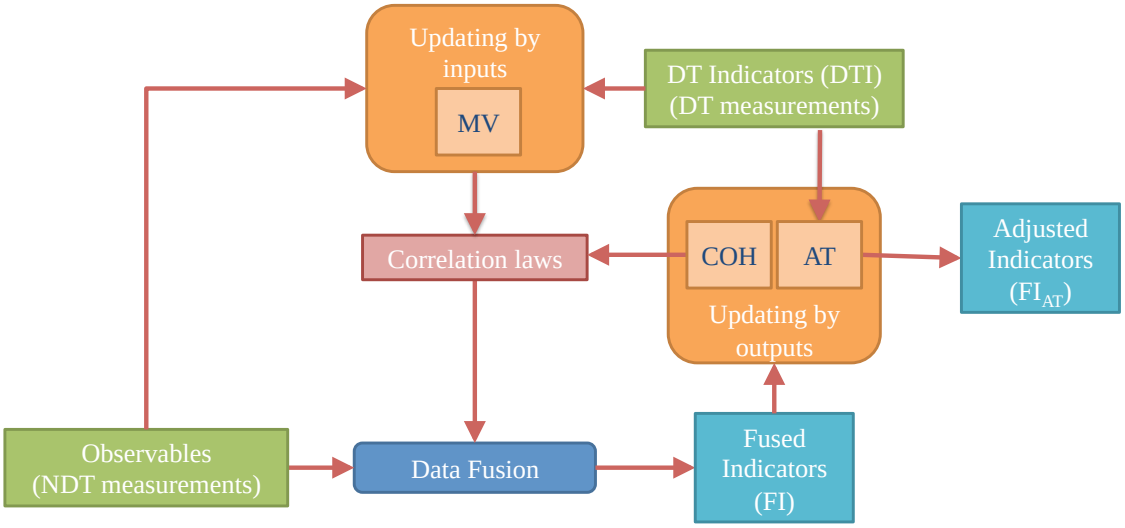

Figure 4-1. Flowchart of the fusion process with its respective updating methods.

However, as it was described in chapter 2, NDT measurements and DTs made on extracted cores can lead to variable results in a zone considered homogeneous, making the results in a specific auscultation point uncertain and unreliable. These uncertainties can be included and propagated in the fusion and the updating processes to obtain a precision on the final FI_{AT} values for each auscultation point. Figure 4.2 shows how the NDTs and DTs uncertainties are included and propagated in the fusion and updating processes. As it can be seen, the NDT uncertainties are introduced in the observables and they can propagate directly on the fusion and updating by inputs processes. However, these uncertainties are assumed treated in the fusion process, as they are included in the distribution of possibilities for each observable. Nevertheless, the DTIs uncertainties are introduced in the DTIs and they can propagate directly in the updating by inputs and the updating by affine transformation. In the ACDC project, the propagation of DTs uncertainties through the updating by inputs showed not to be the best approach, as the method used for this update uses a mean value of NDTs and DTs, thus, it is not sensitive to DTs uncertainties. That leaves us with the propagation of DTs uncertainties through the updating by affine transformation.

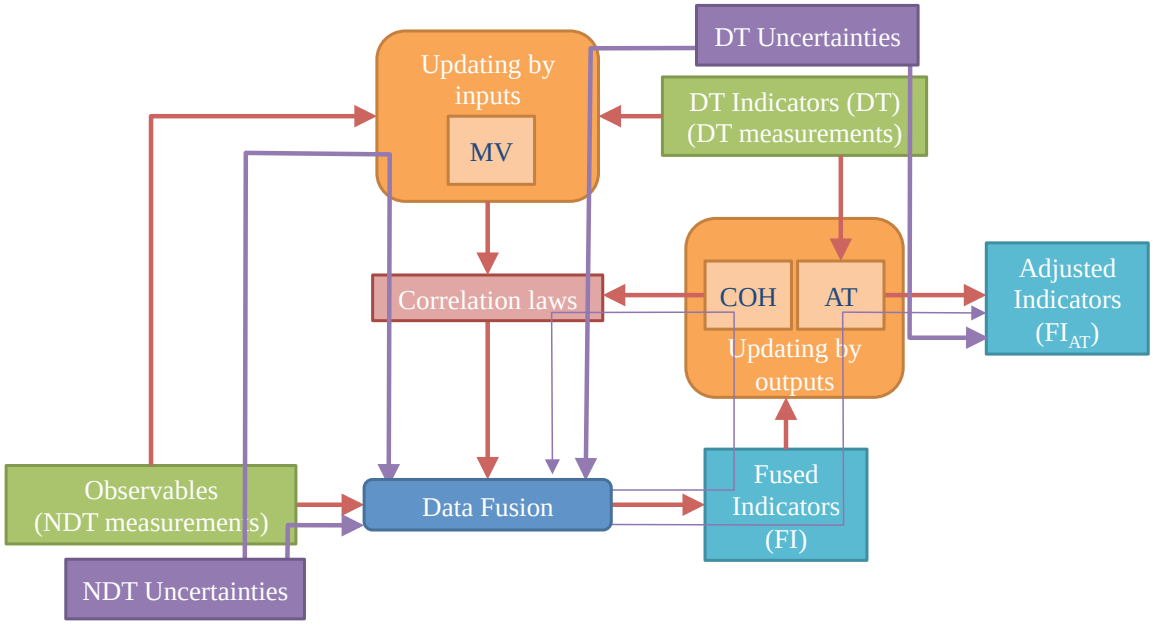

Figure 4-2. Flowchart of the fusion process, its respective updating methods and the NDT and DT uncertainties.

Therefore, in this chapter a method to propagate these DTs uncertainties through the updating by affine transformation is proposed to obtain ranges of possible fused indicator values for each auscultated point, called in this chapter errors or precisions. This method is applied to a case study (Marly's bridge), where two indicators are obtained (saturation degree and compressive strength) from the fusion of three different observables (Impact Echo dynamic modulus, Capacitive Large Electrodes Permittivity and GPR Direct Wave Velocity). The propagation of compressive strength and saturation degree DT uncertainties is made to obtain a mean error of all auscultation points for each studied indicator. Then, the influence of the variation of indicators DTs uncertainties on their errors is studied, as well as the influence of their errors on the number and selection of cores to be extracted.

4.2. Updating by inputs: Mean value method (MV)

As it was introduced in chapter 2, the employed fusion data tool is based on the SENSO project correlation linear laws between the observables of table 2.11 and the indicators. This correlation laws were obtained with samples made in laboratory, and the general equation for each indicator is:

$$O_i = a_i + b_i \cdot I_j \tag{4.1}$$

Hence, to adjust the obtained fusion indicators to the structure, it is necessary to update the correlation laws. The proposed method in the project ACDC consists in using the mean of each NDT measurements and the mean of the studied indicators obtained by destructive tests (DT) from cores extracted directly from the structure. Both means correspond to a "reference value"

necessary to update the correlation law by moving it to the reference value. In other words, the updating of the correlation law is made by changing the coefficient a_i of the equation 4.1. This method of updating is called updating by a mean value (MV) and its principle is illustrated in figure 4.3.

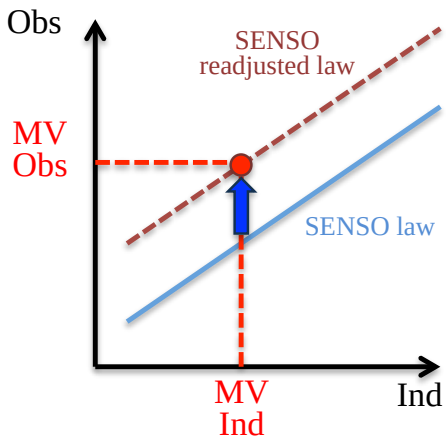

Figure 4-3. Principle of updating by a mean value (One observable, one indicator simplified case).

This method modifies the correlation laws to improve convergence of the possibility distributions of the fused results, which increase the EQ values (described in chapter 2) and, thus, the reliability of the results. However, MV may not be enough to make the results of the fusion reliable.

4.3. Updating by outputs

4.3.1. Updating by coherence (COH)

When EQ values are still not acceptable after the updating by a mean value, another method called updating by coherence (COH) was developed to assure a good convergence, hence, elevated EQ values, consequently, reliable results. This method consists in modifying the coefficients a_i and b_i of the Eq. 1 by optimizing a cost function (equation 4.2).

$$J(a_i, b_i) = \sum_{k=1}^{q} [1 - \mathrm{EQ}_k(a_i, b_i)]^2 \qquad (4.2)$$

The objective is to ensure the convergence of the possibility distributions of the fused values results in the indicators plan I_1 and I_2 for all the measured points.

Once the convergence is ensured, another updating can be made to update the fused results of all measured points to the DT results. This updating is called affine transformation and it is described in the next section.

4.3.2. Updating by affine transformation (AT)

When the possibility distributions of the fused values results are more coherent after the first updating, it is time to update the indicators values obtained from the fusion after the first updating (FI) to the DTs indicators values obtained from the *n* cores extracted (DTI). To make it happen, an Affine Transformation (AT) is made to link the DTI and the FI by a linear relationship (equation.4.3).

$$DTI_{n,j} = c\left(FI_{n,j}\right) + d_j \tag{4.3}$$

Where $DTI_{n,j}$ represents the *n* DTI values for the indicator j, $FI_{n,j}$ represents the *n* FI values for the indicator j and *c* and d_j represent the linear AT coefficients where the value of d_j depends on the indicator j.

The AT objective is to do a linear regression to estimate the AT coefficients (c,d_j) from the Eq. 3 relation, which will be fundamental to obtain the new FI updated values (FI_{AT}) on the *N* auscultation points (equation 4.4). Figure 4.4 illustrates the updating by inputs and outputs methods in a two-steps updating.

$$FI_{AT(N,j)} = c\left(FI_{N,j}\right) + d_j \tag{4.4}$$

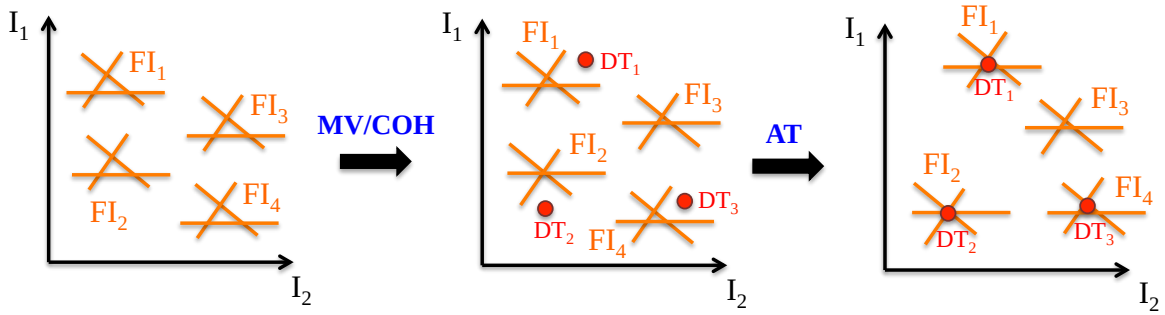

Figure 4-4. Illustration of the two-steps updating: MV/COH and AT for 4 fused indicators values (FI), 3 NDT fused Observables (orange lines) and 3 DT measured values (red points).

The updating by AT process allows to adapt the *N* fusion indicators to the *n* DT indicators. However, as it is known, it is impractical and expensive to extract several cores in the same zone considered homogeneous for different auscultation points of a structure, to have more reliable DTI results. Hence, there is always going to be uncertainties on DTI results when cores are extracted from site. It is expected to reduce these uncertainties and manage their influence on the result of fusion process.

The objective of this chapter is to give to the structure manager a precision on all indicators values evaluated by NDT in function of the number of the cores to be extracted. To this aim, it is necessary to insert the uncertainties on the DTIs, and to propagate them on the fused data after the

first updating (FI) for each auscultation point. The principle of this method is presented in the following section.

4.4. Optimizing on-site core selection depending on the indicator DT uncertainty/variability

4.4.1. Presentation of the methodology

In this section, it is presented a method to assess the sensitivity of FI_{AT} to DTIs uncertainties, as well as the influence of DTIs uncertainties to the number and selection of extracted cores. Figure 4.5 shows the principle of the method to introduce and propagate the DTIs uncertainties on FI_{AT} values for each auscultation point. As explained in the introduction, the DTIs uncertainties are propagated through the updating by the AT.

The first step is to create a simulated DTI reference corresponding to the knowledge of DT values for each point of the database. In figure 4.5, it can be seen that if we use the AT coefficients from a previous inspection (c_R and $d_{R,j}$) and the fused indicators after the first updating on the *N* auscultation points ($FI_{(N,j)}$), we can create this reference base of *N* number of values ($DTI_{R(N,j)}$). The second step is to introduce a DTI uncertainty value to this reference base, called uncertainty indicator (aa_j) and its distribution discretized in 10 000 values, to propagate them through the updating by the AT process. At the end, we obtain the FI_{TA} values for each auscultation point, in which each one is the mean of the 10 000 found after the updating by AT. For each auscultation point it is also found a standard deviation ($\sigma FI_{AT(i,j)}$). The mean of all $\sigma FI_{AT(i,j)}$ obtained is the error used in this study.

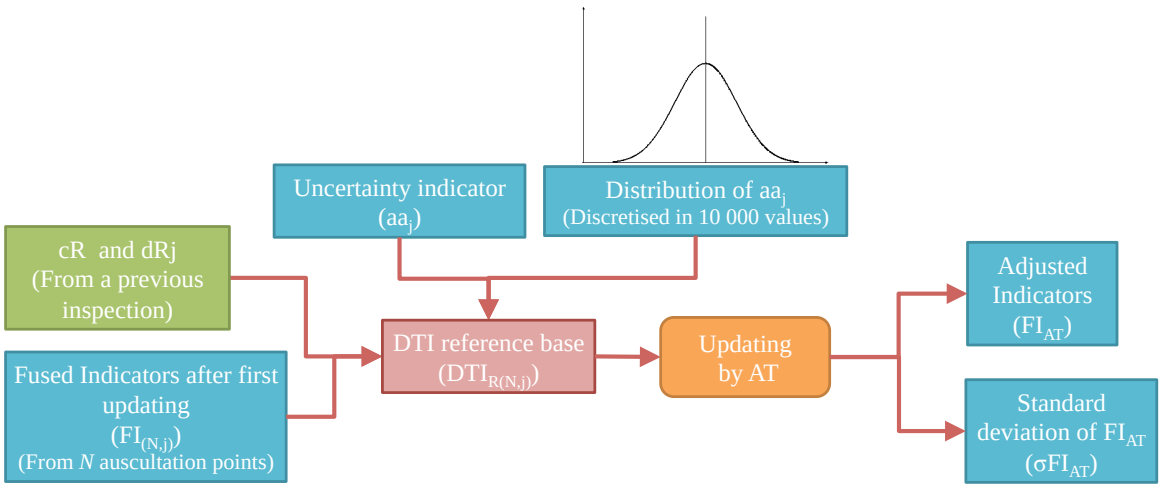

Figure 4-5. Illustration of the method to introduce the DTIs uncertainties on FI_{AT} values for each auscultation point.

The $\sigma FI_{AT(N,j)}$ values may vary depending on the number of cores, hence, number of DTIs. Moreover, they can also vary depending on the distribution of values the DTIs may have in the auscultated structure. The next section are going to describe the detail of the introduction and

propagation of the DTIs uncertainties on FI_{AT} values for each auscultation point and the illustration of this method on a case study (Marly's bridge-France). It is also going to be described a method to study the influence of the number and values distribution of the DTIs on $\sigma FI_{AT(i,j)}$ for the case study.

4.4.2. Insertion of uncertainties on DT data and their propagation to fused results

As mentioned in the last section, the AT creates a linear relationship between the FI and the DTI. To introduce DT uncertainties, several steps may be followed.

First, a $DTI_{R(N,j)}$ reference base for both indicators is created using the AT coefficients (c_R, d_{Rj}). These AT coefficients are estimated form the $DTI_{(n,j)}$ of the *n* extracted cores and the $FI_{(n,j)}$ results on the same positions as the $DTI_{(n,j)}$ from a previous inspection. For creating $DTI_{R(N,j)}$, c_R, d_{Rj} and the results obtained after the first updating $FI_{(N,j)}$ are used in the equation 4.5.

$$DTI_{R(N,j)} = c_R\left(FI_{(N,j)}\right) + d_{Rj} \tag{4.5}$$

If there are not $DTI_{(n,j)}$ and $FI_{(n,j)}$ results from a previous inspection available, the values of c_R and d_{Rj} will be given the value of 1. Then, an uncertainty indicator (aa_j), one for each indicator *j*, which can be estimated by previous experiences (see chapter 2) or given by the laboratory is introduced in the DTI reference base ($DTI_{R(N,j)}$) by creating 10 000 simulated values ($dti_{i,j,k}$) randomly for each $dti_{R(i,j)}$ value following an uniform distribution.

For example, for a value $dti_{Ri,j}$:

$$dti_{i,j,k} = a_R\left(fi_{i,j}\right) + b_{Rj} + vaa_{j,k} \tag{4.6}$$

Where $vaa_{j,k}$ is a random number between –aa and aa and $dti_{i,j,k}$ is the kth simulated value of $dti_{R(i,j)}$. The counter *i* represents a value on the $DTI_{R(N,j)}$ base, *j* represents the indicator and k represents the number of the simulated value. Therefore, for each $dti_{R(i,j)}$, there will be an uniform distribution with a standard deviation. As it could be seen in chapter 2, for several indicators, a normal or lognormal distribution could have been more appropriate to propagate the uncertainties, as these distributions have been generally found for most indicators values obtained by destructive test. However, the choice of a uniform distribution was chosen for this study to illustrate the methodology that can be used with any statistical distribution.

Later, the propagation of the DTs uncertainty is made. Having 10 000 $DTI_{R(N,j)}$ sets, and using the $FI_{(N,j)}$ obtained from the current inspection, it can be calculated 10 000 AT coefficients (*c* and d_j) with the following expression (example for the kth simulated value of $dti_{R(i,j)}$):

$$DTI_{n,j,k} = c_k(FI_{n,j}) + d_{j,k} \tag{4.7}$$

Afterwards, each c_k and $d_{j,k}$ are used to estimate 10 000 $FI_{AT(i,j)}$ for each auscultation point. At the end, for each auscultation point, a matrix $FI_{AT(i,j,10\,000)}$ with a uniform distribution, with a mean value and a standard deviation ($\sigma FI_{AT(i,j)}$) is obtained for each auscultation point of $FI_{AT(N,j)}$.

4.5. Insertion of uncertainties on DT data of a case study: Marly Bridge - France

4.5.1. Presentation of the structure

The auscultated bridge, located in Marly, France, is one of the sites being investigated for a French national research project (C2D2-ACDC), in which SETRA is a partner. The objectives of this project are to provide a framework for preventive monitoring of reinforced concrete structures and to assess by NDT, the concrete properties and pathologies. Additionally, it will also help to identify degradation models for concrete structures to eventually show how it is possible to enhance the results of predictive modeling through NDT.

The case study concerns three piles (S, ZBL and Sadam) of the bridge that was built in 1965. The exposure of these piles encourages critical environmental conditions for the concrete in terms of humidity. The length of the piles is about 2 m and their height is about 18 m. Figure 4.6 shows the location of the auscultated piles.

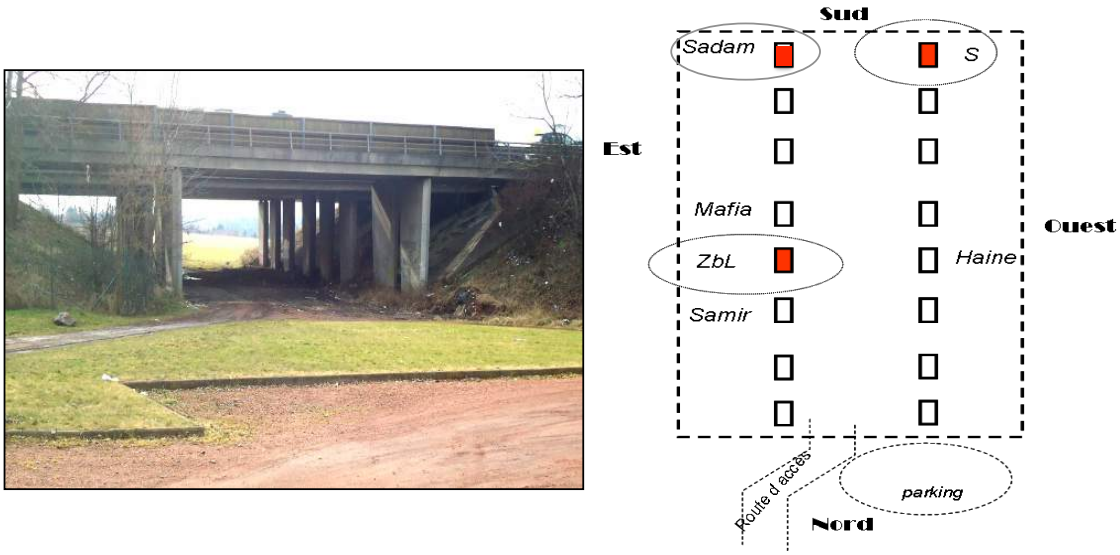

Figure 4-6. Location of the auscultated piles.

The industrial approach of concrete evaluation implies to use the NDT fusion data tool developed during this project to assess concrete properties and pathologies. These fusion results are improved by taking into account the DTIs uncertainties and to propagate them into the updating by AT process to see their influence into fusion results. Hence, 49 measurements points from the three auscultated bridge piles were chosen for the DTI uncertainty study. Several NDT methods were used on this site, but for this study, only the impact echo,

capacitive and GPR methods were selected here to assess the compressive strength (Rc) and saturation degree (Sr) of the concrete piles. A series of 49 Impact Echo dynamic modulus (IEE), Capacitive Large Electrodes Permittivity (CLEP) and GPR Direct Wave Velocity (DWV) measurements were made for the auscultation of the piles. Figure 4.7 shows the grid detail of the auscultation points. Moreover, 7 DTI results for Sr and Rc obtained from 7 cores extracted from a previous inspection were used for this study.

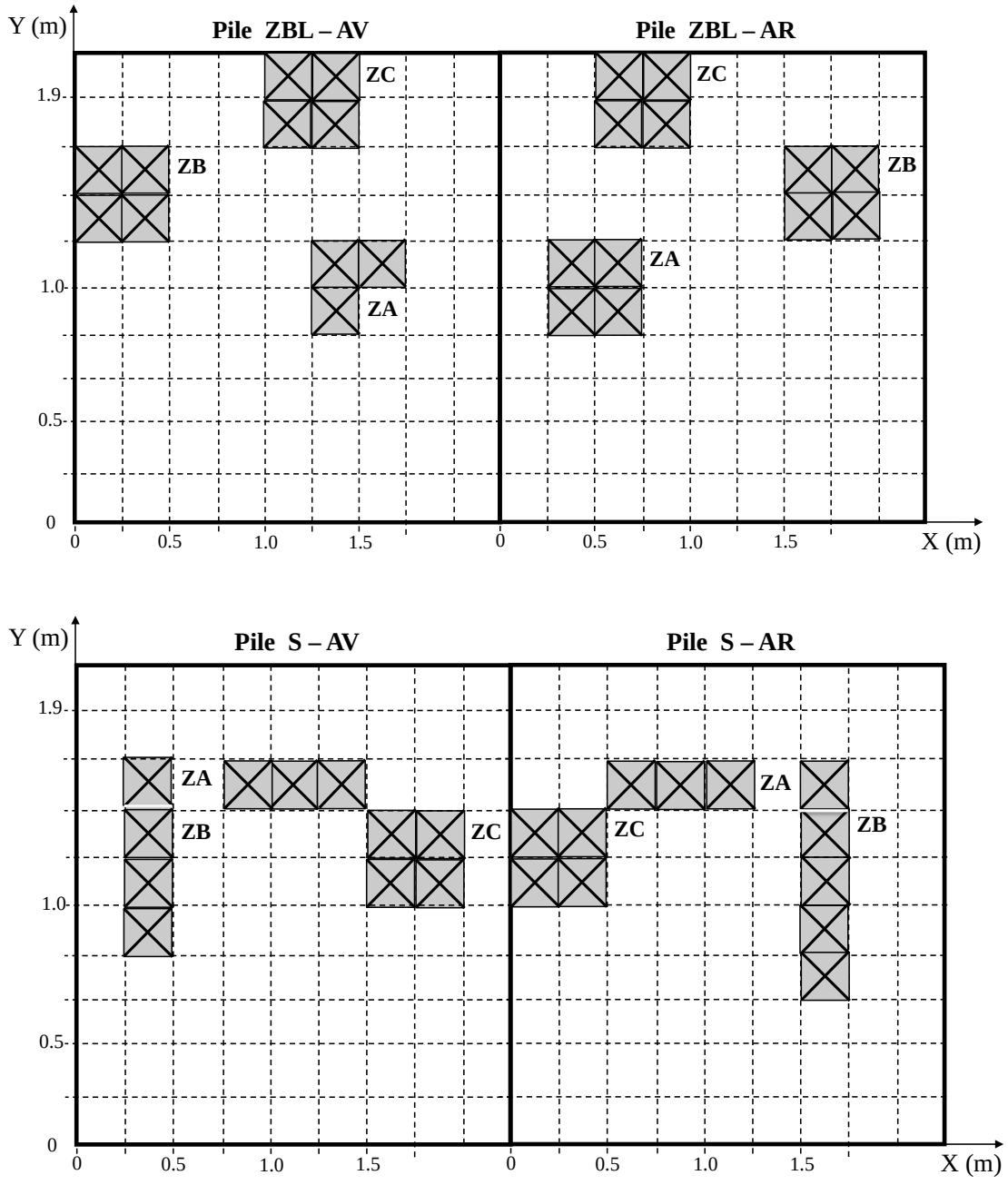

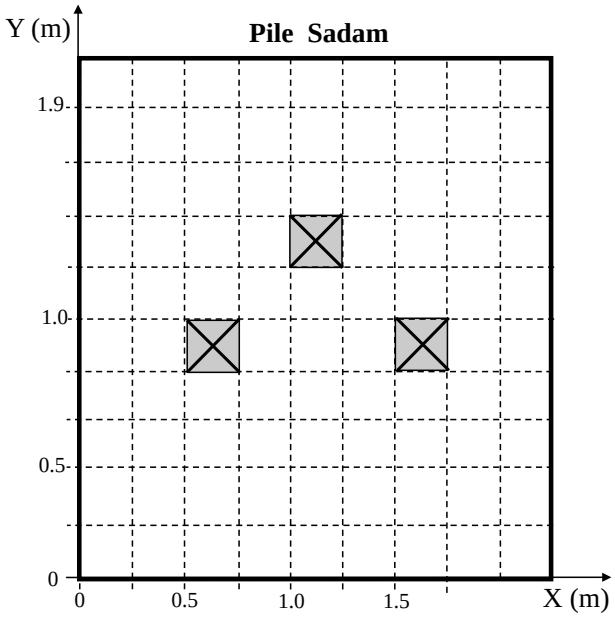

Figure 4-7. Grid detail of the auscultation measurements.

4.5.2. Introduction of uncertainties on compressive strength and saturation degree DTs

As it was presented in the section 4.4, to begin we have to create a reference base ($DTI_{R(N,j)}$) that will allow us to introduce DTIs uncertainties. On this case study, in order to create this base, the Equation 5 is used, where j=1 represents Sr and j=2 represents Rc. Furthermore, the AT coefficients (c_R, d_{RSr}, d_{RRc}) (Table 4.1) that were estimated from DTs made from 7 cores from a previous inspection, were used to create the $DTI_{R(49,j)}$. Figures 4.8a and 4.8b show the reference base values for Sr and Rc.

Table 4-1. AT coefficients for the creation of $\boldsymbol{DTI_{R(49,j)}}$.

c	1.39
d_{Sr} (%)	-36.32
d_{Rc} (MPa)	-17.25

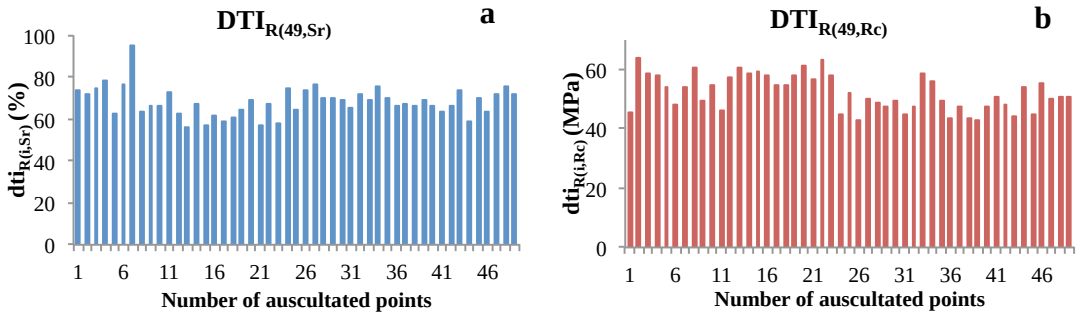

Figure 4-8. Reference base values $DTI_{R(N,j)}$ for: a) Sr and b) Rc.

From $DTI_{R(49,j)}$, the introduction of uncertainties on Sr and Rc DTs is made with the Equation 6. The uncertainty indicators, aa_{Sr} = 10% and aa_{Rc} = 5 MPa, were estimated from

previous experiences. Figures 4.9a and 4.9b show the $FI_{AT(49,,j)}$ and $\sigma FI_{AT(49,,j)}$ for both indicators. A mean of 2.94% for $\sigma FI_{AT(49,1)}$ ($<\sigma FI_{AT(49,Sr)}>$) and a mean of 1.67 MPa for $\sigma FI_{AT(49,2)}$ ($<\sigma FI_{AT(49,Rc)}>$) for all the 49 auscultated points. As expected, the $FI_{AT(49,j)}$ values obtained after the introduction of the uncertainties are exactly the same as the values of the reference base $DTI_{R(49,j)}$, since the objective of the introduction of uncertainties is to obtain a standard deviation (quantified degree of uncertainty) for the fusion results for all 49 auscultation points.

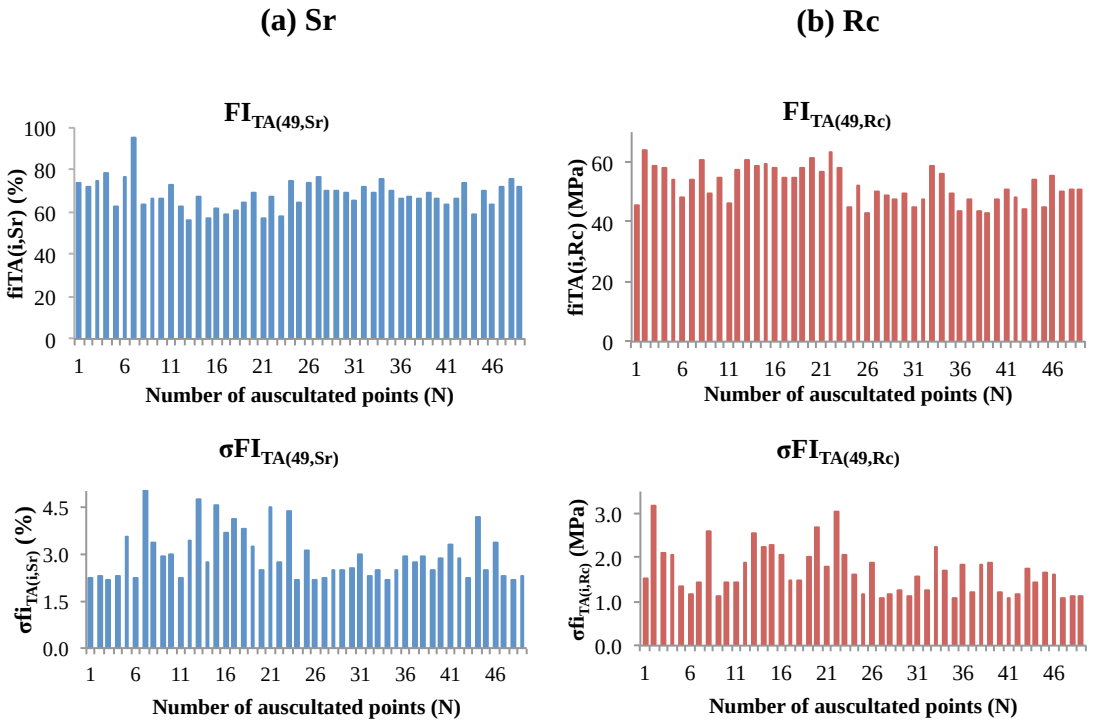

Figure 4-9. $FI_{AT(49,j)}$ and $\sigma FI_{AT(49,j)}$ for: a) Rc and b) Sr.

4.5.3. Influence of the variation of uncertainty indicators values (aa_{Sr} and aa_{Rc}) on the errors $<\sigma FI_{AT(49,Sr)}>$ and $<\sigma FI_{AT(49,Rc)}>$

In the previous section, $<\sigma FI_{AT(49,Sr)}>$ and $<\sigma FI_{AT(49,Rc)}>$ for all 49 auscultated points of Marly's Bridge were calculated with specific values of aa_{Sr} and aa_{Rc}. However, if the values of aa_{Sr} and aa_{Rc} vary, it would have a direct effect on the variation of the errors $<\sigma FI_{AT(49,Sr)}>$ and $<\sigma FI_{AT(49,Rc)}>$. Figure 4.10 illustrates how $<\sigma FI_{AT(49,Sr)}>$ and $<\sigma FI_{AT(49,Rc)}>$ evolve with the variation of *aa*. As it can be seen, there is a linear relationship between $<\sigma FI_{AT(49,Sr)}>$, $<\sigma FI_{AT(49,Rc)}>$ and *aa*, as expected due to the linearity of AT. From figure 4.10 it can also be highlighted that the evolution of $<\sigma FI_{TA,Sr}>$ is more important, which would mean that the $FI_{AT(49,Sr)}$ are more sensitive to DTs uncertainties than $FI_{AT(49,Rc)}$.

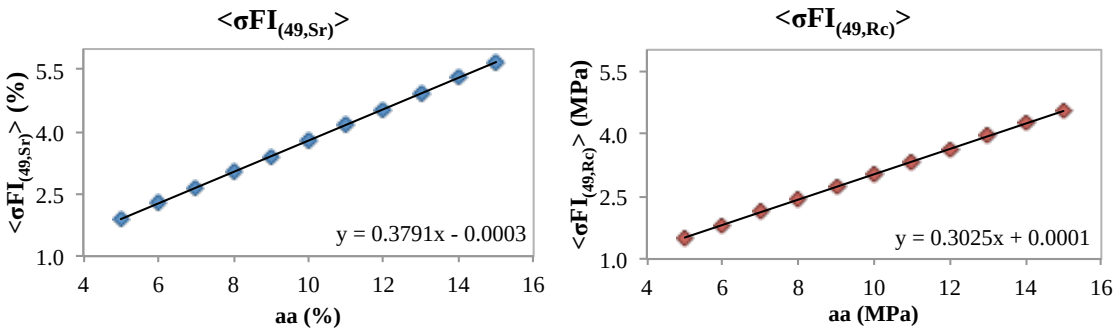

Figure 4-10. Evolution of $<\sigma FI_{AT(49,Sr)}>$, $<\sigma FI_{AT(49,Rc)}>$ as a function of *aa*.

4.5.4. Study of the influence of the number and values distribution of the DTIs

Until now, the estimation of $<\sigma FI_{AT(49,Sr)}>$ and $<\sigma FI_{AT(49,Rc)}>$ have been made with 7 cores, which were the ones extracted from a previous inspection. The interest of this section is to study the influence of a different number of cores selected differently in the propagation of the incertitude, hence, in the errors $<\sigma FI_{AT(49,Sr)}>$ and $<\sigma FI_{AT(49,Rc)}>$. That is interesting for the owner in order to be able to understand the uncertainties of the fusion process as a function of the number of cores, thus, as a function of the cost.

When the number of cores is changed, it is possible to obtain different $FI_{AT(N,j)}$ values as a function of the number of cores used to propagate the uncertainties. This difference is going to depend not only on the number of cores used, but also on their DTI values. For instance, in the case of 7 cores used, it is not the same to use only the cores that have Sr an Rc maximum and intermediary values leaving the minimum values out, or to use the cores that have only Sr an Rc intermediary values and so on. Hence, there are a determined number of possible combinations for each number of cores that we use. For our study on simulated data reference database of Marly's case, 49 possible locations can be used to extract a determined number of cores *n* for DT tests. Consequently, for instance, if we want to extract only 2 cores, 1 176 combinations would be possible to place the cores.

Therefore, to minimize the number of combinations used, only the combinations that includes maximums, minimums or intermediary values close to the mean are considered to have a true effect on $<\sigma FI_{AT(49,Sr)}>$ and $<\sigma FI_{AT(49,Rc)}>$ values. For this reason, an strategy to analyze the influence of the errors $<\sigma FI_{AT(49,Sr)}>$ and $<\sigma FI_{AT(49,Rc)}>$ on the number of cores *n* to be potentially extracted from Marly's bridge have been implemented. Figure 4.11 shows the flowchart of the strategy made in two stages. The first stage consist in taking a determined number *n* values from the DTI reference base for both indicators *j*, to create different configurations including minimum, maximum and intermediary values of both indicators (15 in total). Then, for each configuration of *n* DTI reference values, the introduction of uncertainties (aa_j) is made to finally obtain a mean standard deviation of the N values of FI_{AT}, ($<\sigma FI_{AT(49,j)}>$) hence 15 in total for

each indicator. Later, on the second stage, the best configuration between the 15 tested is chosen for both indicators by finding the smallest $<\sigma FI_{AT(49,j)}>$ value between the 15 found for the 15 tested configurations for both indicators and each *n*. Then, a variable number of *n* is taken from the DTI reference base using the best configuration found. The introduction of uncertainties is made for each *n* to finally obtain a $<\sigma FI_{AT(49,j)}>$ for each indicator and each *n*.

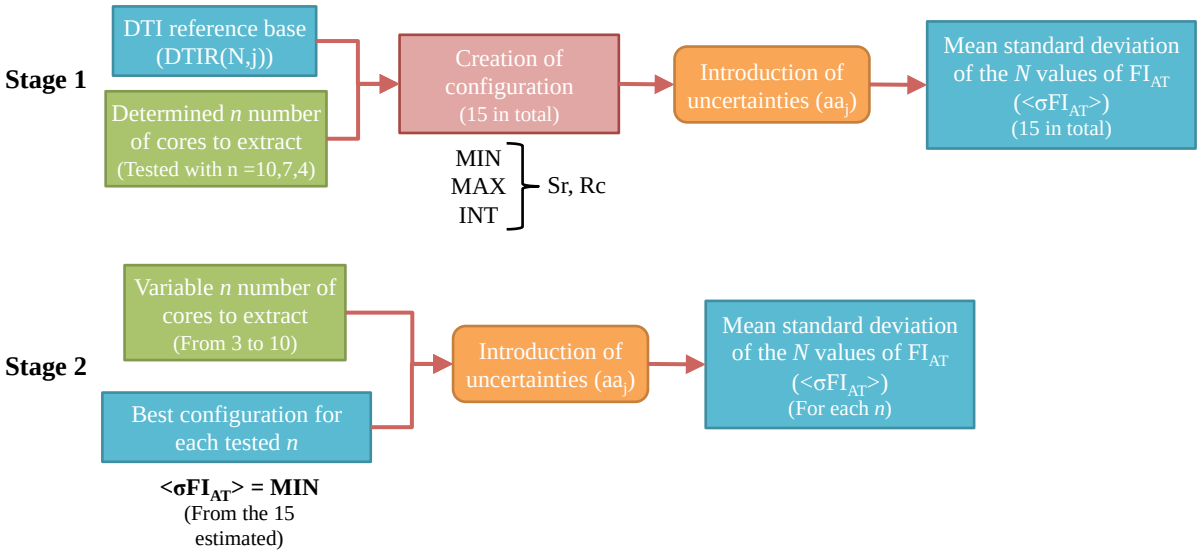

Figure 4-11. Flowchart of the two stages strategy.

4.5.4.1. Stage 1 : Choice of the best configuration

The steps explaining the detailed strategy are the following:

i) Use of the $DTI_{R(N,j)}$ reference base from figure 4.8 to choose 10, 7 or 4 DTI_R Sr and Rc values (number of cores *n* to be extracted), thus, three cases.

ii) Choice of 15 configurations to place *n* for the three different cases following the next criteria. First, the maximum, minimum and intermediary values close to the mean of Sr and Rc in $DTI_{R(N,j)}$ were located. Then, the configurations to place the *n* cores were chosen as shown in Table 4.2.

Table 4-2. Configurations to place *n* for the cases of 10, 7 and 4 cores to extract.

Configurations		1	2	3	4	5	6	7	8	9	10	11	12	13	14	15
Sr	Max	-	-	n	-	-	-	n/2	-	n/3	-	n/2	-	-	n/4	n/6
	Min	n	-	-	-	-	-	n/2	-	n/3	-	-	n/2	-	n/4	n/6
	Int	-	-	-	-	n	-	-	-	n/3	-	-	-	n/2	-	n/6
Rc	Max	-	-	-	n	-	-	-	n/2	-	n/3	n/2	-	-	n/4	n/6
	Min	-	n	-	-	-	-	-	n/2	-	n/3	-	n/2	-	n/4	n/6
	Int	-	-	-	-	-	n	-		-	n/3	-	-	n/2	-	n/6

It is possible that the minimum values of Sr are not located in the same positions as the minimum values of Rc. The same applies to the other configurations.

Figure 4.12 illustrates an example of the location of n = 10 with the configuration 1. The red line represents the 10th smallest value of Sr in the $DTI_{R(49,j)}$ reference base. The chosen positions are highlighted in green for both indicators.

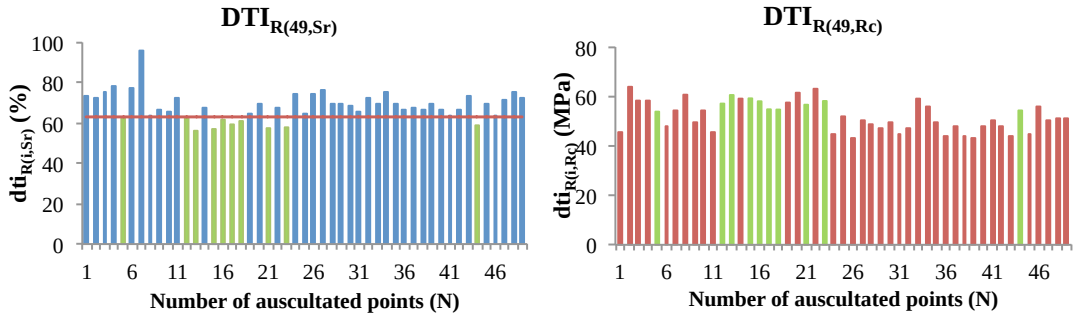

Figure 4-12. Example of the location of Sr and Rc for of n = 10 with the configuration 1 including the 10 smallest values of Sr.

iii) Introduction of the uncertainties (aa_{Sr} = 10% and aa_{Rc} = 5 MPa) on the chosen n $dti_{R(i,j)}$ values from $DTI_{R(49,j)}$ reference base for each case and configuration. Table 4.3 shows the $<\sigma FI_{AT(49,Sr)}>$ and $<\sigma FI_{AT(49,Rc)}>$ values obtained for each configuration, for the cases n = 10, 7 and 4 respectively after the introduction of the uncertainties.

Table 4-3. $<\sigma FI_{AT(49,Sr)}>$ and $<\sigma FI_{AT(49,Rc)}>$ values for the 15 configurations and n = 10, 7 and 4.

	***n* = 10**		***n* = 7**		***n* = 4**	
Configuration	**<σFI(49,Sr)> (%)**	**<σFI(49,Rc)> (MPa)**	**<σFI(49,Sr)> (%)**	**<σFI(49,Rc)> (MPa)**	**<σFI(49,Sr)> (%)**	**<σFI(49,Rc)> (MPa)**
1	4.86	3.07	6.30	3.69	13.23	8.24
2	3.59	4.35	4.43	5.68	5.80	8.18
3	2.69	1.37	3.75	1.81	5.26	2.22
4	2.52	2.53	3.22	3.48	5.40	8.28
5	2.04	1.21	2.40	1.44	3.39	2.17
6	2.13	1.32	2.51	1.51	4.66	3.30
7	2.02	1.22	2.37	1.46	3.15	1.96
8	**1.97**	**1.12**	**2.33**	**1.29**	**3.08**	**1.69**
9	2.04	1.26	2.42	1.47	3.19	1.78
10	2.03	1.20	2.42	1.42	3.23	1.94
11	2.12	1.22	2.56	1.42	4.05	2.56
12	2.16	1.37	2.72	1.79	3.23	1.82
13	2.32	1.61	3.02	2.13	5.05	3.95
14	2.00	1.22	2.39	1.36	3.23	1.78
15	2.05	1.18	2.43	1.38	3.42	2.30

iv) *Choice of the best configuration:* The best configuration is chosen by selecting the smallest values of $<\sigma FI_{AT(49,Sr)}>$ and $<\sigma FI_{AT(49,Rc)}>$ between all the 15 configurations. As illustrated in tables 4.3, for all 3 cases (n = 10, 7 and 4), the smallest values of both

$<\sigma FI_{AT(49,Sr)}>$ and $<\sigma FI_{AT(49,Rc)}>$ are the ones from the configuration 8, which includes the maximum an minimum values of Rc.

The coincidence that the minimum value of $<\sigma FI_{AT(49,Sr)}>$ and $<\sigma FI_{AT(49,Rc)}>$ are found exactly in the same configuration, lead us to think that there may be a relationship between $<\sigma FI_{AT(49,Sr)}>$ and $<\sigma FI_{AT(49,Rc)}>$. Figure 4.13a-c, shows $<\sigma FI_{AT(49,Sr)}>$ in function of $<\sigma FI_{AT(49,Rc)}>$ for the 15 configurations for the 3 cases. As it can be seen, a tendency of power form was found (R^2 between 0.69 and 0.75). Moreover, when the number of cores decreases, the correlation between $<\sigma FI_{AT(49,Sr)}>$ and $<\sigma FI_{AT(49,Rc)}>$ also decreases.

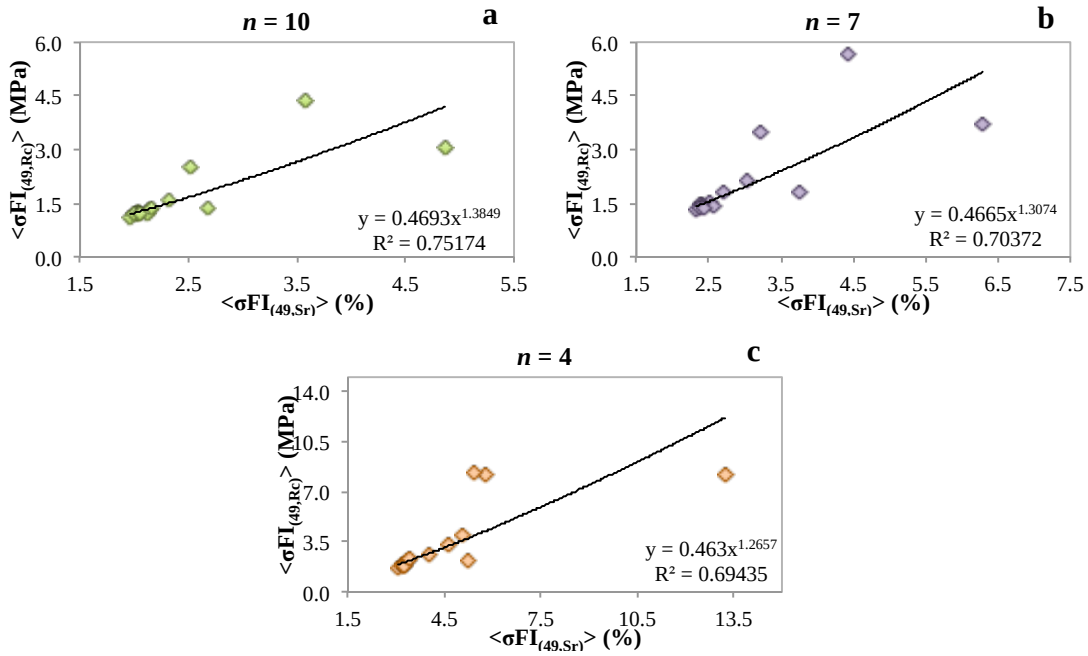

Figure 4-13. $<\sigma FI_{AT(49,Sr)}>$ in function of and $<\sigma FI_{AT(49,Rc)}>$ for the 15 configurations for the case: a) n = 10, b) n = 7 and c) n = 4.

4.5.4.2. Stage 2: Analysis of the chosen configuration

In the previous section, it was found that for the Marly's bridge study, the best configuration to study the influence of the errors on the number of cores to be extracted is the configuration 8, which includes the maximums and minimums of Rc. Therefore, if we vary the number of cores using this configuration, it is possible to obtain a relationship between the error $<\sigma FI_{AT(49,Sr)}>$ and $<\sigma FI_{AT(49,Rc)}>$ for both indicators and the number of cores to extract n. Figure 4.14 shows this relationship including the bars of errors for $<\sigma FI_{AT(49,Sr)}>$ and $<\sigma FI_{AT(49,Rc)}>$ for each n, which represents the standard deviation for $<\sigma FI_{AT(49,Sr)}>$ and $<\sigma FI_{AT(49,Rc)}>$ from all the 49 auscultated points. As it can be seen, as n increases, $<\sigma FI_{AT(49,Sr)}>$ and $<\sigma FI_{AT(49,Rc)}>$ decreases. For both indicators (Rc and Sr), it was found a power relationship, and from figure 4.14 it can also be seen that if we increase the number of cores n from 3 to 10, the error $<\sigma FI_{AT(49,Sr)}>$ decreases by 52% for Sr, and the error $<\sigma FI_{AT(49,Rc)}>$ decreases by 47% for Rc.

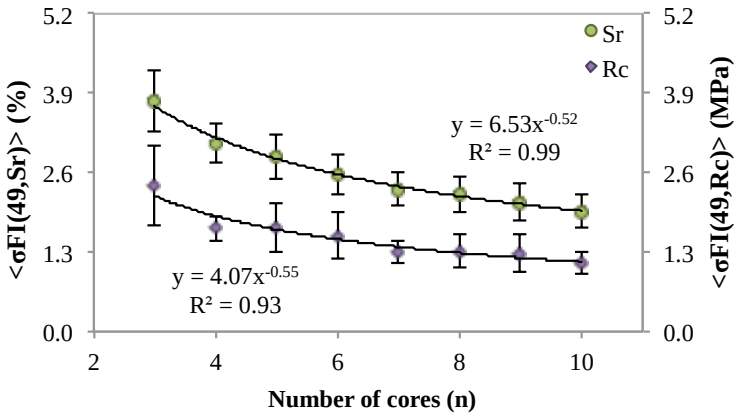

Figure 4-14. $<\sigma FI_{AT(49,Sr)}>$ and $<\sigma FI_{AT(49,Rc)}>$ in function of *n*.

From figure 4.14 if we compare $<\sigma FI_{AT(49,Sr)}>$ and $<\sigma FI_{AT(49,Rc)}>$ it can be inferred that the error for Rc is smaller than the error for Sr by 1% approximately in average. It can also be inferred from this figure that if we make a sum of the variances of $<\sigma FI_{AT(49,Sr)}>$, $<\sigma FI_{AT(49,Rc)}>$ $<<\sigma FI_{AT(49,Sr)}>>$ and $<<\sigma FI_{AT(49,Rc)}>>$ for each indicator respectively, it can be deduced that each $FI_{AT(N,j)}$ value can vary from 2% to 3.8% for Sr, and from 1.1 MPa to 2.47 MPa for Rc in average if we reduce the number of cores from 10 to 3. Moreover, if we search for a relationship between $<\sigma FI_{AT(49,Sr)}>$ and $<\sigma FI_{AT(49,Rc)}>$ in this case, which is the variation of *n* for the same configuration (figure 4.15), a better relationship of exponential form (R^2 = 0.96) is found confirming that the errors of Sr and Rc may be related.

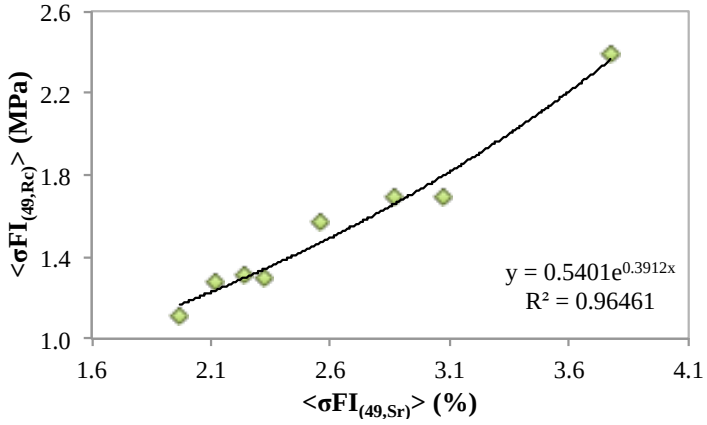

Figure 4-15. Relationship between $<\sigma FI_{AT(49,Sr)}>$ and $<\sigma FI_{AT(49,Rc)}>$. Case of the variation of *n* for the chosen configuration.

4.6. Conclusions

In this chapter, a proposal of the introduction of the uncertainties representing the variability of indicators obtained by destructive tests of the studied material of a studied concrete structure is made. The propagation of these uncertainties to the indicators obtained by fusion is made through

the updating by affine transformation, which assumes a linear relationship between the indicators obtained by destructive test and the indicators obtained by the fusion process.

This contribution offers to the structure manager additional entry information for the indicators prediction models. This additional information is the precision (standard deviation and statistical distribution) of the indicators obtained by the fusion of NDT methods for each auscultation point of the studied structure, as well as the sensitivity of this precision to the number and selection of cores. Hence, it is possible to offer to the structure manager a number of cores to extract as well as their position for a given indicator uncertainty. The method used to obtain this variation can be applied to any concrete structure.

Here, the case study concerns three piles (S, ZBL and Sadam) of a bridge located in Marly – France. Two indicators were chosen for this study: Saturation degree (Sr) and Compressive strength (Rc). Seven DT indicator results of Sr and Rc, obtained from the extraction of seven cores made in a previous auscultation. Moreover, 49 measurements of Impact Echo dynamic modulus (IEE), Capacitive Large Electrodes Permittivity (CLEP) and GPR Direct Wave Velocity (DWV) from the three auscultated bridge piles were chosen to estimate the fused indicator values of Sr and Rc for each auscultated point, for the DT uncertainty study. The main conclusions are the following:

- Finding a predictable linear relationship between the mean standard deviations $<\sigma FI_{TA,Sr}>$, $<\sigma FI_{TA,Rc}>$ and *aa*, it could be observed that the increase of $<\sigma FI_{TA,Sr}>$ is more important compared to $<\sigma FI_{TA,Rc}>$. This means that the indicator results for saturation degree are more sensitive to DTs uncertainties than the compressive strength.

- A study of the influence of the number and values distribution of the DTIs selected from extracted cores on the error $\sigma FI_{AT(i,,j)}$ was developed for the case study. A DT reference base was estimated using the affine transformation. Three cases of 10, 7 and 4 cores with 15 different configurations including maximum, minimum and intermediary values were tested. The chosen configuration for this study was the one containing maximum and minimum values of Rc, which includes the location of the first $n/2$ highest and $n/2$ smallest values of Rc in $DTI_{R(N,j)}$. This configuration had the smallest values of $<\sigma FI_{TA,Sr}>$ and $<\sigma FI_{TA,Rc}>$ between all the 15 configurations. This confirms that the best configuration belongs to the indicator that has more variability throughout the studied structure (important difference between max and min) for fused and DT indicators values, which at the same time are correlated. Moreover, a relationship of power form between $<\sigma FI_{TA,Sr}>$ and $<\sigma FI_{TA,Rc}>$ values found for the 15 configurations was found for each *n* case.

- For the chosen configuration, we varied the number of cores *n*. For this case study it was found that as *n* increases, the errors $<\sigma FI_{TA,Sr}>$ and $<\sigma FI_{TA,Rc}>$ decreases. Moreover, it was obtained a power form relationship between the error ($<\sigma FI_{TA,Sr}>$ and $<\sigma FI_{TA,Rc}>$) for both indicators and the number of cores to extract *n.* For Sr, $<\sigma FI_{TA,Sr}>$ decreases by 52% if we pass from 3 to 10 number of cores. Even though, for Rc, $<\sigma FI_{TA,Rc}>$ decreases only by 47%.

- An exponential relationship between $<\sigma FI_{TA,Sr}>$ and $<\sigma FI_{TA,Rc}>$, which is the variation of the number of cores for the best configuration was found confirming that the errors of Sr and Rc may be related.

References

[1] Garnier, V. et al., Rapport Final Projet C2D2-ACDC, March 2014.

[2] Garnier, V., Martini, D., Balayssac, J.P., Sbartai, Z.M., Villain, G., Piwakowski, B., Salin, J., Fardeau. V., “Analysis and Capitalisation for the Diagnosis of Constructions : Méthodologie de transfert d’essais non destructifs du laboratoire vers le site”, 12th Congrès Français de Mécanique, Bordeaux, 2013.

[3] Martini, D., Garnier, V., Ploix, M.A., “Evaluation of an intrinsic error estimator for the data fusion of NDT techniques used to identify the material and damage properties of concrete structures”, 6th workshop on structural health monitoring, Dresden, 2012.

CHAPTER 5

ARTIFICIAL NEURAL NETWORK APPLIED FOR THE PREDICTION OF CONCRETE PERFORMANCE AND DURABILITY INDICATORS

5.1. Introduction

As the data fusion by theory of possibilities has shown to be reliable and consecutively has been used in different French projects to determine different indicators from measured observables, it has an important limitation, which is that there must be a linear correlation between the target indicators and the measured observables for being able to apply the method. Therefore, as the Artificial Neural Network (ANN) has different advantages as its simple and inexpensive application, as well as it does not need a linear correlation between the target indicators and the measured observables like the data fusion method, it also has shown to be effective on inversion applications on concrete [1-2]. For this reason, ANN was tested and its performance has been evaluated in this chapter as an alternative NDT combination method.

This chapter shows the capacity of ANN for the prediction of four concrete indicators: water content (w), porosity (P) compressive strength (Rc) and carbonation depth (Pc). It is presented in this chapter, the model optimization procedure: selection of the network architecture, modification of the number of neurons in the hidden layer and, input and output information. The development of the neural models has been made with the Matlab toolbox "Neural Network". This toolbox has different advantages as the definition of simple architectures, the choice of transfer functions, the choice of optimization algorithms, etc.

Each selected model was tested using a multilayer perceptron (MLP) and the optimization of the learning process was made by crossed validation of the Mean Square Error (MSE) (equation 5.1) between the target values (V_T) and the predicted values (V_P) of the learning and validation base. The algorithms used to train the MPLs were whether the Levenberg-Maquardt (LM) or the Scaled Conjugate Gradient (SCG). Other important criterion to stop the learning process for this study was the coefficient of determination (R^2), which minimum value was selected according to the training performance of each MPL.

$$MSE = \frac{1}{N}\sum_{i=1}^{N}(V_T - V_P)^2 \tag{5.1}$$

The performance of the different ANN models for each targeted indicator (w, P, Rc and Pc) was first tested with the SENSO database. Later, an application of the selected ANN models for w, P and Rc was made on a wall of Le-Havre site. Finally, a comparison between the performance of the ANN and the data fusion is made using the results of w, P and Rc obtained with both methods for Le-Havre thermal power plant, clarifying that the data fusion results are the ones obtain from the raw data fusion process (without updating).

5.2. Database used for the implementation of neural models of w, P and Rc

The database used for the creation of the different ANNs is the laboratory based SENSO database. This database, which is the same used for the creation of multi-linear correlation laws that relate one observable with a pair of indicators and, which are used for the data fusion process (see chapter 2) is composed of 222 samples of 9 different concretes: G1, G2, G3, G3a, G4, G5, G6, G7, G8, hence, different porosities. The composition of each concrete is shown in table 5.1. The samples of each concrete are also at different saturation degrees: 0 %, 40 %, 60 %, 80 % and 100 %.

Table 5-1. Composition of the SENSO concretes G1, G2, G3, G3a, G4, G5, G6, G7, G8 [3].

	G1	G2	G3	G3a	G7	G8	G4	G5	G6
Type de granulats	SR 14	SR 14	SR 14	SR 14	SR 14	SR 14	SR 22	SC 14	CC 14
Ciment CEM I 52,5 N Calcia	405	420	370	370	320	240	370	370	370
Fumée de silice	45								
Fluidifiant (Glenium 27)	1.5 % (*)								
Sable 0/4	710	738	774	774	839	938	660	760	758
Gravier 4-14	1065	1062	1069	1069	1047	1016	415	1090	1138
Gravier 4-22							750		
Eau totale	140	197	212	212	216	217	212	212	214
E/C	0,31	0,47	0,57	0,57	0,68	0,90	0,57	0,57	0,58

Seventeen observables (table 2.11) were measured on the different samples; hence, countless input configurations are possible to estimate the different targeted indicators (w, P and Rc). However, only seven observables are used to form the different tested input configurations, as they are considered to be the most relevant to estimate the targeted indicators. These observables were chosen based on tests from previous studies, which objective was to assess the same indicators, but with the fusion data tool described in chapter 2. These studies did not only consider the sensitivity of each observable to the targeted indicators, but also which and how many observables must be combined to obtain the most accurate estimation of a pair of targeted indicators. Table 5.2 shows the different observables used for this study.

Table 5-2. Observables used on the tested MPL models configurations for the estimation of w, P and Rc.

Number	***Observable***
4	Surface Ultrasound - Wave velocity 3 cm (m/s)
5	Ultrasound Pulse - 250kHz transmission velocity (m/s)
7	Impact Echo - Dynamic modulus of Young (GPa)
8	Impact Echo - Compressive waves velocity (m/s)
9	Capacity of large electrodes - Permittivity
11	Log of the quadripole resistivity 5 cm

The ANN bases for the 3 targeted indicators were composed choosing samples of the SENSO database randomly as following:

- Training base: 70 % of the SENSO database samples. Hence, 156 samples.
- Validation base: 15 % of the SENSO database samples. Hence, 33 samples.
- Test base: 15 % of the SENSO database samples. Hence, 33 samples.

5.3. General architecture of the adopted neural models

A Multi-Layer Perceptron (MPL) composed of one input layer, one hidden layer with an optimized number of neurons has been selected for the estimation of the targeted indicators: w, P, Rc and Pc. The number of inputs for the input layer of each MPL model is defined by the different tested configurations showed in the following sections. The tested configurations were also chosen based on tests from previous indicators assessment made with the fusion data tool described in chapter 2, and which results showed to be accurate.

As it was mentioned in chapter 2, different transfer/activation functions linear or not can be applied to make a transformation for the added values of the hidden and output layer. In the case of this study, the tan-sigmoid function was used as the transfer function for the hidden layer and the linear function was used for the output layer. Table 5.3 shows the forms and equations for the used transfer functions.

Table 5-3. Forms and equations of the tan-sigmoid and the linear transfer functions.

Name	***Equation***	***Form***
Linear	f (S) = S	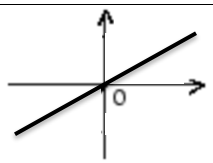
Hyperbolic tangent	$f(S) = \frac{e^{S} - e^{-S}}{e^{S} + e^{-S}}$	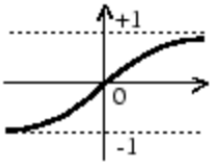

5.4. Neuronal model for the prediction of water content

5.4.1. Selected architecture

Figure 5.1 and Table 5.4 show the optimized architecture and the tested input configurations of the MPL model for the estimation of w (MLP-w).

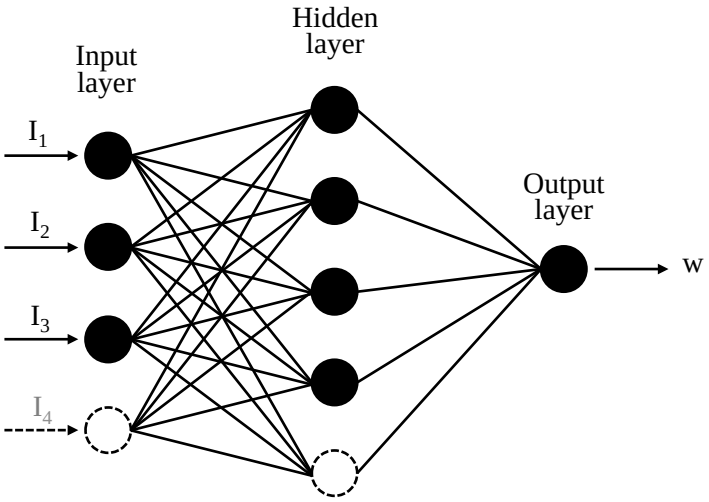

Figure 5-1. Architecture of MLP-w.

Table 5-4. Tested input configurations for the estimation of w.

Input observables configurations
4 5 7
4 5 9
5 7 9
5 8 9
5 9 11
5 9 14
7 9 11
4 7 9 11
4 8 9 11
5 7 9 11
6 8 9 11

For each tested input configuration several tests were made to obtain the optimal number of neurons in the hidden layer. The variable chosen to optimize the number of neurons was the Mean Square Error (MSE) (Eq. 1). Figure 5.2 shows the performances of the MLP-w of the best 5 tested input configurations (smallest MSE) for the training, validation and test base.

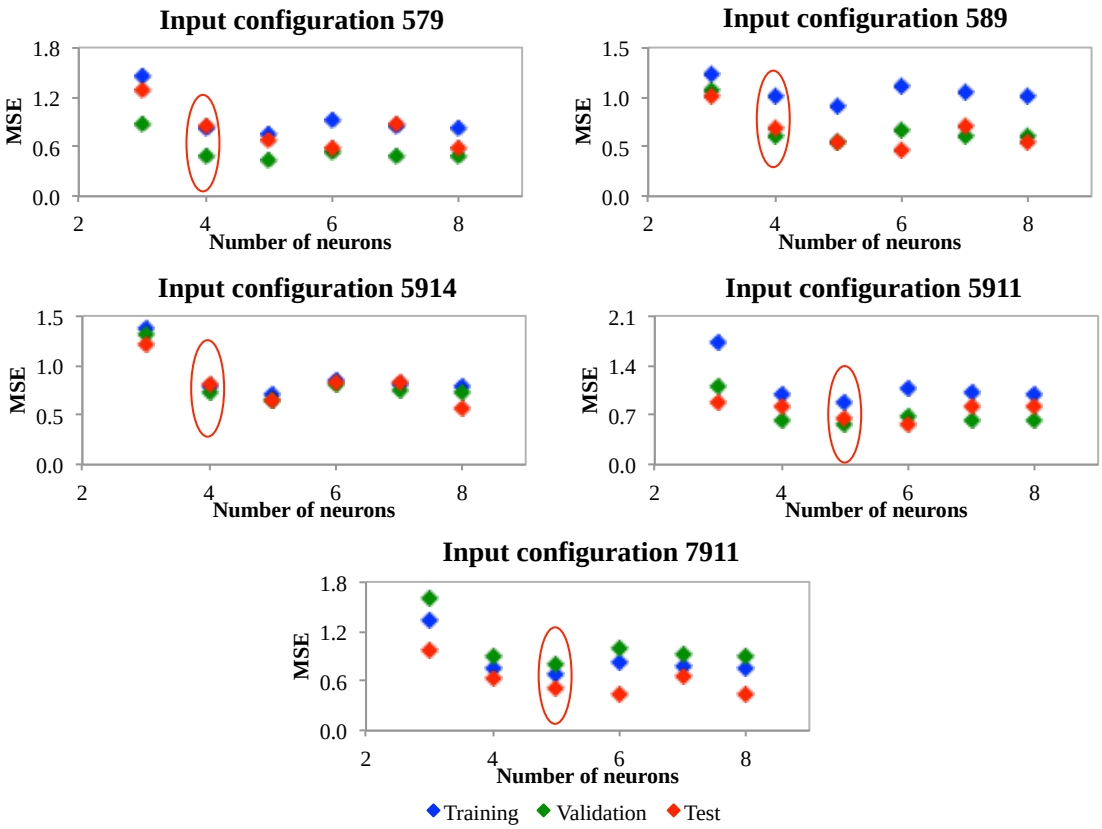

Figure 5-2. Performances of the MLP-w of the best 5 tested input configurations for the training, validation and test base.

As it can be observed, the stabilization of the MSE is between 4 or 5 neurons for all five input configurations. We retain then, 4 neurons in the hidden layer for the configurations 579, 589 and 5914 and, 5 neurons in the hidden layer for the configurations 5911 and 7911.

5.4.2. Results on SENSO base and choice of the best configuration

Each one of the 5 MLP-w bases was trained with the optimal number of neurons in the hidden layer found in the previous section. The learning algorithm used was the Levenberg-Maquardt due to its simplicity, reduced calculation time, and satisfying results. The minimum value of R^2 used to stop the training process was 0.9.

Figure 5.3 shows the learning optimization process for the 5 MLP-w. As it can be seen the MSE vary from 0.76 $\%^2$ to 1.02 $\%^2$ for the training base and, from 0.48 $\%^2$ to 0.9 $\%^2$ for the validation base. Besides, the R^2 is of 0.99 on average for the three bases of all MLP-w.

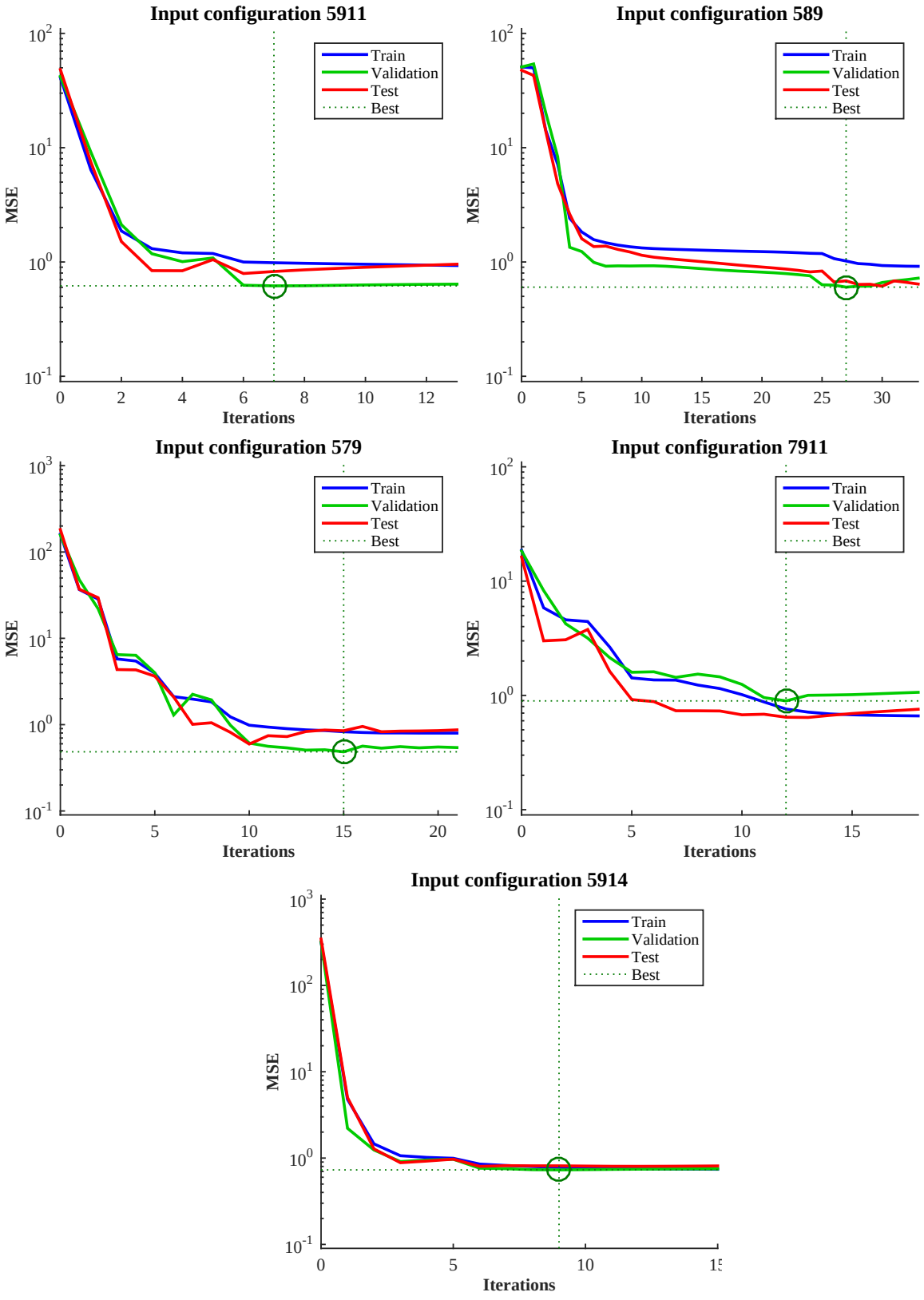

Figure 5-3. Training optimization process for the 5 MLP-w studied.

To choose the best MLP-w between the 5 studied, an Absolute Mean Error (AME) (equation 5.2) was calculated, between the target w values of the SENSO base and the estimated values. Figure 5.4 shows the AME for the 5 MLP-w. As it can be seen, the AME varies between 0.5 %

and 0.7 %. Hence, the best MLP-w is the one that has the minimum AME among the others. In this case, it belongs to the MLP-w obtained with the input configuration 579.

$$AME = \frac{1}{N}\sum_{i=1}^{N}|V_T - V_P| \quad (5.2)$$

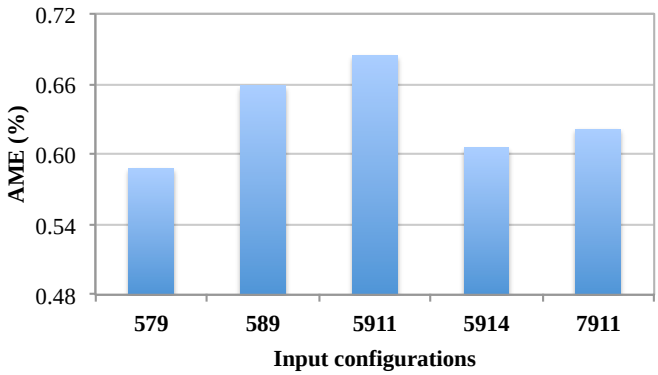

Figure 5-4. Absolute mean error for the results of the 5 MLP-w studied.

Figure 5.5 shows the correlations between the predicted and measured water content values for the training, validation and test bases of MLP-w for the configuration 579. For the training base composed of 156 samples, the correlation is quite good as the MSE is inferior to 1 % and the R^2 is equal to 0.99. For the test and validation base, composed of 33 samples, the correlations also showed to be good as the MSE are inferior to 0.5 % and 1 % respectively and both R^2 are over 0.98. Consequently, these results confirm the quality of the chosen MLP-w.

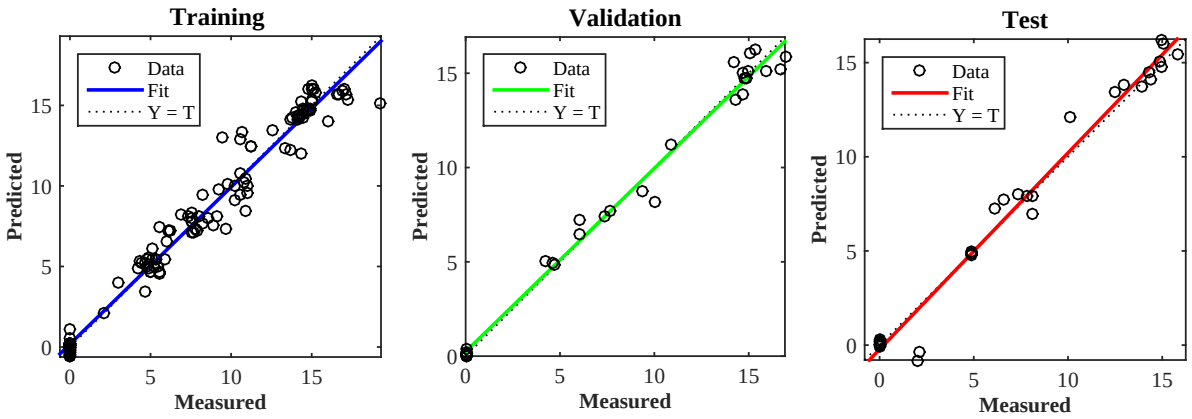

Figure 5-5. Correlations between the predicted and measured water content values for the training, validation and test bases of MLP-w for the configuration 579.

5.5. Neuronal model for the prediction of porosity

5.5.1 Selected architecture

Figure 5.6 and Table 5.5 show the optimized architecture and the tested input configurations of the MPL model for the estimation of P (MLP-P).

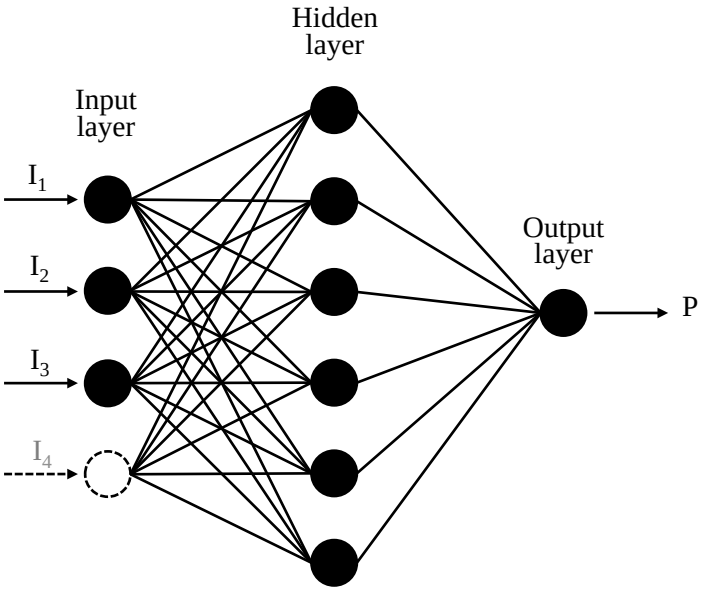

Figure 5-6. Architecture of MLP-P.

Table 5-5. Tested input configurations for the estimation of P.

Input observables configurations
5 7 9
5 9 11
7 9 11
4 8 9 11
6 7 9 11

Figure 5.7 shows the performances of the MLP-P of the best 2 tested input configurations (smallest MSE) for the training, validation and test base.

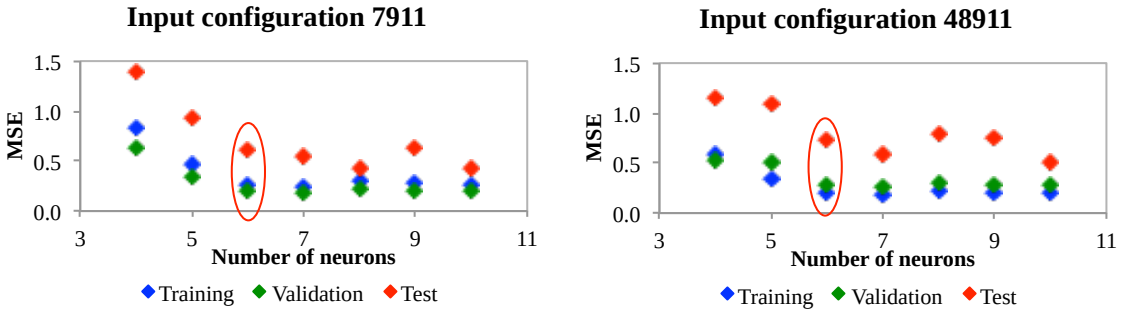

Figure 5-7. Performances of the MLP-P of the best 2 tested input configurations for the training, validation and test base.

As it can be observed, the stabilization of the MSE is between starts at 6 neurons for both input configurations. Thus, we retain 6 neurons in the hidden layer for both configurations. Contrary to the water content case, it was very difficult to find input configurations that could gave results with an acceptable MSE, which is a sign that calibration will be necessary for another set of data.

5.5.2. Results on SENSO base and choice of the best configuration

Each MLP-P was trained with the optimal number of neurons in the hidden layer found in the previous section. The learning algorithm used was also the Levenberg-Maquardt due to its acceptable results. Contrary to the water content case, not all the bases of the tested configuration had a R^2 value more important than 0.9. Hence, the learning process stopped when two of the three bases had a value of at least 0.9 and the other one a R^2 value of at least 0.8.

Figure 5.8 shows the learning optimization process for both MLP-P. As it can be seen the MSE is 0.24 $\%^2$ in average for the training and validation bases of both MLP-P. Besides, the R^2 is over 0.9 for the training and validation bases of both MLP_P.

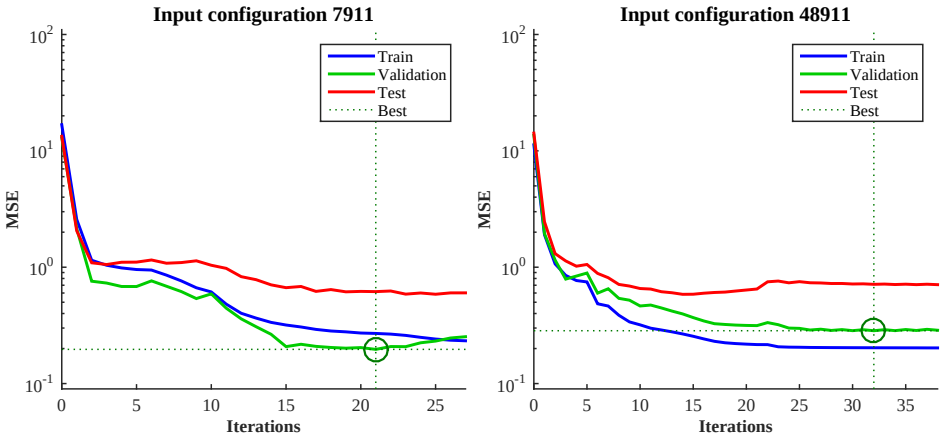

Figure 5-8. Training optimization process for both MLP-P studied.

To choose the best MLP-P, the Absolute Mean Error was calculated between the P measured values of the SENSO base and the P estimated values. Figure 5.9 shows the AME for both MLP-P. As it can be seen, the AME was 0.37 % for the 48911 configuration, and 0.42 % for the 7911 configuration. Both AME are acceptable. Besides, if the measurements of the 4 observables are not available, the input configuration 7911 can also be used.

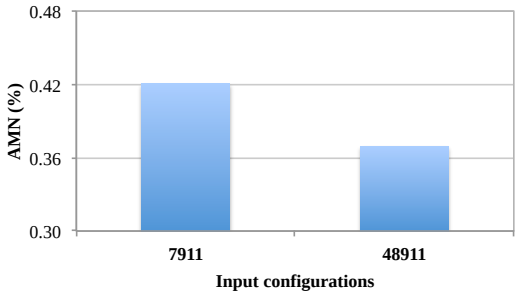

Figure 5-9. Absolute mean error for the results of both MLP-P studied.

Figure 5.10 shows the correlations between the predicted and measured porosity values for the training, validation and test bases of MLP-P for both configurations. For the training base

composed of 156 samples, the correlation is quite good as the MSE is inferior to 1 % and the R^2 is over 0.9 for both MPL-P. For the validation base, composed of 33 samples, the correlations also showed to be good as the MSE are inferior to 0.3 % and the R^2 are over 0.9 for both MPL-P. As for the test base, an acceptable correlation is found with a MSE inferior to 0.8 % and a R^2 over 0.8.

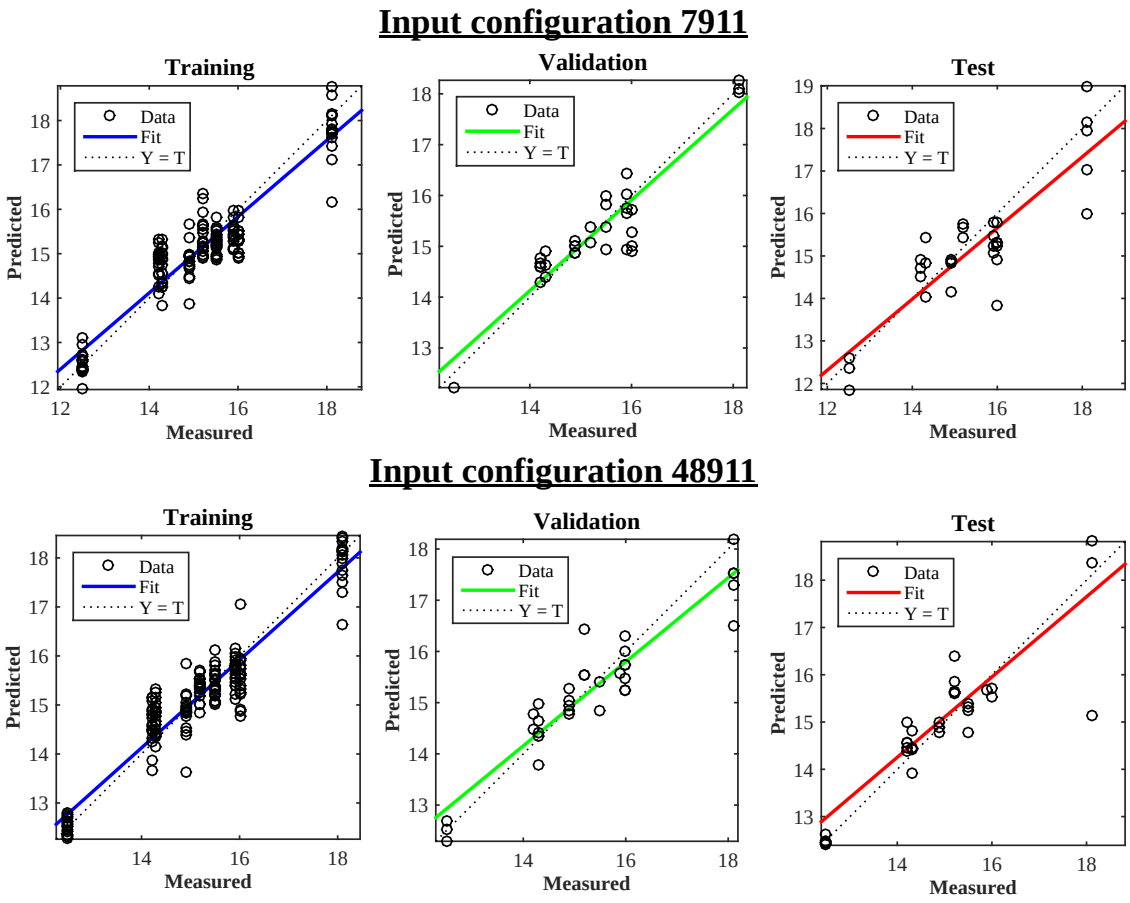

Figure 5-10. Correlations between the predicted and measured water content values for the training, validation and test bases of the MLP-P models for the input configurations 48911 and 7911.

5.6. Neuronal model for the prediction of compressive strength

5.6.1. Selected Architecture

Figure 5.11 and Table 5.6 show the optimized architecture and the tested input configurations of the MPL model for the estimation of Rc (MLP-Rc).

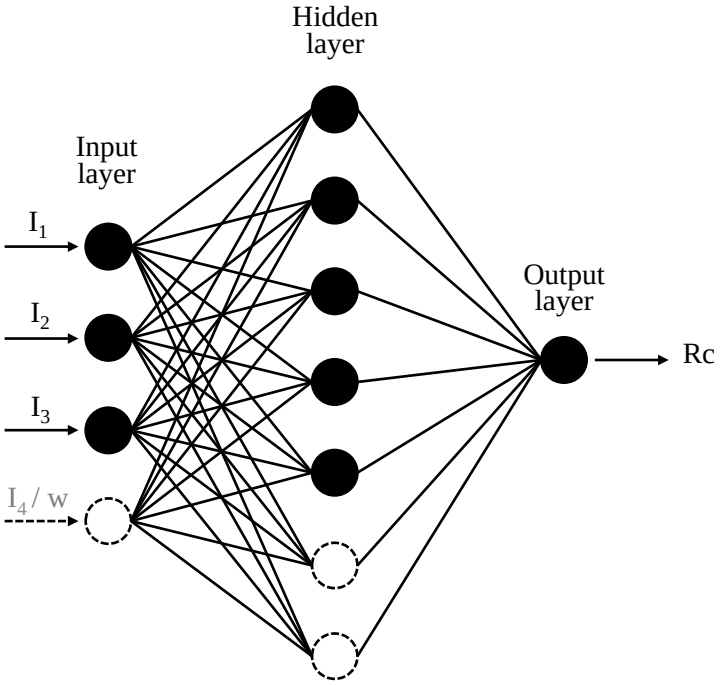

Figure 5-11. Architecture of MLP-Rc.

Table 5-6. Tested input configurations for the estimation of Rc.

Input observables configurations
4 5 7
5 7 9
5 9 11
7 9 11
8 9 11
4 8 9 11
5 7 9 11
6 8 9 11

Figure 5.12 shows the performances of the MLP-Rc of the best 3 tested input configurations (smallest MSE) for the training, validation and test base.

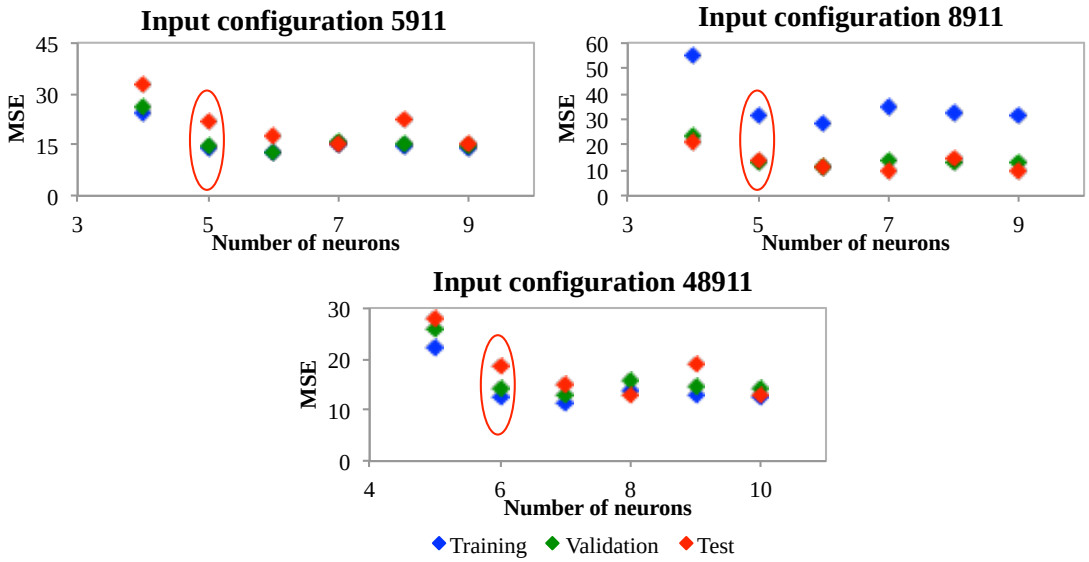

Figure 5-12. Performances of the MLP-Rc of the best 3 tested input configurations for the training, validation and test bases.

As it can be observed, the stabilization of the MSE is between 5 and 6 neurons for the three input configurations. We retain then, 5 neurons in the hidden layer for configurations 5911 and 8911, and 6 neurons in the hidden layer for the 48911 configuration. Contrary to the water content case, it was very difficult to find input configurations that could gave an acceptable MSE, as for the training, validation and test bases its value is between 15 and 19 MPa^2 for the 3 configurations. Therefore, other configurations were tested using also the water content values estimated with the MPL-w described above as an input. The chosen one was the 5911w with 7 neurons in the hidden layer, which had the smaller value of MSE (9.8 MPa^2) in average for the three bases (training, validation and test).

5.6.2. Results on SENSO base

The chosen MLP-Rc was trained using also the learning algorithm Levenberg-Maquardt due to its acceptable results. The criteria to stop the learning process was, as mentioned above, the crossed validation of both bases (validation and training) by the minimization of MSE. As the water content and porosity cases, R^2 was also used to stop the learning process. The learning process stopped when the value was at least 0.9 for the three bases.

Figure 5.13 shows the training optimization process for the chosen MLP-Rc. As it can be seen the MSE is below 10 MPa^2 for the training and validation bases and, over 10 MPa^2 for the test base. Besides, the R^2 is of 0.99 on average for all MLP-Rc bases and the estimated AME between the Rc measured values of the SENSO base and the Rc estimated values are 2.1 MPa, which is an acceptable approximation.

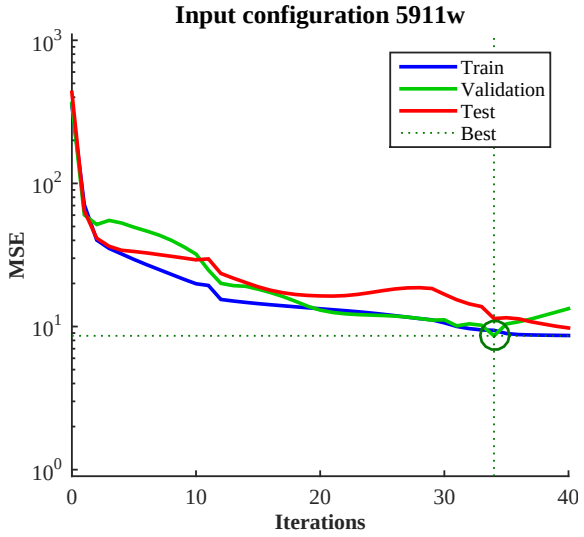

Figure 5-13. Training optimization process for the chosen MLP-Rc studied.

Figure 5.14 shows the correlations between the predicted and measured compressive strength values for the training, validation and test bases of MLP-Rc for the configuration 5912w. For the training base composed of 156 samples, the correlation is not bad as the MSE is inferior to 10 MPa and the R^2 is equal to 0.96. For the validation base, composed of 33 samples, the correlation also showed to be acceptable as the MSE is also below 10 MPa and the R^2 is 0.98. Finally, for the test base, composed of 33 samples, the correlations also showed to be correct as the MSE are inferior to 12 MPa^2 and R^2 is 0.96.

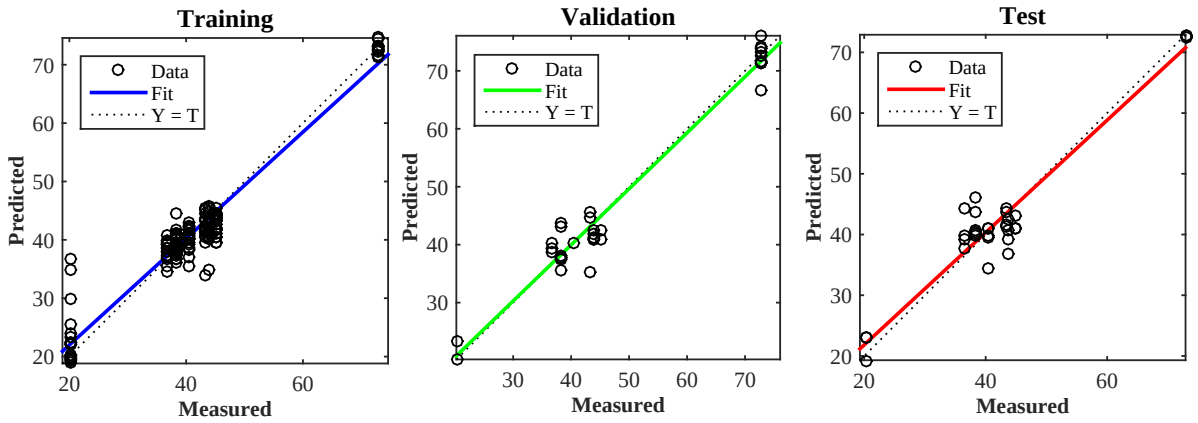

Figure 5-14. Correlations between the predicted and measured water content values for the training, validation and test bases of MLP-Rc for the configuration 5911w.

5.7. Neuronal model for the prediction of carbonation depth

5.7.1. Database used for the creation of neural models of Pc

The database used for the creation of the different ANN models is composed of two laboratory based databases: EVADEOS and SENSO-Pc. The EVADEOS base is composed of 24 samples of one kind of concrete: C1 that has the same composition as the concrete G8 of the

SENSO base (see table 5.1). The different samples of each concrete are also at two different saturation degrees: 50% and 100 % and different carbonation depths. Besides the EVADEOS database also includes 23 samples of a wall made with the same concrete C1, a saturation degree of 60 % in average, three different carbonation depths and two different faces: one with steel reinforcement and one without. Finally, from the SENSO-Pc database, 16 samples of concretes G3, G3a, G7 and G8 (see table 5.1) completely saturated and with different carbonation depths were also incorporated.

Seventeen observables (table 2.11) were measured on the different samples. Hence, countless input configurations are possible to estimate the targeted indicator: carbonation depth (Pc). The difficulty with this indicator is that only some of the measured observables are barely sensitive to Pc compared with their respective notable sensitivities to w, Rc or P. A careful study during the EVADEOS project was made to choose the pertinent observables sensitive to Pc that can be combined to obtain acceptable estimated values of Pc. Thus, only six observables were used together, as they are considered to be the most relevant to estimate the Pc. The results presented below use the 6 observables together as an only input configuration. Other configurations were tested using less number of observables, but the best training performance was obtained using the 6 observables as an input configuration. Table 5.7 shows the 6 observables used for this study.

Table 5-7. Observables used on the tested MPL for the estimation of Pc.

Number	***Observable***
4	Surface Ultrasound - Wave velocity 3 cm (m/s)
5	Ultrasound Pulse - 250kHz transmission velocity (m/s)
9	Capacity of large electrodes - Permittivity
11	Log of the quadripole resistivity 5 cm
14	GPR pic to pic amplitude
16	Direct wave GPR velocity (cm/s)

The ANN bases for the targeted indicator were composed choosing samples of the SENSO database randomly as follows:

- Training base: 70 % of the SENSO database samples. Hence, 45 samples.
- Validation base: 15 % of the SENSO database samples. Hence, 10 samples.
- Test base: 15 % of the SENSO database samples. Hence, 10 samples.

5.7.2. Selected architecture

Figure 5.15 shows the optimized architecture and the tested input configurations of the MPL model for the estimation of Pc (MLP-Pc).

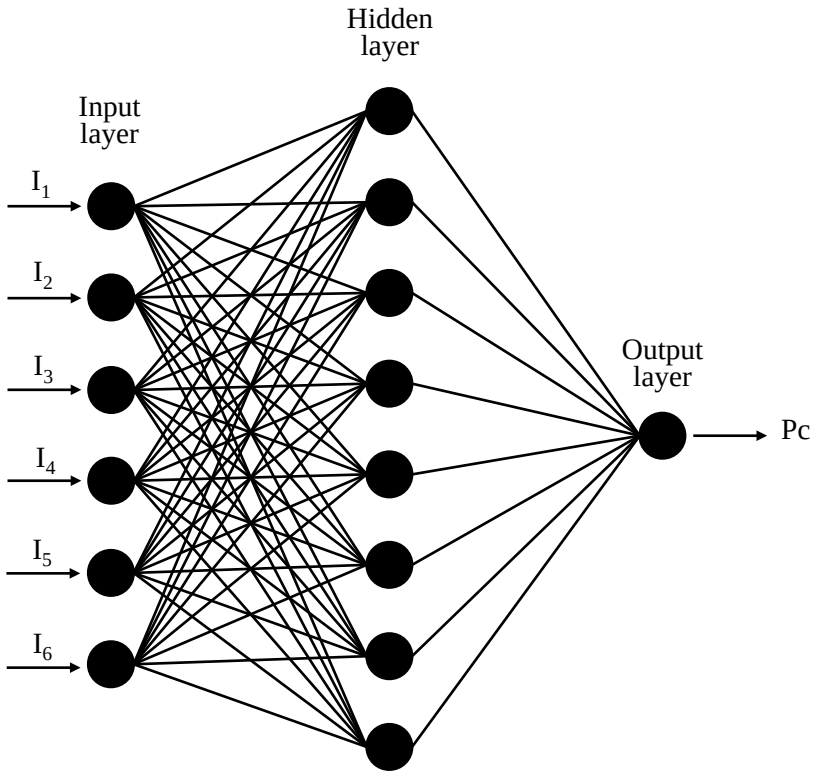

Figure 5-15. Architecture of MLP-Pc.

The transfer functions used for the tested MPL-Pc are the same as the ones used for the previous MPL indicators cases: tan-sigmoid for the hidden layer and linear for the output layer.

The learning process was made using the Scaled Conjugate Gradient (SCG) learning algorithm. Even if this algorithm take longer to make the learning process, their fitting to the training and validation bases is better for this case than the fitting obtained with Levenberg-Marquardt learning algorithm. The minimum value of R^2 considered for this case was 0.8.

Figure 5.16 shows the performance of the MPL-Pc for the training, validation and test bases.

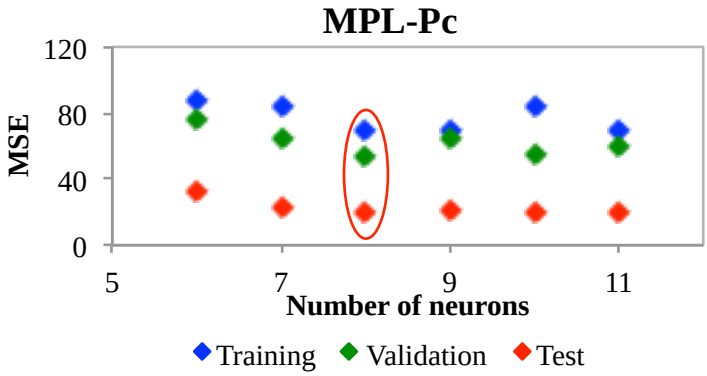

Figure 5-16. Performance of the MLP-Pc for the training, validation and test bases.

As it can be observed, the stabilization of the MSE was at 8 neurons.

5.7.3. Results on SENSO base

Figure 5.17 shows the training optimization process for the chosen MPL-Pc. As it can be seen, the MSE is between 50 and 70 mm^2 for the training and validation bases and, below 20 mm^2 for the test base. Moreover, the R^2 is above 0.8 for the training base and above 0.9 for the test base.

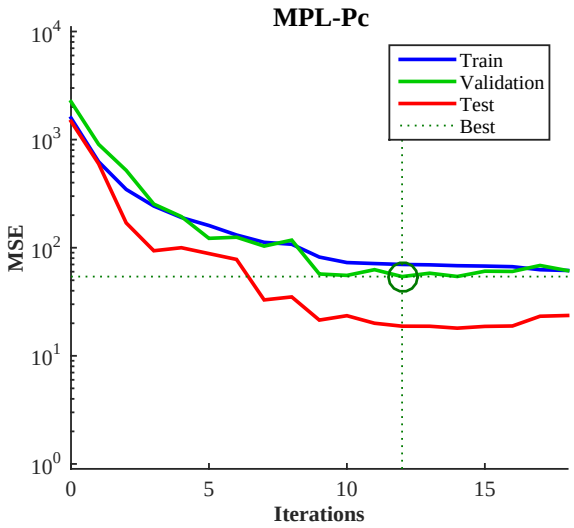

Figure 5-17. Training optimization process for the chosen MPL-Pc.

Furthermore, the Absolute Mean Error calculated between the Pc measured values and the Pc estimated values was of 5.9 mm. Hence, to assess its performance, this model will be tested on the on-site case of the next chapter.

Figure 5.18 shows the correlations between the predicted and measured carbonation depth values for the testing, validation and test bases of the chosen MPL-Pc model. For the training base composed of 45 samples, the correlation does not seem very good as the MSE is 70 mm^2 and the R^2 is below 0.9. For the validation base, composed of 10 samples, the correlations

showed to be better as the MSE is below 55 mm^2 and the R^2 is over 0.9. Moreover, for the test base the MSE was below 20 mm^2 and its R^2 above 0.9.

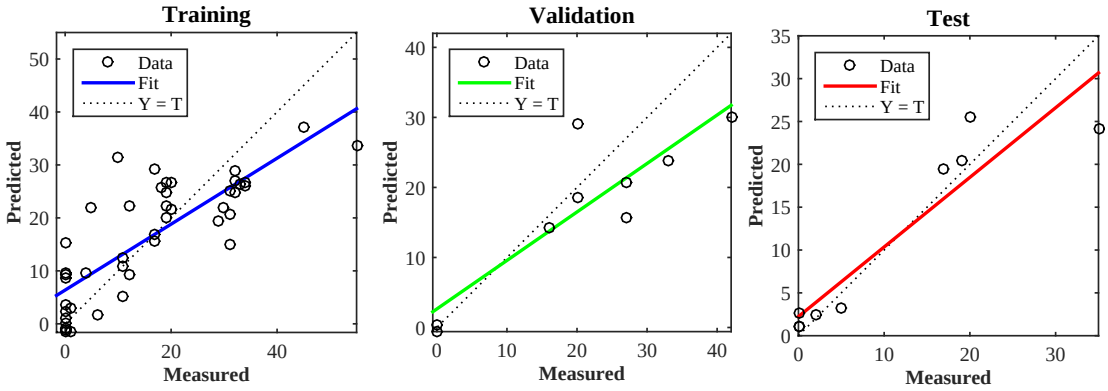

Figure 5-18. Correlations between the predicted and measured carbonation depth values for the training, validation and test bases of MPL-Pc model.

5.8. Performance on selected models and comparison between data fusion and ANN on a case-study: Le-Havre thermal power plant

Le-Havre thermal power plant was selected to test the performance of the chosen MPL models of w, P and Rc and to compare it to the performance of the data fusion tool (without updating) developed on the ACDC project and described in chapter 2. As carbonation was not significant for this site, the MPL-Pc models were not tested here.

In chapter 3, section 3.5.2 Le-Havre thermal power plant is presented. Only one wall (Wall III-N), which is the same used for the OSSM study (chapter 3) is considered in this chapter. Figure 3.13 shows the location of the studied wall III-N and figure 3.14 shows the grid detail: one for the 2D data, hence, 10 auscultation points, and one for the correlation depth data (LC-1D), hence, 27 auscultation points. Hence, a total of 37 measurements of 5 observables:

- 5 - ultrasonic pulse velocity (UPV),
- 7 - Impact Echo - Dynamic modulus of Young (IEE),
- 8 - Impact Echo - Compressive waves velocity (IE_Vp),
- 9 - capacity of large electrodes – Permittivity (CLEP) and,
- 11 - Log of the quadripole resistivity 5 cm (RE5)

were made for pre-auscultation and auscultation. Besides, a total of 5 cores (3 for auscultation and 2 for pre-auscultation) were extracted to obtain the values of Rc, P and w by destructive testing.

5.8.1. Performance of w, P and Rc MPL models

The estimated 37 values of w, P and Rc were calculated as follows:

- For w: Measurements of the observables UPV, IEE and CLEP were used as inputs for the MPL-w model. Figure 5.19 shows the 37 estimated w values and the 5 targeted w values representing the w values obtained from destructive test made on the 5 cores extracted.

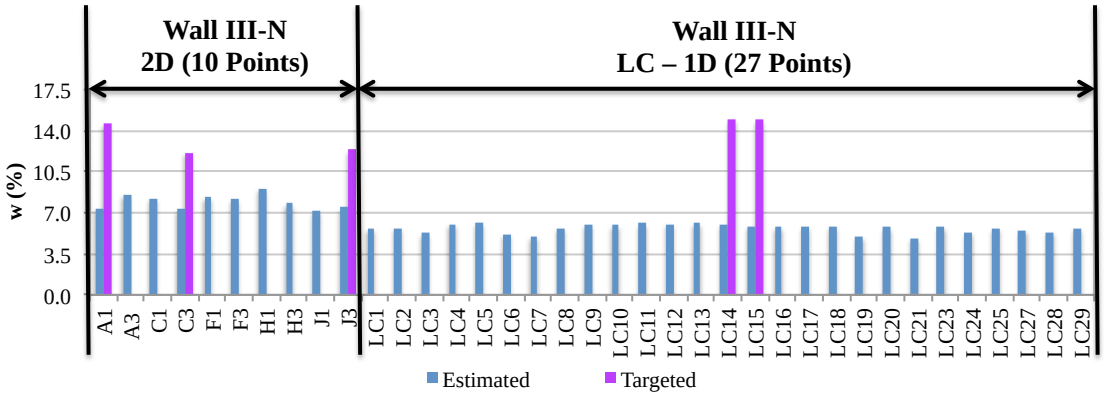

Figure 5-19. Estimated 37 w values and targeted w values of the 5 extracted cores of the wall III-N.

- For P: Measurements of the observables IEE, CLEP and RE5 were used as inputs for the MPL-P model. Figure 5.20 shows the 37 estimated P values and the 5 targeted P values representing the P values obtained from destructive test made on the 5 cores extracted.

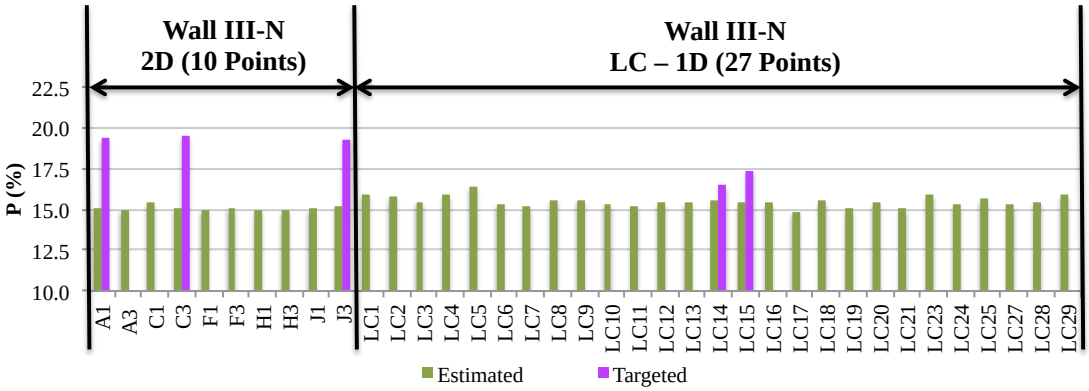

Figure 5-20. Estimated 37 P values and targeted P values from the 5 extracted cores of the wall III-N.

- For Rc: Measurements of the observables UPV, CLEP and RE5, as well as the estimated values of w calculated above were used as inputs for the MPL-Rc model. Figure 5.21 shows the 37 estimated Rc values and the 5 targeted Rc values representing the Rc values obtained from destructive tests made on the 5 cores extracted.

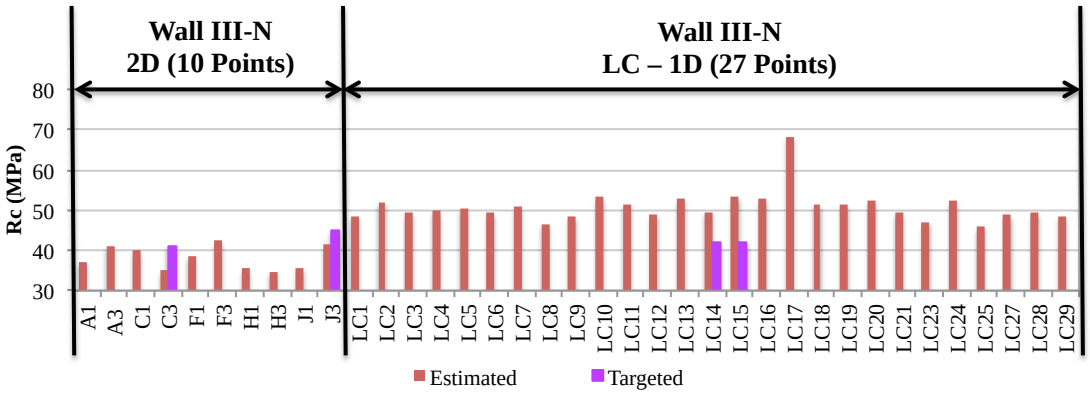

Figure 5-21. Estimated 37 Rc values and targeted Rc values from the 5 extracted cores of the wall III-N.

To evaluate the performance of the MPL models, Relative Mean Error (RME) (equation 5.3) was calculated between the DT targeted indicators values and the estimated indicators values located in the same positions as the DTs. Figure 5.22 shows the values of RME for the targeted indicators.

$$RME = \frac{1}{N}\sum_{i=1}^{N}\frac{|V_T - V_P|}{V_T} \tag{5.3}$$

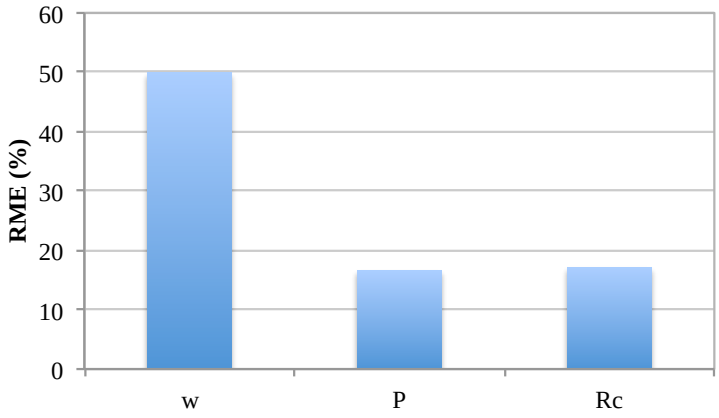

Figure 5-22. RME values of w, P and Rc obtained by ANN.

As it can be seen, all RME values for both P and Rc targeted indicators are below 20 %, and 50% for w. which is is surprising. If we consider that the ANN is a method that is quite good to interpolate values, and all observable and targeted indicator values with the exception of P are between the limits of the SENSO ranges, the indicators estimation should be better. Hence, a calibration of the MPL models or a calibration of the outputs should be considered in order to obtain better results.

5.8.2. Performance comparison between data fusion and ANN

As said at the beginning of this chapter, this on-site application was chosen to compare both methods: ANN and data fusion. For being able to compare them, it is important to put both methods under the same conditions. As the RNA is trained only with laboratory data

(SENSO data), the outputs of this method are adapted to this data. The data fusion tool as it was developed, uses multi-linear correlation laws between one observable and a pair of indicators that were obtained from the same laboratory data (SENSO data). Then, as it is described in chapter 2 and 4, an updating of the method is necessary to adjust the raw fused results to the data measured on-site. However, for being able to compare both methods, the raw fused data was used without updating.

As described in chapter 2, the data fusion tool estimates a pair of indicators at a time, the estimation of the 3 targeted indicators is going to be as follows:

- For Sr and Rc: Measurements of the observables UPV, IEE, IVP, CLEP and RE5 were used as inputs. Figure 5.23 shows the 37 estimated values of Sr and Rc as well as the EQ for each estimated value.

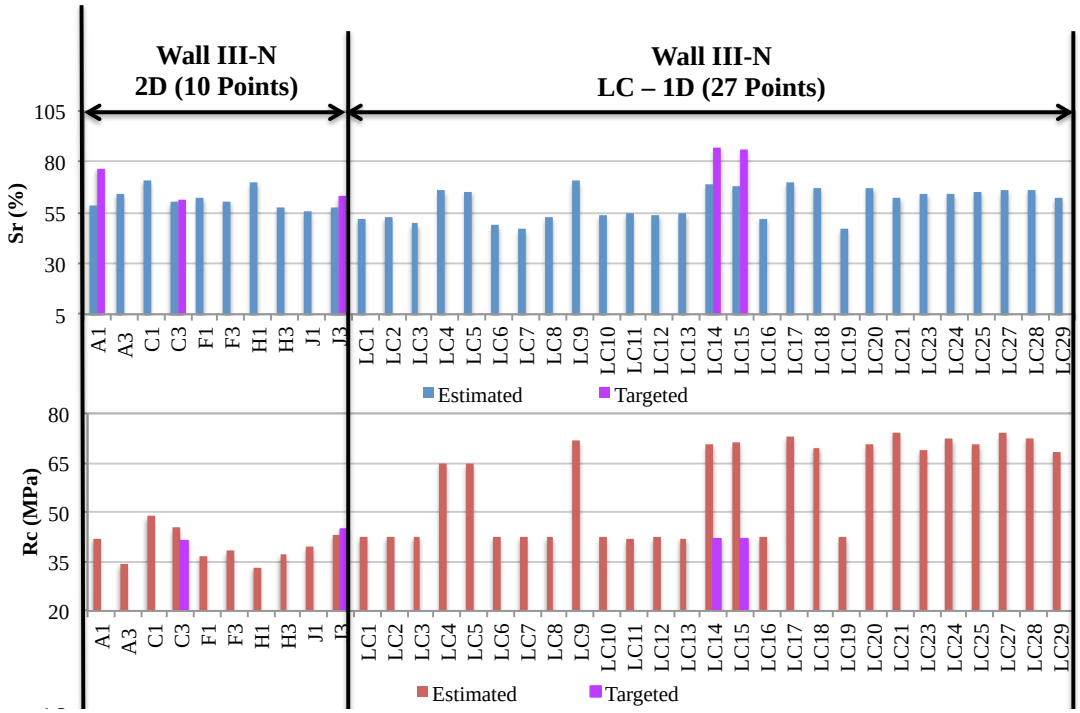

Figure 5-23. Estimated Sr, Rc and EQ values of the wall III-N.

- For Sr and P: Measurements of the observables IEE, CLEP and RE5 were used as inputs. Figure 5.24 shows the 37 estimated values of Sr and P as the EQ for each estimated value.

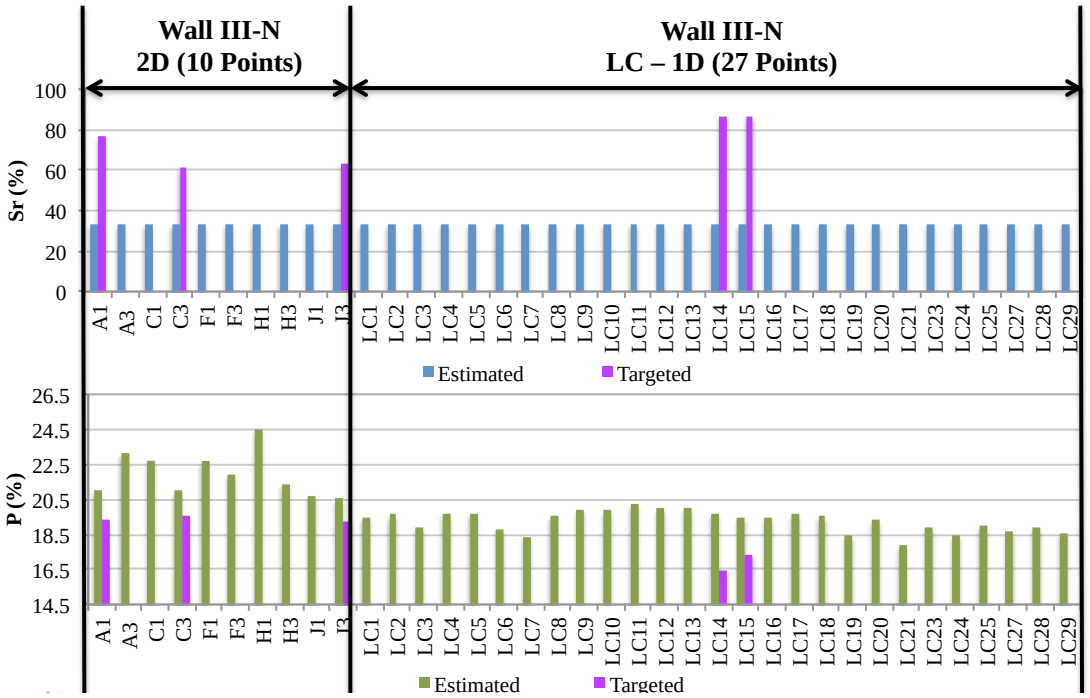

Figure 5-24. Estimated Sr, P and EQ values of the wall III-N.

It is important to highlight that these estimated values are the results of the raw fused values not updated (see chapter 2 and 4). This is made to put both methods under the same conditions to later compare their performances.

As it can be seen in figure 5.24, the Sr estimated values obtained from the Sr and Rc fusion are closest to the targeted values than the ones obtained from the Sr and P fusion. Following the same evaluation as the MPL models performance, the RME was calculated between the DT indicators values and the estimated indicators values located in the same positions as the DTs. Figure 5.25 shows the values of RME for ANN and data fusion for the targeted indicators. Moreover, table 5.8 shows the mean values for the estimated and targeted indicators, as well as the AME and RME between the estimated and targeted indicators for both ANN and data fusion.

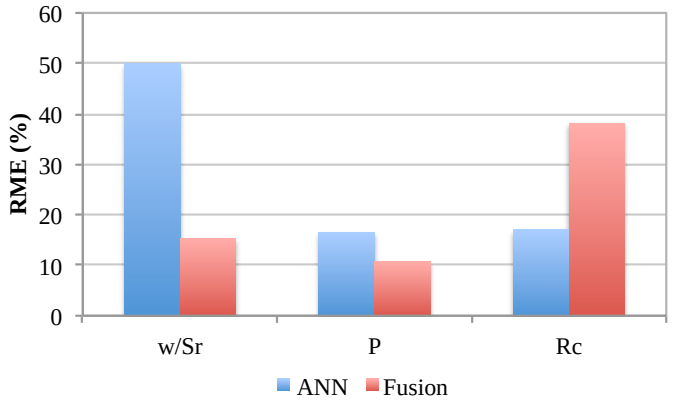

Figure 5-25. RME values of w/Sr, P and Rc obtained by ANN and data fusion.

Table 5-8. Mean values, AME and RME for the estimated and targeted indicators for ANN and data fusion.

		Estimated (Mean)	Targeted (Mean)	AME (%)	RME (%)
ANN	**w (%)**	6.3	13.8	7.0	49.9
	P (%)	15.4	18.4	3.1	16.5
	Rc (Mpa)	47.4	42.4	7.2	17.1
Fusion	**Sr (%)**	60.3	75.7	12.3	15.4
	P (%)	20.0	18.4	1.9	10.8
	Rc (Mpa)	53.1	42.4	15.9	38.1

As it can be seen, for ANN, the RME values for the 3 targeted indicators are below 20 %. For data fusion (raw results), the RME values for Sr and P are below 15 %, while the RME value for Rc is over 35 %. These results not only confirm that Sr and P estimated values are more reliable than Rc estimated values, but it also shows that with data fusion performance is better for the estimation of Sr and P, while the ANN performance is better for the estimation of Rc.

5.9. Conclusions

Artificial Neural Network method is tested as an alternative NDT combination method. In this chapter, it is shown the aptitude of ANN for the prediction of four concrete indicators: Water content (w), porosity (P) compressive strength (Rc) and carbonation depth (Pc).

First, the performance of the different ANN models for each targeted indicator (w, P, Rc and Pc) was first tested with the SENSO database. The chosen models were the following:

- For w, the MLP-w obtained with the input configuration 579 as the MSE is inferior to 1 %, the R^2 is over 0.98 and the AME is below 1%.
- For P, the MLP-P models obtained with the input configuration 48912 or 7912 as the MSE is inferior to 1 %, the R^2 is over 0.8 and the AME is below 0.45% for both models.

- For Rc, the MLP-Rc obtained with the input configuration 5912w, which means that a better estimation of Rc can be obtained with w as an input value. For this model, the MSE is inferior to 12 MPa^2, the R^2 is over 0.95 and the AME is below 2.5 MPa.
- For Pc, the model MPL-Pc has a MSE below 70 mm^2, the R^2 is over 0.9 and the AME is below 6 mm.

Later, an application of the selected ANN models for w, P and Rc was made on a wall of Le-Havre site. A total of 37 measurements of 4 observables: ultrasonic pulse velocity, Impact Echo - Dynamic modulus of Young, Impact Echo - Compressive wave velocity, capacity of large electrodes – Permittivity and Log of the quadripole resistivity 5 cm were made for pre-auscultation and auscultation. Besides a total of 5 cores were extracted to obtain the indicators destructive tests values of Rc, P and w. The performance of the ANN models as well as the comparison between ANN and data fusion methods was made. It was concluded that for ANN, the RME values for P and Rc are below 20 %, while for w is 50%. For data fusion (raw results without updating), the RME values for Sr and P are below 15 %, while the RME value for Rc is over 35 %. Therefore, in this case, the estimation of Sr and P is better with data fusion method, while the estimation of Rc is better with ANN.

For future works, it would be important to find a way to update either by found neural network models or by outputs. This in order to obtain results that can fit better to targeted values, as it was already developed for the fusion data tool (see chapter 4).

References

[1] Sbartaï, Z.M., “Caractérisation physique des bétons par radar approche neuromimetique de l’inversion”, Doctoral thesis, Toulouse and Sherbrooke universities, 2005.

[2] Viriyametanont, K., “Reconnaissance physique et géométrique d’éléments en béton armé par radar et réseaux de neurones artificiels”, Doctoral thesis, Toulouse university, 2008.

[3] Balayssac J.P., Laurens S, Arliguie G, Breysse D, Garnier V, Dérobert X, Piwakowski B. Description of the general outlines of the French project SENSO – Quality assessment and limits of different NDT methods. Construction and Building Materials, Volume 35, October 2012, p. 131-138.

CHAPTER 6
ON SITE APPLICATION - CEA SACLAY

6.1. Introduction

As mentioned in chapter 2, Non-Destructive Testing (NDT) methods are essential not only for detecting anomalies, but also for assessing concrete indicators and their variability during the diagnosis of civil engineering structures. NDT is a powerful tool for reducing the auscultation budget of a concrete structure. The proposed approaches described in chapters 3, 4 and 5 are included in EVADEOS project which goal is to optimize the monitoring of civil engineering structures by implementing preventive maintenance to reduce costs.

In the case of this chapter, the aim was to use the tools developed during this thesis on a case study, which includes non-destructive and destructive measurements taken on a wall of the CEA-Saclay, France.

- First, the performance of the OSSM described in chapter 3 was explored on non-destructive measurements taken on the studied wall. Besides, the fusion tool developed in a previous project and described in chapter 2 was used to obtain saturation degree and porosity in each auscultated point of the wall. These indicators were used later to locate optimally some destructive tests using the OSSM.

- Since for this structure, there is no correlation between the fused and the destructive testing indicators, as assumed in the updating by affine transformation, the propagation of DTs uncertainties proposed in chapter 4 was not made.

- Finally, the performance of the artificial neural network models described in chapter 5 was tested principally for carbonation depth model, but also for water content, porosity and compressive strength.

CEA-Saclay is one of the studied sites selected for EvaDéOS project. The interest of this site is that the concrete is significantly carbonated with relative depths close to the reinforcement depth. The case study considers two walls: one facing north (Wall N) and the other facing south (Wall S). These walls were built in 1979, their lengths vary between 20 and 40 m and their height is approximately 2.2 m. Figure 6.1 shows the location of the walls inspected as part of this project.

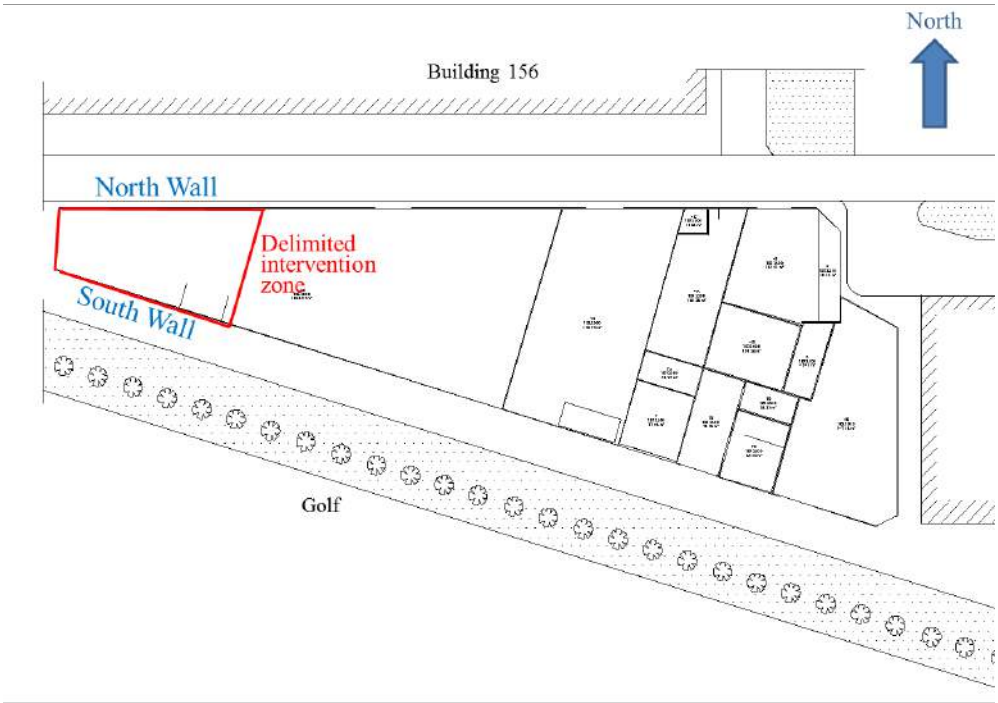

Figure 6-1. Location of the inspected walls.

A pre-auscultation and auscultation campaign was made in July 2014 where different NDT methods such as capacitive method, ultrasound, impact echo, resistivity, rebound hammer, permeability and GPR were used. The weather was rather hot and dry, which affected mostly the measurements of low penetration methods. The industrial approach of concrete assessment implies to reduce the number of NDT tests and cores to optimize the auscultation cost. For this study, only the North wall (wall N) was considered.

6.2. Validation of the OSSM

6.2.1. Spatial sampling design for NDT measurements: Impact Echo and Capacitive method

Many NDT methods were used in this measurement campaign, but only the measurements of the permittivity by the capacitive method (P_Capa) and the compression wave velocity measured by the impact-echo technique (Vp_IE) were used and analyzed here to test and validate the developed approach. These observables are very sensitive to two different indicators: Vp_IE is very sensitive to the porosity and P_Capa is very sensitive to the saturation degree, thus, two different fields to test the OSSM. Moreover, these methods were used in the data fusion process to estimate the porosity and saturation degree as mentioned below.

For being able to do this, a series of 28 capacitive and impact echo measurements were made for the pre-auscultation of the wall N. They are distributed along two parallel horizontal lines. Figure 6.2 shows the grid detail. A spherical variogram was fitted to P_Capa and Vp_IE experimental data. The fitted curves have a nugget of 0.02 and 0 $(m/s)^2$, a range of 0.6 m and

0.51 m and a sill of 0.24 and 8894 $(m/s)^2$ respectively. These variograms and the kriging method were then used for the spatial interpolation process in order to obtain the original fields for both NDTs. Figure 6.3 shows the Vp_IE and P_Capa original fields and variograms. As it can be seen, three different zones of 13 m large are clearly identified.

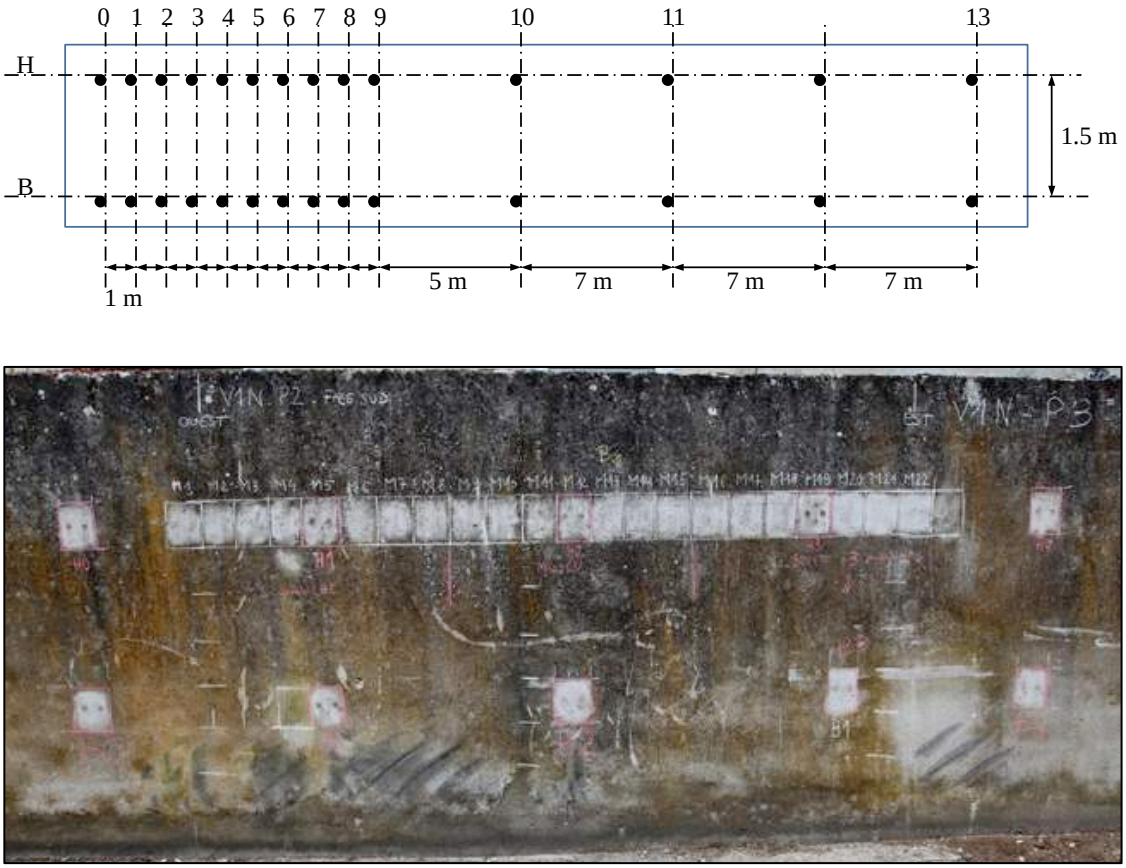

Figure 6-2. Grid detail for the pre-auscultation of the wall N.

The OSSM performance was explored with different number of measurements (n). Figure 6.4 shows the variation of the two objective functions - MPE (Figure 6.4a and Figure 6.4c) and VEE (Figure 6.4b and Figure 6.4d) – with n measurements organized on a regular grid (before optimization) and with the optimized location of those n measurements organized on an irregular grid (after the OSSM) for P_Capa and Vp_IE.

If MPE is used as the objective function, we can observe a significant decrease in its value for P_Capa (Figure 6.4a) of 49% on average from a regular grid to an irregular one. In the case of Vp_IE (Figure 6.4c), there is a decrease in average of 55% for MPE. From Figure 6.4b, it can be deduced that if n is reduced to 13, the new global variance is equal to that obtained with the original 28 measurements P_Capa. In figures 6.4a and 6.4b it can also be seen that if we fix a MPE value of 2% for P_Capa and a MPE value of 1.6% for Vp_IE, we can reduce the number of measurements from 18 to 8 just by organizing the 8 measurements in an optimal irregular

grid. Figure 6.5 illustrates the reduction of number of measurements from 18 to 8 by fixing a MPE value. As it can be seen for both NDTs, the details of the kriging maps obtained with the 18 measurements organized in a regular grid are not lost when the number of measurements is reduced to 8 organized in an optimal irregular grid, if we compare them to the original maps.

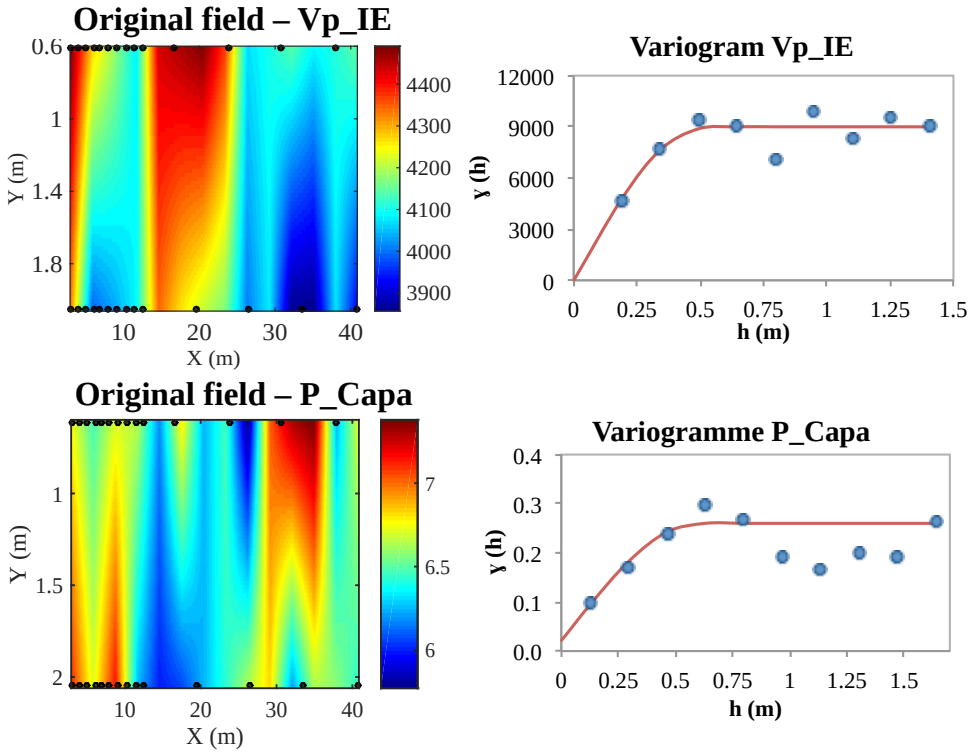

Figure 6-3. Variograms and original fields of Vp_IE and P_Capa.

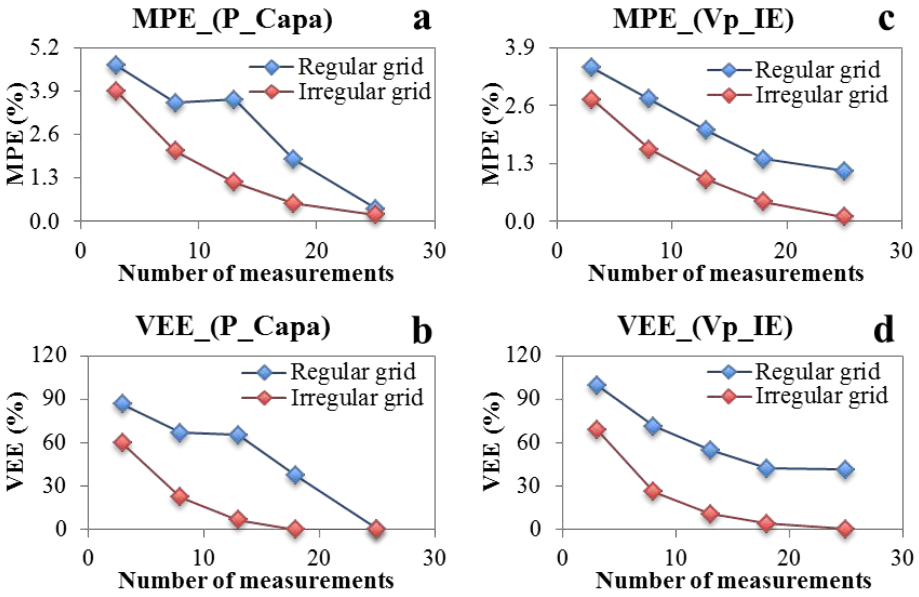

Figure 6-4. Relationship between the number of measurements and the fitness function values for a) MPE (P_Capa), b) VEE (P_Capa), c) MPE (Vp_IE) and d) VEE (Vp_IE). Regular grid (blue points) and optimal irregular grid (red points).

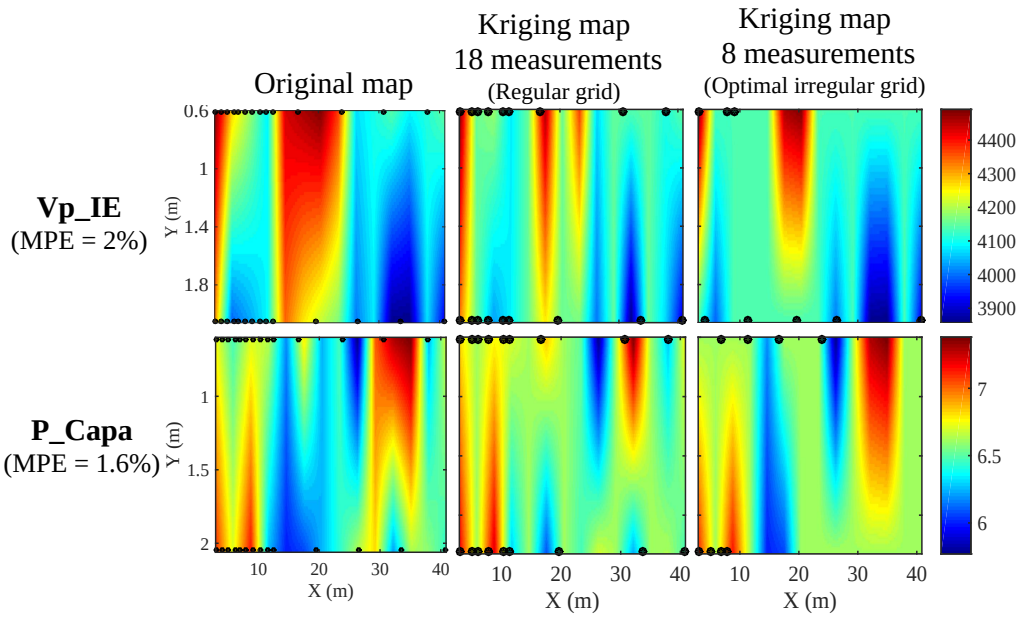

Figure 6-5. Illustration of the reduction of number of measurements from 18 to 8 by fixing a MPE value for P_Capa and Vp_IE.

We can better visualize the impact of the optimization from Figures 6.6a to 6.6d.

- Figure 6.6a shows the original map with 28 Vp_IE measurements,
- Figure 6.6b shows the kriging map obtained with 13 measurements organized in a regular grid,
- Figure 6.6c shows the kriging map obtained with 13 measurements organized in an irregular grid optimized by the algorithm with MPE as the objective function and,

- Figure 6.6d, shows the kriging map obtained with 13 measurements arranged in an irregular grid optimized by the algorithm with VEE as objective function.

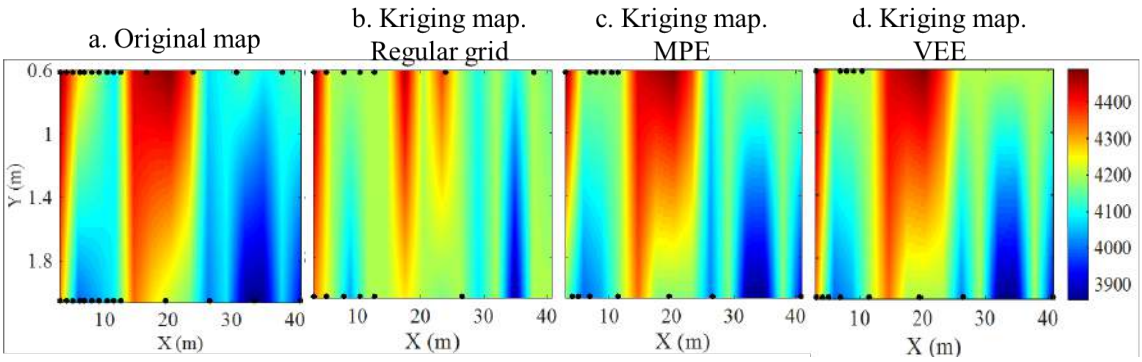

Figure 6-6. a) Original Vp_IE map with 28 measurements, b) Kriging map made with 13 measurements organized in a regular grid, c) Kriging map made with 13 measurements organized in an optimal irregular grid obtained after OSSM with MPE as fitness function, d) Kriging map made with 13 measurements organized in an optimal irregular grid obtained after OSSM with VEE as the fitness function.

MPE and VEE showed interesting performances. Their value is reduced by 52% and 75% on average for both NDT methods going from a regular grid to optimal irregular one. Note that MPE leads to a smaller mean prediction error in the kriging map and a mean value closer to the original one than the mean obtained with VEE. On the other hand, VEE provides a variance value closer to the global variance than MPE. In this case VEE and MPE gave an almost identical kriging map. However, special attention should be paid to what is expected before selecting the most appropriate objective function to analyze a particular data set. For example, if the structure manager wants to know the spatial distribution to optimize further controls or if he wants to locate the priority zones to schedule maintenance, MPE must be used. If, on the contrary, he wants to estimate the overall variability of the material for reliability calculation, VEE should be chosen. Since the aim of our work is to optimize the monitoring of civil engineering structures by NDT methods, MPE will be privileged in the next section.

6.2.2. Spatial sampling design for destructive testing

As part of a complete and reliable inspection, destructive laboratory testing on concrete samples obtained by coring is needed to confirm and calibrate the results of the indicators obtained by the fusion of different NDT methods [1]. Because of the cost of both coring and destructive testing can be prohibitive, and it can induce damage to the structure, it is important to propose an optimal spatial sampling plan to extract a limited number of cores.

In this chapter, the objective is to locate in the best way possible the cores to extract, to make destructive tests to obtain the saturation degree and porosity for each core. In order to do this, ideally we should have the measurements of saturation degree and porosity for each auscultation point to use the OSSM. However, as mentioned before, it is not usual to take 28 cores. Therefore, we combined the capacitive method, impact echo and electrical resistivity through a

fusion process based on the theory of possibilities and described in chapter 2 to obtain the reference maps for saturation degree and porosity at each point of the auscultated wall. It is assumed that these reference maps have a similar spatial variability from the ones that would be obtained if destructive tests were made on 28 cores extracted in each one of the auscultated points. Only 25 points were selected for the OSSM implementation due to the non-destructive measurement errors identified in the fusion process.

For each one of the concrete indicators (porosity and saturation degree), a variogram was determined. As shown in Figure 6.7a, a spherical variogram with a range of 0.18 m, a sill of 38.9% and a nugget of 0% has been fitted to the saturation degree data. It is important to point out that the range is a fitted parameter and the correlation length is of about 60 cm as can be seen in figure 6.7a. In contrast, for the porosity, no model could be fitted (Figure 6.7b). This means that the distribution of the porosity throughout the wall is constant, which means that for any distance between measurements the variance is similar. The location of cores for assessing the porosity doesn't have significant effect and can be anywhere. Hence, the cores for assessing the porosity can be located at the same positions as the ones obtained after OSSM made for the saturation degree with MPE and VEE as fitness functions. We can see from figure 6.7 that if correlation and a variogram can be found for the NDT data, concrete indicators do not necessarily show the same spatial correlation. This can be due to the dependency of NDT to more than one concrete indicator.

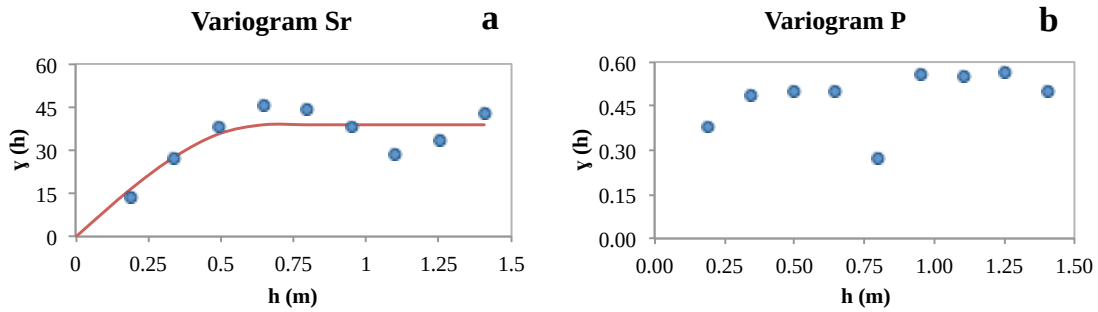

Figure 6-7. Empiric variograms (points) and the respective adjusted models (lines) of the indicators studied on the auscultated wall. a) Saturation degree variogram, b) Porosity variogram.

For this approach, it was used two objective functions: MPE_Sr and VEE_Sr for the saturation degree. We study this minimization for different number of cores. Figures 6.8a and 6.8b show the evolution of each objective function according to the number of cores organized in a regular grid before optimization (blue curve), and in the case of an irregular grid after optimization (red curve). The advantage of this transition to an irregular grid is to give an additional degree of freedom in the grid to reduce the objective function value.

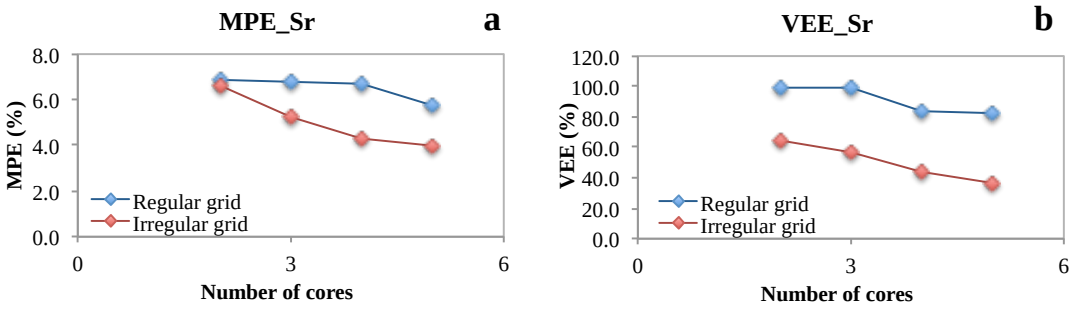

Figure 6-8. Relationship between the number of cores and fitness function values for a) MPE_Sr, b) MPE_P. Regular grid (blue points) and optimal irregular grid (red points).

It is noted on the figures 6.8a and 6.8b that the error decreases to 24% and 45% in average from a regular grid to an irregular one for the case of OSSM with MPE_Sr and VEE_Sr respectively. However, although the location of the cores on an irregular grid significantly decreases the error, the decrease is not as important as in the case of spatial optimization of NDTs. It can be expected due to the reduced number of cores (known values).

Figure 6.9 shows an example of the optimization with 5 cores. In the left part of the figure, we have the reference maps for saturation degree and porosity obtained after fusion. In the middle part of the figure, we have the kriging maps for saturation degree and porosity after optimization carried out with 5 cores and MPE_Sr as the objective function. Finally, in the right part of the figure, we have the kriging maps for saturation degree and porosity after optimization carried out with 5 cores and VEE_Sr as the objective function. In the figures, it can be clearly seen the objective of each fitness function. Even though the number of cores is only 5, the kriging maps obtained with the locations provided by OSSM and MPE_Sr as the fitness function for both reference maps (Sr and P) are quite similar. Moreover, when VEE_Sr is used as the fitness function, it is observed that the optimized locations search to find the maximum and minimum zones. Besides, using exactly the same locations for Sr and P, optimizing only the locations of Sr, confirms that the variability of the porosity is constant. Hence, satisfying results for Sr and P can be obtained with only the optimized locations of Sr.

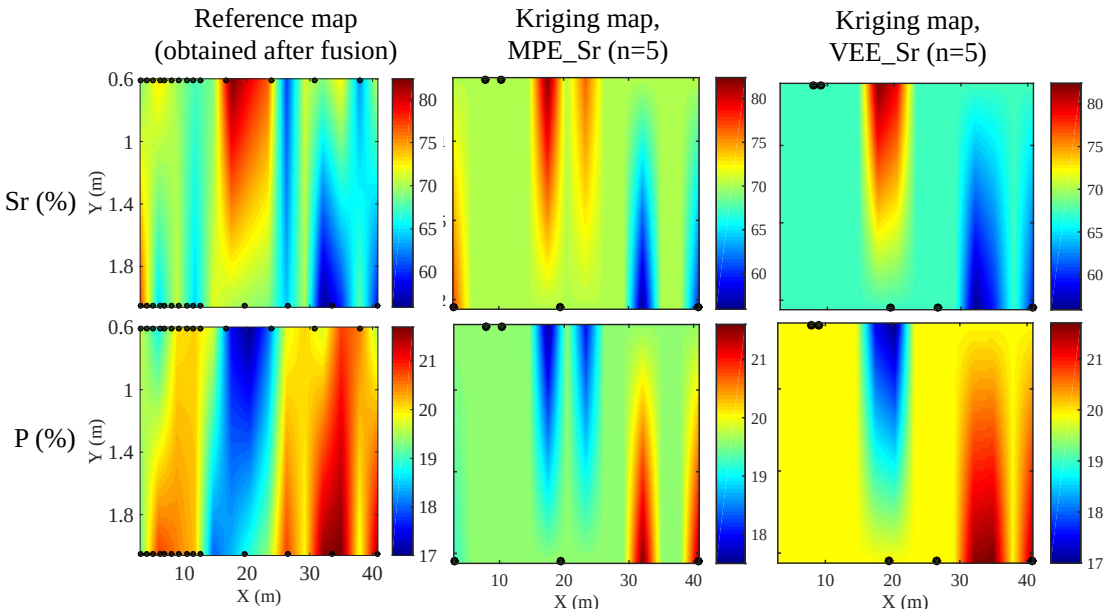

Figure 6-9. Saturation degree and porosity reference maps. Left side: original maps. Middle: kriging maps after optimization made with 5 cores and MPE_Sr as the objective function. Right side: kriging maps after optimization made with 5 cores and VEE_Sr as the objective function.

6.3. Estimation of carbonation depth by Artificial Neural Networks

As mentioned in chapter 5, Artificial Neural Networks (ANN) showed to be a promising NDT combination tool to predict carbonation depth (Pc) values. The chosen ANN model was a multilayer perceptron with one input layer composed of 6 observables (Table 5.7), one hidden layer composed of 8 neurons and one output. This model (MPL-Pc) was obtained with the scaled conjugate gradient training algorithm, which showed better results than the Levenberg-Marquardt. With this model, an Absolute Mean Error (AME) of 5.9 mm was obtained for the EVADEOS and SENSO-Pc databases.

Table 5.7. The 6 observables used as inputs for the MPL-Pc.

Number	***Observable***
4	Surface Ultrasound - Wave velocity 3 cm (m/s)
5	Ultrasound Pulse - 250kHz transmission velocity (m/s)
9	Capacity of large electrodes - Permittivity
11	Log of the quadripole resistivity 5 cm
14	GPR pic to pic amplitude
16	Direct wave GPR velocity (cm/s)

In the case of CEA, 26 pre-auscultation measurements out of the 28 were selected, due to the absence of some NDT measurements and used on the MPL-Pc. Moreover, 15 Pc values were obtained by destructive tests made from extracted cores in order to evaluate the performance of the MPL-Pc on the studied case. Figure 6.10 shows the 26 estimated and targeted values of Pc. For this case study an AME of 10 mm was obtained, hence a Relative Mean Error (RME) of 49 %.

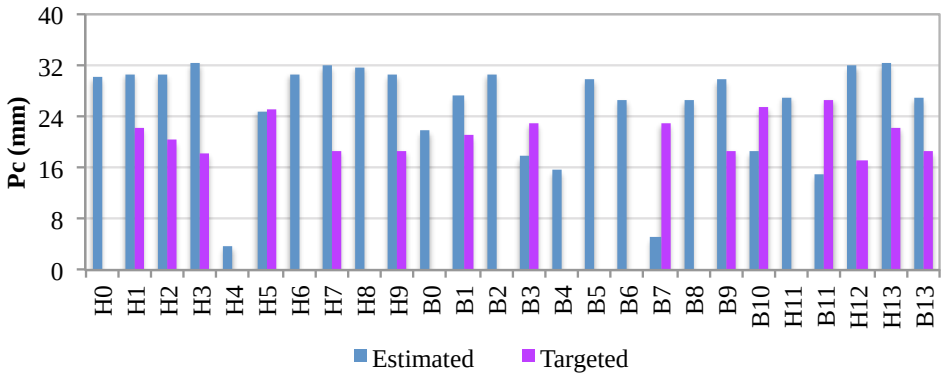

Figure 6-10. Estimated values of Pc with MPL-Pc and targeted values obtained from 15 DTs of the wall N.

The carbonation is a concrete pathology that affects principally the surface of the concrete and it evolves with time. Hence, concrete indicators such as w, P and Rc are also expected to be affected by it. For example, some works have showed that carbonation decreased the porosity of concrete by clogging up the pores and reducing the pore sizes, thus, for an important carbonation depth value an increase of Rc is expected [2-5]. Carbonation could affect w, but in this case study it should mostly be affected by the weather conditions at the moment of the measurements. The w, P and Rc MPL models defined in chapter 5 and based on non-carbonated concretes were also tested and the indicators results were compared to the DTs results obtained on surface concrete (carbonated part of the extracted cores) and on core concrete (non-carbonated part of the extracted cores) for w and P indicators. Figure 6.11 shows the results for the estimated w, P and Rc and the targeted values of on core and surface concrete indicators for w and P, and the targeted values for Rc. Figure 6.12 shows the RME values and table 6.1 shows the AME values for Pc, Rc, w-surface, w-core, P-surface and P-core.

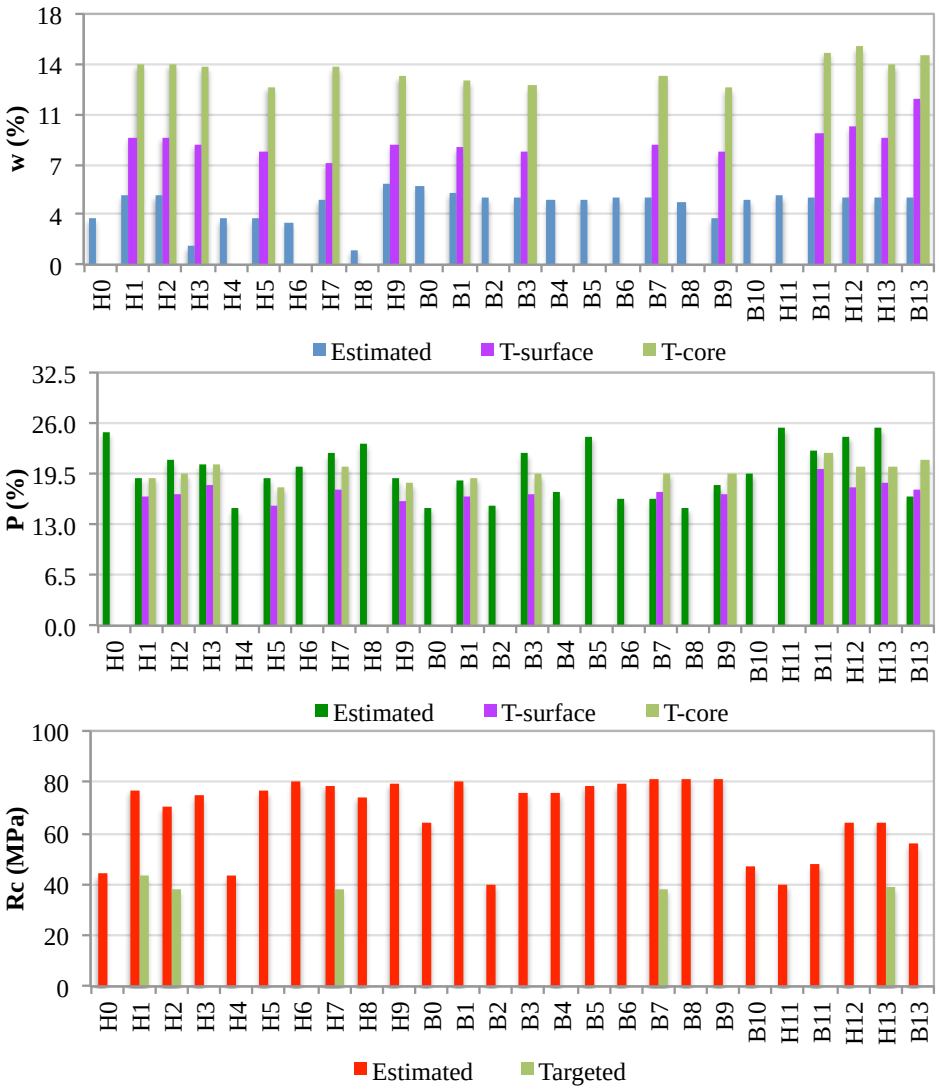

Figure 6-11. Estimated w, P and Rc and the targeted values of on core and surface indicators for w and P, and the targeted values for Rc.

As it can be seen in figure 6.12, there is a slightly decrease of the MPL model performance for the estimation of P if we want to evaluate the porosity on surface. On the other hand, a performance increase of the MPL-P model is found if we want to evaluate the core porosity (RME P-surface value more important than RME P-core value). This is expected, because the data used to train the model was obtained from non-carbonated concretes. However, the same does not apply for the estimation of w. The RME does not only increase significantly (the double compared to Le-Havre case study presented in chapter 5), but also the performance of the MPL-w model is worse if we want to estimate the water content of core concrete than if we want to estimate the water content of surface concrete (higher RME value obtained with w-core than the one obtained with w-surface). Therefore, as the estimation of Rc depends on the results of the w estimated, it is expected that the performance of MPL-Rc model to be highly decreased.

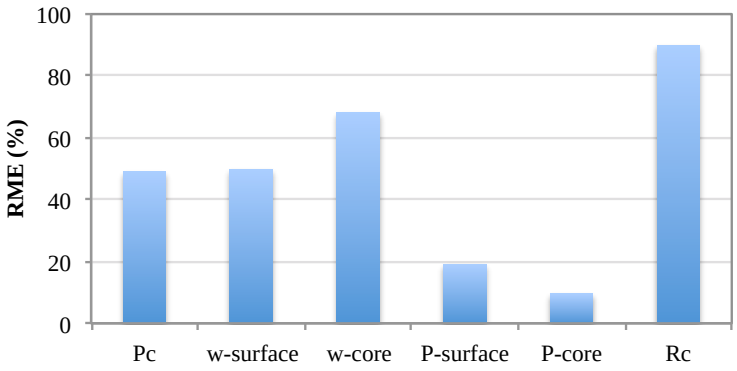

Figure 6-12. RME values for Pc, Rc, w-surface, w-core, P-surface and P-core.

The increase of RME values demonstrates the need of a calibration to obtain better results adapted to the structure, as a performance decrease of the MPL models was found for the estimation of core concrete indicators, which are not carbonated. Besides, the difference of RME values between the core and surface concrete indicators shows that the performance of the MPL models for the estimation of the indicators on surface, are affected by the presence of the carbonation. Thus, as the MPL-w model performance was the most affected, affecting also the performance of the MPL-Rc model significantly, a new MPL-wc model was trained with the EVADEOS and SENSO-Pc databases, which contain carbonated concretes. This, in order to estimate better the water content on surface for the study case. The new MPL-wc model was trained with the scaled conjugate gradient algorithm, which as well as the Pc case (described in chapter 5) showed better results than the Levenberg-Marquardt algorithm. Figure 6.13 shows the architecture of this MPL-wc model with the same 6 inputs as the Pc case and 7 neurons in the hidden layer.

With this new MPL-wc model an AME of 2.2 % and a RME of 24 % (table 6.1) was obtained when the estimated values are compared to w-surface values. Consequently, a significant increase in the estimation of w-surface is obtained. Now, if we take these new water contents estimated values and we include them in the MPL-Rc model, we obtain a AME and RME of 18.7 MPa and 48.1 % respectively (table 6.1), that are half of the ones obtained before. Even though, the improvement on AME and RME are significant for Rc, these values remain important. It is expected, as the values of w used for the estimation of Rc are the w-surface. For obtaining a better estimation of Rc, we should use w-core values, but for now we do not have a MPL-w model that gives a good estimation of w-core values when the surface of the concrete is carbonated.

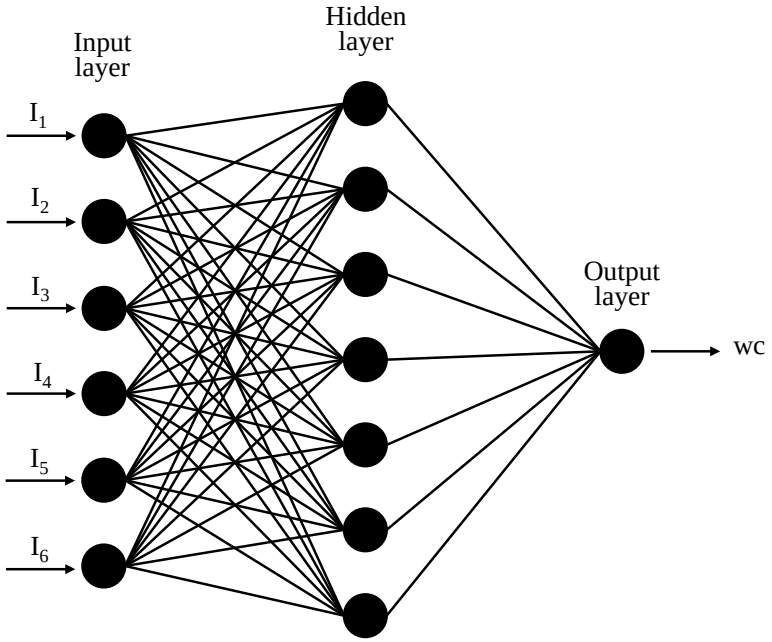

Figure 6-13. Architecture of the MPL-wc.

Table 6-1. Mean, AME and RME values for Pc, Rc, w-surface, w-core, P-surface and P-core estimated and targeted values for the estimation of w-surface with MPL-w and MPL-wc models.

		Estimated (Mean)	Targeted (Mean)	AME	RME (%)
With MPL-w model	**Pc (mm)**	25.4	21.3	10.0	49.1
	w-surface (%)	4.2	8.6	4.3	49.7
	w-core (%)	4.2	13.6	9.3	68.3
	P-surface (%)	19.9	17.3	3.3	19.1
	P-core (%)	19.9	19.8	1.9	9.6
	Rc (MPa)	67.4	39.2	35.0	89.8
With MPL-wc model	**w-surface (%)**	6.5	8.6	2.2	24.0
	Rc (MPa)	55.7	39.2	18.7	48.1

6.4. Conclusions

This chapter provides an approach that can contribute to an effective characterization of structures by implementing NDT methods with the aim of limiting inspection costs. A preliminary study of a concrete structure was carried out with two non-destructive testing methods (capacitive method and impact echo) to evaluate the spatial correlation of a wall on the CEA site in Saclay, France. A first spatial optimization was made for later use in the case of a future auscultation with more performant NDTs or for a monitoring of the site. Then, the fusion of three NDTs (capacitive method, impact echo and electrical resistivity) is made by the theory of possibilities method to obtain the saturation degree and porosity values for the studied wall. After the fusion of the non-destructive measurements and the estimation of the two studied concrete indicators, a variogram model could be fitted only for the saturation degree. This

variogram was then used for the spatial optimization of the cores to extract from the studied wall.

For NDT spatial optimization, two objective functions were exploited: MPE and VEE. However, for cores to extract case, spatial optimization using only MPE and VEE for Sr as the objective functions were retained because no variogram model could be fitted for P, which means that its variability is constant throughout the studied wall. NDT optimization was tested with twenty-three, eighteen, thirteen, eight and three measurement points. All cases showed a decrease of the objective functions: 52% for MPE and 75% for VEE on average. It was also showed that if a MPE value is fixed, a decrease of the number of measurements is possible by organizing the reduced number of cores in an optimal irregular grid. Between regular and irregular spatial distribution of measurements for spatial optimization for destructive testing samples (cores), the algorithm was tested with five, four, three and two cores. The algorithm was run with MPE_Sr and VEE_Sr as fitness functions. All cases showed an important decrease of objective functions, but not as important as the NDT case. Maybe this difference can be due to a more important variability on NDTs (important difference between max et min values), than on DTs. The reduced number of cores can also explain this difference.

Later, the estimation of Pc values for each auscultated point was made by the use of the ANN model (MPL- Pc) described in chapter 5. Their AME and RME were 10 mm and 49 % respectively, which are a sign that a calibration to obtain better results adapted to the structure is necessary. MPL models for w, P and Rc were also tested and its results were compared to DTs made on surface and on core for the cases of w and P. In general, it was observed a decrease of the MPL models performance with the exception of MPL-P. Therefore, these results are good indicators not only for the need of a calibration to obtain better results adapted to the structure, but also, that the performance of the MPL models are affected by the presence of the carbonation. For this reason, a new model for w (MPL-wc) trained with SENSO-Pc and EVADEOS databases was developed. Its performance for the assessment of w-surface of the studied structure was increased significantly compared to the MPL-w model.

For future works, it will be important to develop a calibration process for the MPL implemented models and a careful consideration must be made to whether taking into account the effect of carbonation in the calibration process for the original w, P and Rc MPL models or to develop new models including carbonated concretes to assess the different indicators effectively. Moreover, the inclusion of the indicators uncertainties on the OSSM can be a good way of evaluating its performance, either as input data or as another fitness function.

References

[1] G Villain, Z.M Sbartaï, X Dérobert, V Garnier and J.P Balayssac, 'Durability diagnosis of a concrete structure in a tidal zone by combining NDT methods: laboratory test and case study', Construction and Building materials, Vol 37, pp 893-903, 2012.

[2] Cui, H., Tang, W., Zhijun, W.L., Dong, F., Xing, "Experimental study on effects of CO2 concentrations on concrete carbonation and diffusion mechanisms", Construction and Building Materials, Vol. 93, pp. 522-527, 2015.

[3] Chang, C.F., Chen, J.W, "Strength and elastic modulus of carbonated concrete", ACI Materials Journal, Vol. 102, pp. 315-321, 2005.

[4] Chang, C.F., Chen, J.W., "The experimental investigation of concrete carbonation depth", Cement and Concrete Research, Vol. 36, pp. 1760-1767, 2006

[5] Jerga, J., "Physico-mechanical properties of carbonated concrete", Construction and Building Materials, Vol. 18, pp. 645-652, 2004.

CHAPTER 7
CONCLUSIONS AND PERSPECTIVES

In order to estimate the degradation state of a concrete structure, it is important to plan a maintenance strategy at a minimum cost. For that aim, the development of an optimal diagnosis strategy is necessary. Until now, for assessing concrete properties in relation with the degradations destructive testing on cores is the most usual method. The location of cores is generally done after a visual inspection of the structure that can provide information about the presence or the consequence of pathology. The results of destructive testing, which are the concrete properties linked to the pathologies, called indicators, are used as inputs for prediction models. However, visual inspection as a diagnosis method remains informal and subjective. Regarding destructive testing, because of the concrete own variability and the spatial variability of concrete indicators a large number of cores must be extracted, so the cost of destructive testing can be prohibitive and disabling for the integrity, particularly if the structure is very large.

For that reason, non-destructive testing (NDT) is an interesting complement in the diagnosis of a concrete structure. However, NDTs are variable themselves and the concrete indicators can have combined effects on NDT measurements. So the combination of NDT methods is necessary and a methodology for exploring this combination and for merging the results is necessary.

French projects such as SENSO and ACDC have focused in developing different NDT methods to be used in combination and have also developed a data fusion method to obtain the most reliable information of the properties of a concrete slab or structure. To be used in real structure the fusion procedure requires a calibration by DT on cores. The minimum number of cores determines the quality of the calibration.

EvaDéOS project proposes a global methodology in which the concrete properties assessed by NDT are used as inputs of predictive models and as data for the actualization of the prediction. For this purpose it was necessary to provide information about spatial variability of properties. The assessment of spatial variability will require a minimal number of measurements, which is the main interest of NDT in comparison with DT. Nevertheless, it is important to emphasize that the diagnosis is limited by a budget. Hence, it is important to develop an optimal methodology for the assessment of concrete properties on real structures, taking into account the variability of both NDT and DT. Moreover it is also important to determine the minimum number of cores regarding the quality of fusion calibration. This was one of the objectives of this thesis. The other objective was to extend the combination methodology to other concrete properties. Because EvaDéOS project mainly focused on corrosion, carbonation was explored by NDT combination. A new approach of combination methodology was proposed by using artificial neural networks (ANN).

The first axe of the thesis was about the study of the spatial correlation and variability of NDT for creating an optimal spatial sampling method that will eventually be useful to plan an

optimal inspection strategy. **With this method it was shown that it is possible to improve the knowledge of the material properties (mean, variance, extreme values) and to locate specific areas where the investigation will be refined, by using a methodology based on variographic theory. When compared to investigation programs based on a regular grid, it enables to reduce the number of measurements to reach a given quality and/or to increase the quality if the number of measurements remains constant.** The optimal spatial sampling method uses two fitness functions: Mean Estimation Error (MPE) and Variance Estimation Error (VEE). They have different objectives and they may be complementary. The choice of one fitness function has to be done by considering the real objectives of the material assessment (mainly mean values or variance). Both fitness functions showed a high improvement in the representation of all cases studied (simulated field and on-site ultrasonic velocity measurements). However, the VEE values are highly affected by the variation of the number of measurements and the correlation length, while the MPE values are only affected by the modification of the number of measurements.

The second axe of the thesis, seeks the reduction on the number of DTs and their optimal location by studying the sensitivity of the error obtained on the concrete properties estimated by data fusion. This error is obtained by introducing and propagating a fixed value of DT uncertainty through the data fusion process. A proposal of the introduction of the uncertainties representing the variability of indicators obtained by destructive tests of the studied material of a studied concrete structure is made. The propagation of these uncertainties to the indicators obtained by fusion is made through the updating by affine transformation, which assumes a linear relationship between the indicators obtained by DT and the indicators obtained by fusion of NDT.

This contribution offers to the structure manager additional entry information for the indicators prediction models. This additional information is the precision (standard deviation and statistical distribution) of the indicators obtained by the fusion of NDT methods for each auscultation point of the studied structure, as well as the sensitivity of this precision to the number and selection of cores. The method used to obtain this variation can be applied to any concrete structure.

The method was applied on a case study, where the studied indicators saturation degree and compressive strength have different variability. For the saturation degree, the indicator values obtained by fusion and the ones obtained by destructive test have a variability of 10 %, while for compressive strength is the double. For this study, it was found that the fused results for saturation degree are more sensitive to the value of DTs uncertainties than for compressive strength. It was also found that even though different configurations including minimum,

maximum and intermediary values were tested, the best configuration to place the cores for both indicators, belongs to the indicator that has more variability throughout the structure, in this case, compressive strength. Moreover, it was found that the error found for both indicators is correlated, when the configurations changes, but the number of cores is fixed. Then, if we fix the best configuration and we change the number of cores, a decrease power relationship between the error found for both indicators and the number of cores is found. In this case, an important decrease of the errors for both indicators is found, when the number of cores is reduced from 10 to 3. Moreover, the errors of both indicators for this case (fixed configuration and variable number of cores) are also correlated.

In the third axe of the thesis, the Artificial Neural Network (ANN) method was tested as an alternative NDT combination method. In this chapter, **it is shown the aptitude of ANN for the prediction of four concrete indicators: water content (w), porosity (P) compressive strength (Rc) and carbonation depth (Pc).** The performance of the different ANN models for each targeted indicator (w, P, Rc and Pc) was first tested with the SENSO database.

An MLP-w model for the estimation of w obtained with an input configuration composed of the observables UPV, IEE and CLEP was chosen as the MSE is inferior to 1 %, the R^2 is over 0.98 and the AME is below 1%. Moreover, two MLP-P models for the estimation of P obtained with input configurations composed of the observables 4, 8, 9, 12 and 7, 9, 12 were chosen as the MSE is inferior to 1 %, the R^2 is over 0.8 and the AME is below 0.45% for both models. Besides, an MLP-Rc model for the estimation of Rc obtained with an input configuration composed of w and the observables UPV, IEE, RE5 was chosen as the MSE is inferior to 12 MPa^2, the R^2 is over 0.95 and the AME is below 2.5 MPa. Finally, an MLP-Pc model for the estimation of Pc obtained with an input configuration composed of the observables UPV, CLEP, RE5, GPRV was chosen as the MSE is below 70 mm^2, the R^2 is over 0.9 and the AME is below 6 mm. It was also found for the case study that the estimation of saturation degree and porosity is better with the data fusion method, while the estimation of Rc is better with ANN.

Finally a case study was presented on reinforced concrete walls at CEA-Saclay. **OSSM for NDTs spatial optimization, but also for the spatial optimization of the cores to extract for evaluating optimally two indicators, saturation degree and compressive strength were used.** The values of both indicators for each auscultation point were obtained by the data fusion method and their spatial correlations were evaluated. However, no variogram model could be fitted for the porosity, even though a variogram model could be fitted for the NDTs used to estimate both indicators. This means that the porosity variability is constant throughout the studied structure element. Nevertheless, **the OSSM was used for the saturation degree to optimize the cores location for both indicators.** NDT and DT optimizations showed an

important decrease of the fitness functions. However for the DT case this is not as significant as the NDT case may be because the NDT variability (difference between minimum and maximum values) is more important than the DT variability. The reduced number of cores can also explain this difference.

Later, the estimation of Pc for each auscultated point was made by the use of the MPL-Pc model. The AME and RME were 10 mm and 49 % respectively. Moreover, MPL models for w, P and Rc were also tested and their results were compared to DTs made on surface and on core for the cases of w and P. In general, it was observed a decrease of the MPL models performance with the exception of MPL-P. Therefore, these results are good indicators not only for the need of a calibration to obtain better results adapted to the structure, but also, that **the performance of the MPL models is affected by the presence of carbonation. For this reason, a new model for w (MPL-wc) trained with SENSO-Pc and EVADEOS databases was developed. Its performance for the assessment of w-surface of the studied structure was increased significantly compared to the MPL-w model.**

For future works:

As the fitness functions used for the optimization spatial sampling method (OSSM) have complementary information, a good compromise can be obtained from the combination of the two fitness functions using for example a multi-objective optimization for a better evaluation of mean and variance. A cost function could also been implemented.

Until know the OSSM developed has been used with a single value for each auscultation point. For future works it is intended to study the performance of the OSSM by using also the variance of each auscultation point as an additional input. Moreover, the inclusion of the indicator errors obtained by the propagation of DTs uncertainties on the OSSM can also be a good way of evaluating its performance, either as input data or as another fitness function.

Until know, the measurement values obtained for each auscultation point, have been considered for an average auscultation depth. It would be interesting that for future works, the method could be used for a concrete cover to the reinforcement depth.

It is also intended to continue to work on the artificial neural networks. First, it will be important to develop a calibration process for the MPL implemented models and a careful consideration must be made to whether taking into account the effect of carbonation in the calibration process for the original w, P and Rc MPL models or to develop different models including carbonated concretes to assess the different indicators effectively. Second, until now the only way of evaluating the performance of the MPL implemented models is by comparing the results obtained from the models and the targeted values obtained by destructive test. It

would be interesting, for future works, to develop a method to evaluate the quality of the results, when destructive test values are not available.

REFERENCES

Adalarasan, R., Santhanakumar, M., Rajmohan, M., “Optimization of laser cutting parameters for Al6061/SiCp/Al2O3 composite using grey based response surface methodology (GRSM)”, Measurement, Vol. 73, 2015, p. 596-606.

Aït-Mokhtar A., Belarbi R., Benboudjema F., Burlion N., Capra B., Poyet S. et al. “Experimental investigation of the variability of concrete durability properties”, Cement and Concrete Research, Vol. 45, 2013, p. 21–36.

Aldahdooh, M.A., Bunnori, N.M., Johari, M.A., “Evaluation of ultra-high-performance-fiber reinforced concrete binder content using the response surface method”, Materials & Design, Vol. 52, 2013, p. 957-965.

Angst, U.M., Polder, R., “Spatial variability of chloride in concrete within homogeneously exposed areas”, Cement and Concrete Research, Vol. 56, 2014, p. 40–51.

Atici, U., “Prediction of the strength of mineral admixture concrete using multivariable regression analysis and an artificial neural network”, Expert Systems with Applications, Vol. 38, 2011, p. 9609-9618.

Bal, L., Buyle-Bodin, F., “Artificial neural network for predicting drying shrinkage of concrete”, Construction and Building Materials, Vol. 38, 2013, p. 248-254.

Balayssac, J.P., et al, ANR-GUI-AAP-04-Scientific Document, 2011.

Balayssac J.P., Laurens S, Arliguie G, Breysse D, Garnier V, Dérobert X, Piwakowski B. Description of the general outlines of the French project SENSO – Quality assessment and limits of different NDT methods. Construction and Building Materials, Vol. 35, 2012, p. 131-138.

Barnes, R., Variogram Tutorial, Global Software, Inc., p. 1-23.

Bastidas-Arteaga, E., Schoefs, F., Stochastic improvement of inspection and maintenance of corroding reinforced concrete structures placed in unsaturated environments, Engineering Structures, vol. 41, 2012, p. 50-62.

Bayramov, F., Taşdemir, C., Taşdemir, M.A., “Optimisation of steel fibre reinforced concretes by means of statistical response surface method”, Cement and Concrete Composites, Vol. 26, 2004, p. 665-675.

Belagraa, L., Abdelaziz, M., Miloud, B., “Study of the Physico-Mechanical Properties of a Recycled Concrete Incorporating Admixtures by the Means of NDT Methods”, Procedia Engineering, Vol. 108, 2015, p. 80-92.

Bektas, F., Bektas, B.A., “Analyzing mix parameters in ASR concrete using response surface methodology”, Construction and Building Materials, Vol. 66, 2014, p. 299-305.

Bloch, I., Maitre, H., “Fusion de données en traitement d’images: modèles d’information et decisions”, Traitement du Signal, Vol. 11, 1994.

Bloch, I., “Information combination operators for data fusion: A comparative review with classification”, IEEE, Vol. 26, 1996, p. 52-67.

Bohling, G., Kriging, C&PE 940, 2005, p. 1-20.

Borosnyoi A., Szilagyi K. Studies on the spatial variability of rebound hammer test results recorded at in-situ testing. Építőanyag - Journal of Silicate Based and Composite Materials, vol. 65, 2013, pp. 102-106.

Box, G.E., Wilson, K.B., “On the Experimental Attainment of Optimum Conditions”, Journal of the Royal Statistical Society, Vol. 1, 1951, p. 1–45.

Breysse, D. “Non-Destructive Assessment of Concrete Structures: Reliability and Limits of Single and Combined Techniques”. Springer, RILEM, 2012, 374p.

Breysse, D., “Nondestructive evaluation of concrete strength: An historical review and a new perspective by combining NDT methods”, Construction and Building Materials, Vol. 33, 2012, p. 139-163.

Breysse, D., Lataste, J.F., Balayssac, J.P., Garnier, V. “Quality and accuracy of concrete assessment provided by NDT measurement”, 6th International Probabilistic Workshop, Darmstadt, Germany, 2008, 15 p.

Bungey, J.H., “Determining concrete strength by using small cores”, Concrete Research, Vol. 31, 1979, p. 91-98.

Bungey, J.H., Millard, S.G., “Testing of concrete structures”, Chapman & Hall, Glasgow, 1996.

Buratti, N., Ferracuti, B., Savoia, M., “Response Surface with random factors for seismic fragility of reinforced concrete frames”, Structural Safety, Vol. 32, 2010, p. 42-51.

Cai, L., Wang, H., Fu, Y., “Freeze–thaw resistance of alkali–slag concrete based on response surface methodology”, Construction and Building Materials, Vol. 49, 2013, pp. 70-76.

Castañedo, F., “A review of data fusion techniques”, The Scientific World Journal, 2013, 19 p.

CEBTP Service Matériaux, “Essais d’intercomparaison 12ème campagne”, COFRAC, 2005.

Chang, C.F., Chen, J.W, “Strength and elastic modulus of carbonated concrete”, ACI Materials Journal, Vol. 102, pp. 315-321, 2005.

Chang, C.F., Chen, J.W., “The experimental investigation of concrete carbonation depth”, Cement and Concrete Research, Vol. 36, pp. 1760-1767, 2006

Cho, T., “Prediction of cyclic freeze–thaw damage in concrete structures based on response surface method”, Construction and Building Materials, Vol. 21, 2007, p. 2031-2040.

Cihan, M.T., Güner, A., Yüzer, N., “Response surfaces for compressive strength of concrete”, Construction and Building Materials, Vol. 40, 2013, p. 763-774.

Clark, I., Practical Geostatistics, Geostokos Limited, 2001, p. 24-29.

Colombo, M., Felicetti, R., “New NDT techniques for the assessment of fire-damaged concrete structures”, Fire Safety Journal, Vol. 42, 2007, p. 461-472.

Cui, H., Tang, W., Zhijun, W.L., Dong, F., Xing, “Experimental study on effects of CO2 concentrations on concrete carbonation and diffusion mechanisms”, Construction and Building Materials, Vol. 93, pp. 522-527, 2015.

Davis, A.G., “Nondestructive Test Methods for Evaluation of Concrete in Structures”, ACI 228.2R-98, 1998, 62 p.

De Larrard, T., Benboudjema, F., Colliat, J.B., Torrenti, J.M., “Caractérisation expérimentale de la variabilité spatiale des propriétés d’un béton: Identification des longueurs de corrélation et recherche de corrélations entre indicateurs de durabilité”. JFMS2012, Chambéry - France, 2012, 15p.

Dias, W.P., Pooliyadda, S.P., “Neural networks for predicting properties of concretes with admixtures”, Construction and building materials, Vol. 15, 2001, p. 371-379.

Doetsch, J., Linde, N., Pessognelli, M., Green, A.G., Günther, T., Constraining 3-D electrical resistance tomography with GPR reflection data for improved aquifer characterization, Applied Geophysics, vol. 78, 2012, p. 68-76.

Dreyfus G., Samuelides M., Martinez J.M., Gordon M.B., Badran F., Thiria S., Hérault L., “Réseaux de neurones: Méthodologie et applications”, Eyrolles, 2nd ed., 2004, 386p.

Dupuis O., “Fusion entre les données ultrasonores et les images de radioscopie à haute résolution: application au contrôle de cordon de soudure”, Doctoral thesis, Lyon INSA, 2000.

Dubois, D., Prade, H., “Théorie des possibilités: application à la représentation des connaissances en informatique”, Doctoral thesis, Masson, Paris, 1988.

Ferreira, R.M., Jalali, S., “NDT measurements for the prediction of 28-day compressive strength”, NDT & E International, Vol. 43, 2010, p. 55-61.

Ferreyra, R.A., Apeztegui, H.P., Sereno, R., Jones, J.W., Reduction of soil water spatial sampling density using scaled semivariograms and simulated annealing, Geoderma, vol. 110, 2002, pp. 265-289.

Garnier, V., Martini, D., Balayssac, J.P., Sbartai, Z.M., Villain, G., Piwakowski, B., Salin, J., Fardeau. V., “Analysis and Capitalisation for the Diagnosis of Constructions : Méthodologie de transfert d’essais non destructifs du laboratoire vers le site”, 12th Congrès Français de Mécanique, Bordeaux, 2013.

Garnier, V. et al., Rapport Final Projet C2D2-ACDC, March 2014.

Georgel, B., Lavayssière, B., “Fusion de données: un nouveau concept en CND”, In Procedings of the 6th European Conference on NDT, Vol. 1, 1994, p. 31–5.

Gomez-Cardenas, C., Sbartaï, Z.M., Balayssac, J.P., Garnier, V., Breysse, D., “New optimization algorithm for optimal spatial sampling during non-destructive testing of concrete structures”, Engineering Structures, vol. 88, 2015, pp. 92-99, http://dx.doi.org/10.1016/j.engstruct.2015.01.014.

Gros, X.E., Bousigue, J., Takahashi, K., “NDT data fusion at pixel level”, NDT&E International, Vol. 32, 1999, p. 283–292.

Gros, X.E., Strachan, P., Lowden, D.W., Edwards, I., “NDT data fusion”, In Procedings of the 6th European conference on NDT, Vol. 1, 1994, p. 355–359.

Güneyisi, E., Gesoğlu, M., Algın, Z., Mermerdaş, K., “Optimization of concrete mixture with hybrid blends of metakaolin and fly ash using response surface method”, Composites Part B: Engineering, Vol. 60, 2014, p. 707-715.

Haach, V.G., Juliani, L.M., Da Roz, M.R., “Ultrasonic evaluation of mechanical properties of concretes produced with high early strength cement”, Construction and Building Materials, Vol. 96, 2015, p. 1-10.

International Atomic Energy Agency (IAEA), “Guidebook on non-destructive testing of concrete structures”, Vienna, Austria, 2002, 242 p.

Jerga, J., “Physico-mechanical properties of carbonated concrete”, Construction and Building Materials, Vol. 18, pp. 645-652, 2004.

Khuri, A.I., Mukhopadhyay, S., “Response surface methodology”, John Wiley & Sons, Vol. 2, 2010, 22 p.

Kohl, C., Streicher, D., “Results of reconstructed and fused NDT-data measured in the laboratory and on-site at bridges”, Cement & Concrete Composites, Vol. 28, 2006, p. 402–413.

Koller J., Ulmke M., “Data Fusion for Ground Moving Target Tracking”, IEEE International Conference on Multisensor Fusion and Integration for Intelligent Systems, 2006, p. 217–224.

Krzemień, K., Hager, I., “Post-fire assessment of mechanical properties of concrete with the use of the impact-echo method”, Construction and Building Materials, Vol. 96, 2015, p. 155-163.

Lataste, J.F., Breysse, D., “A Study on the variability of electrical resistivity of concrete”, Nondestructive Testing of Materials and Structures, RILEM Bookseries, 2013, p. 255-262.

Li, O., Cai, L., Fu, Y., Wang, Zou, H.Y., “Fracture properties and response surface methodology model of alkali-slag concrete under freeze–thaw cycles”, Construction and Building Materials, Vol. 93, 2015, p. 620-626.

Lydon F.D., Mahawish, A.H., “Strength and permeability results from a range of concretes”, Cement and Concrete Research, Vol. 19, 1989, p. 366-376.

Malhotra, V.M., Carino, N.J., “Handbook on Nondestructive Testing in Concrete”, CRC Press, Boca Raton, FL, 2004, 384 p.

Martin, A., “La fusion d’informations, Polycopié de cours ENSIETA”, 2005.

Martini, D., Garnier, V., Ploix, M.A., “Evaluation of an intrinsic error estimator for the data fusion of NDT techniques used to identify the material and damage properties of concrete structures”, 6th workshop on structural health monitoring, Dresden, 2012.

Masi, A., Chiauzzi, L., “An experimental study on the within-member variability of in situ concrete strength in RC building structures”, Construction and Building Materials, Vol.47, 2013, p. 951-961.

Melles, S.J., Heuvelink, G.B.M., Twenhöfel C.J.W., Van Dijk, A., Hiemstra, P.H., Baume, O., Stöhlker, U., Optimizing the spatial pattern of networks for monitoring radioactive releases, Computers & Geosciences, vol. 37, 2011, pp. 280-288.

Mohammed, B.S., Fang, O.C., Hossain, K.M., Lachemi, M., “Mix proportioning of concrete containing paper mill residuals using response surface methodology”, Construction and Building Materials, Vol. 35, 2012, p. 63-68.

Molyneaux, T.C., Millard, S.G., Bungey, J.H., Zhou, J.Q., “Radar assessment of structural concrete using neural networks”, NDT & E International, Vol. 28, 1995, p. 281-288.

Nam, Y.S., Jeong, Y.I, Shin, B.C., Byun, J.H., “Enhancing surface layer properties of an aircraft aluminum alloy by shot peening using response surface methodology”, Materials & Design, Vol. 83, 2015, p. 566-576.

Nambiar, E.K., Ramamurthy, K., “Models relating mixture composition to the density and strength of foam concrete using response surface methodology”, Cement and Concrete Composites, Vol. 28, 2006, p. 752-760.

Neville, A.M., “Propriétés des bétons”, Eyrolles, CRIB Sherbrooke-Laval, 1995, 806p.

Newman, J., Seng Choo, B., “Testing an quality”, Advanced Concrete Technology, 2003, 313p.

Nguyen, N.T., “Évaluation non destructive des structures en béton armé: Étude de la variabilité spatiale et de la combinaison des techniques”, Doctoral Thesis, Bordeaux University, 2014.

Nguyen, N.C., Sbartaï, Z.M., Lataste, J.F., Breysse, D., Bos, F., Assessing the spatial variability of concrete structures using NDT techniques – Laboratory tests and case study, Construction and Building Materials, vol. 49, 2013, pp. 240-250.

Nikbin, I.M., Eslami, S.H., Rezvani, D. “An experimental comparative survey on the interpretation of concrete core strength results”, European journal of scientific research, Vol. 37, 2009, p. 445-456.

O’Connor, A.J., Kenshel, O., “Experimental evaluation of the scale of fluctuation for spatial variability modeling of the chloride-induced reinforced concrete corrosion”, Journal of Bridge Engineering, Vol. 18, 2013, p. 3-14.

Ollivier, J.P., “Les résultats des essais croises Afrem pour la Détermination de la masse volumique apparente et de la porosité accessible à l’eau des bétons”, AFREM, 1998, 6p.

Pardo-Igdzquiza, E., Chica-Olmo, M., The Fourier Integral Method: An efficient spectral method for simulation of random fields, Mathematical Geology, vol. 25, n° 2, 1993, pp. 177-217.

Pei, H., Li, Z., Zhang, J., Wang, O., “Performance investigations of reinforced magnesium phosphate concrete beams under accelerated corrosion conditions by multi techniques”, Construction and Building Materials, Vol. 93, 2015, p. 989-994.

Pfister, V., Tundo, A., Luprano, V.A.M., “Evaluation of concrete strength by means of ultrasonic waves: A method for the selection of coring position”, Construction and Building Materials, Vol. 61, 2014, p. 278-284.

Ploix, M.A., Garnier, V., Breysse, D., Moysan, J., “NDE data fusion to improve the evaluation of concrete structures”, NDT&E International, Vol. 44, 2011, p. 442–448.

Pollard, E., “Évaluation de situations dynamiques multicibles par fusion de données spatio-temporelles”. Doctoral Thesis, Grenoble University, 2010, 268 p.

Project MAT1-CT94-0043, “Inter-laboratory comparison to support revision CEN/ISO standards called up in EN 206”, Concerte, 1997.

Pucinotti, R., “Assessment of in situ characteristic concrete strength”, Construction and Building Materials, Vol.44, 2013, p. 63-73.

R.A.M, “A comparison between cube strength and in situ concrete strength developement”. In Proceedings of the Institution of Civil Engineering Structures and Buildings, 1996, p. 138-153.

Ratkoe, B.L., Hedayat, A., Federer, W.T., “Factorial Designs”, John Wiley & Sons, 1981.

Rougeau, P., “Les résultats d'essais Croises Afrem: Essai de carbonatation acceleré”, AFREM, 1998, 18p.

Sbartaï, Z.M., “Caractérisation physique des bétons par radar approche neuromimetique de l’inversion”, Doctoral thesis, Toulouse and Sherbrooke universities, 2005.

Sbartaï, Z.M., Breysse, D., Larget, M., Balayssac, J.P., “Combining NDT techniques for improved evaluation of concrete properties”, Cement and Concrete Composites, Vol. 34, 2012, p. 725-733.

Sbartaï, Z.M., Laurens, S., Elachachi, S.M., Payan, C., “Concrete properties evaluation by statistical fusion of NDT techniques”, Construction and Building Materials, Vol. 37, 2012, p. 943-950.

Schoefs F, Tran TV, Bastidas-Arteaga E, Villain G, Derobert X, O'Connor AJ, Bonnet S. Optimization of non-destructive testing when assessing stationary stochastic processes: application to water and chloride content in concrete. Proceedings of the International Conference Durable Structures (ICDS12), Lisbon – Portugal, 31 May – 1 June 2012, p. 14.

Shamekhi, E., Tannant, D.D., "Probabilistic assessment of rock slope stability using response surfaces determined from finite element models of geometric realizations", Computers and Geotechnics, Vol. 69, 2015, p. 70-81.

Shaw, M.R., Millard, S.G., Molyneaux, T.C., Taylor, M.J., Bungey, J.H., "Location of steel reinforcement in concrete using ground penetrating radar and neural networks", NDT & E International, Vol. 38, 2005, p. 203-212.

Şimşek, B., İç, Y.T., Şimşek, E.H., Güvenç, A.B., "Development of a graphical user interface for determining the optimal mixture parameters of normal weight concretes: A response surface methodology based quadratic programming approach", Chemometrics and Intelligent Laboratory Systems, Vol. 136, 2014, p. 1-9.

Stein, A., Ettema, C., An overview of spatial sampling procedures and experimental design of spatial studies for ecosystem comparisons, Agriculture, Ecosystems and Environment, vol. 94, 2003, pp. 31-47.

Stewart MG, Suo Q. Extent of spatially variable corrosion damage as an indicator of strength and time-dependent reliability of RC beams. Engineering Structures, Vol 31, 2009, pp. 198–207.

Tacnet, J.M., Richard, D., Dezert, J., Batton-Hubert, M., "Aide à la décision et fusion d'information pour l'expertise des risques naturels: Analyse de l'efficacité des ouvrages de protection", JFMS, Toulouse, 2010.

Trocoli, A., Dantas, A., Batista, M. De Jesus Nagahama, L.K., "Prediction of compressive strength of concrete containing construction and demolition waste using artificial neural networks", Construction and Building Materials, Vol. 38, 2013, p. 717-722.

Turatsinze, A., Castel, A., Bascoul, M., Mouret, M., "Comparaison entre la résistance des éprouvettes normalisées en béton et la résistance du béton in situ", Annales du Bâtiment et des Travaux Publics, 1999, p. 43-51.

Valet L., Mauris G., Bolon P., "A Statistical Overview of Recent Literature in Information Fusion", In proceedings of the 3rd International Conference On Information Fusion, Paris, 2000, p. MoC3-22.

Van Groeningen, J.W., Siderius, W., Stein, A., Constrained optimization of soil sampling for minimization of the kriging variance, Geoderma, vol. 87, 1998, pp. 239-259.

Villain, G., Sbartaï, Z.M., Dérobert, X., Garnier, V., Balayssac, J.P., "Durability diagnosis of a concrete structure in a tidal zone by combining NDT methods: Laboratory tests and case study", Construction and Building Materials, Vol. 37, 2012, p. 893-903.

Viriyametanont, K., "Reconnaissance physique et géométrique d'éléments en béton armé par radar et réseaux de neurones artificiels", Doctoral thesis, Toulouse university, 2008.

Völker, C., Shokouhi, P., "Multi sensor data fusion approach for automatic honey comb detection in concrete", NDT&E International, Vol. 71, 2015, p. 54–60.

Xiang, Y., Tso, S.K., "Detection and classification of flaws in concrete structure using bispectra and neural networks", NDT & E International, Vol. 35, 2002, p. 19-27.

Yeh, I.C., “Modeling of strength of high-performance concrete under normal outdoor exposure”, RILEM Seminar on durability, Hanover, 1984.

Zaid, M., Gaydecki, P., Quek, S., Miller, G., Fernandes, B., “Extracting dimensional information from steel reinforcing bars in concrete using neural networks trained on data from an inductive sensor”, NDT & E International, Vol. 37, 2004, p. 551-558.

Zhang, J., Chen, H.Z., Huang, H.W., Luo, Z., “Efficient response surface method for practical geotechnical reliability analysis”, Computers and Geotechnics, Vol. 69, 2015, p. 496-505.